Towards ultrasensitive SPR-based sensing: self-referencing and detection of single nanoparticles

Von der Fakultät für Umwelt und Naturwissenschaften
der Brandenburgischen Technischen Universität Cottbus-Senftenberg
zur Erlangung des akademischen Grades eines
doctor rerum naturalium (Dr. rer. nat.)

genehmigte Dissertation

vorgelegt von

Master of Science (M.Sc.)

Vitali Scherbahn

aus Floreschty, Moldawien

Gutachter: Prof. Dr. Vladimir M. Mirsky

Gutachter: Prof. Dr. Peer Schmidt

Gutachter: Prof. Dr. Gunther Wittstock

Tag der mündlichen Prüfung: 18.12.2018

Erklärung

Ich, Vitali Scherbahn, versichere meine Dissertation

"Towards ultrasensitive SPR-based sensing: self-referencing and detection of single nanoparticles"

selbständig ohne unerlaubte Hilfe angefertigt und mich dabei keiner anderen als der von mir ausdrücklich bezeichneten Quellen bedient zu haben.

Die vorliegende Dissertation wurde in der jeweiligen oder einer ähnlichen Form noch bei keiner anderen Hochschule eingereicht und hat noch keinen sonstigen Prüfungszwecken gedient.

Vitali Scherbahn

Berlin, 11.06.2018

Abstract

Surface plasmon resonance (SPR) and its extensions, surface plasmon resonance imaging (SPRi) and surface plasmon resonance microscopy (SPRM) both enabling visualization of the sensor surface, belong to classical, indispensable highly sensitive and robust optical (bio)analytical techniques to study affinity processes on a surface. Nevertheless, SPR and SPRi/SPRM undergo a continuous development in regard to the improvement of sensitivity. The main challenge in this direction is attributed to the separation of signals due to the binding of analytes and those due to the bulk effect.

The main task of the present thesis was to apply different strategies to improve the performance of SPR sensing. Within this scope, two main objectives were pursued: (1) implementation and realization of a so-called internal referencing towards suppression of the bulk effect leading to an improvement and optimization of the signal-to-noise ratio (SNR) and (2) application of wide-field (WF)-SPRM to detect, to visualize and to characterize single nanoparticles adsorbed to modified surfaces.

The first objective of this thesis comprises the realization of three different internal-referencing approaches. In the first approach, a self-referencing effect based on arbitrarily distributed micro-patterned self-assembled monolayer (SAM) containing sensing and referencing spots was realized. Measurements of classical antigen-antibody-interaction resulted in a 10-fold improvement of the SNR by suppression of the bulk effect and the corresponding microfluctuations of the bulk temperature. The application of the second internal-referencing-approach, ionic referencing, acting as an assessment of patterned SAM was realized using electrolytes with a high molar refraction of either anions or cations to micro-patterned SAM combined with WF-SPRM as detecting technology. As a result, successful, unobtrusive visualization and spatial distinction of micro-patterned surfaces was shown. Unlike visualization of micro-scaled surface areas, the application of spatio-temporal referencing in WF-SPRM, as a third type of internal referencing, enables to detect, moreover to visualize and localize, smallest changes in refractive index near/on the sensor surface.

In that sense, the second objective of this thesis was dedicated to the application of the WF-SPRM technology combined with spatio-temporal referencing to detect, to visualize, to quantify and to characterize single nanoparticles adsorbed to the sensor surface; here, nanoparticles act as analyte species. As a result, adsorption of single nanoparticles of different materials and sizes both to homogeneously and heterogeneously coated surfaces was successfully investigated. Based on a sophisticated image

analysis, successful detection and characterization of single nanoparticles in complex media such as wine, juice and sun cream was performed showing an apparent limit of detection about 10^6 nanoparticles ml^{-1}, which can be significantly decreased by increasing the measurement time or by increasing the measurable sensor area.

Besides being a powerful solution for nanoparticles analytics, the WF-SPRM technology represents a base to develop novel, ultra-sensitive and fast (bio)sensing platforms. Within this scope, enzyme-assisted generation of nanoparticles was studied. Among several enzymes investigated, alkaline phosphatase (ALP) was shown to be the most appropriate one to mediate formation of gold nanoparticles within first minute(s). Applying WF-SPRM as main detecting technology, successful detection, visualization and quantification of single gold nanoparticles generated by ALP both unbound in solution and immobilized as an enzyme-antibody-conjugate to the sensor surface was performed.

Zusammenfassung

Oberflächenplasmonenresonanz (engl. surface plasmon resonance, SPR) und deren Erweiterungen Oberflächenplasmonenresonanz-Imaging (SPRi) und Oberflächenplasmonenresonanz-Mikroskopie (SPRM) gehören zu den klassischen, unverzichtbaren, robusten und äußerst empfindlichen Messtechnologien, um Affinitätsprozesse auf modifizierten Oberflächen zu untersuchen. Nichtsdestotrotz unterliegt diese Messtechnologie einem kontinuierlichen Entwicklungsprozess hinsichtlich der Messempfindlichkeit. Dabei stellt die Trennung des Affinitäts- vom Volumensignal die größte Herausforderung dar.

Das Ziel der vorliegenden Dissertation besteht in der Anwendung von unterschiedlichen Strategien zur Optimierung der Leistung und der Empfindlichkeit von SPR-basierten (Bio)sensoren. Um das Ziel zu erreichen, wurden zwei Ansätze verfolgt: (1) Implementierung und Realisierung einer sogenannten internen Referenzierung zur Unterdrückung des Volumeneffekts mit dem Ziel, das Signal-Rausch-Verhältnis zu optimieren und (2) die Anwendung von Weitfeldoberflächenplasmonenresonanzmikroskopie (engl. wide-field (WF)-SPRM) zur Detektion, Visualisierung und Charakterisierung der Adsorption einzelner Nanopartikel auf modifizierten Oberflächen.

Im ersten Teil der vorliegenden Arbeit wurden drei Ansätze zur Realisierung einer internen Referenzierung verfolgt. Der erste Ansatz basiert auf der Anwendung einer durch Referenz- und aktive Oberflächenbereiche mikrostrukturierten Beschichtung der Sensoroberfläche. Messungen von Antigen-Antikörper-Wechselwirkungen ergaben dabei eine 10-fache Verbesserung des Signal-Rausch-Verhältnisses. Der zweite Ansatz – ionische Referenzierung, um mikrostrukturierte Oberflächen mithilfe von WF-SPRM zu untersuchen bzw. abzubilden – basiert auf der Anwendung von Salzen, welche eine hohe Differenz in ihrer Molrefraktion aufweisen. Somit konnten schwierig zu untersuchende monomolekulare Oberflächenstrukturen, die z.B. unterschiedliche Oberflächenladungen aufweisen, sichtbar gemacht werden. Der dritte Ansatz basiert auf der Kombination einer räumlich-zeitlichen (engl. spatio-temporal) Bildreferenzierung mit bildgebender WF-SPRM-Technologie, um äußerst minimale Änderungen im Brechungsindex nahe der Sensoroberfläche visuell zu erfassen.

Gleichzeitig stellt dieser Ansatz den zweiten Teil der vorliegenden Arbeit dar: Nachweis, Sichtbarmachung und Analyse der Wechselwirkung zwischen einzelnen

Nanopartikeln und modifizierten Sensoroberflächen mittels höchstempfindlicher WF-SPRM. Mit dieser Technologie konnten industriell hergestellte Nanopartikel unterschiedlicher Größen, unterschiedlichen Materials auf unterschiedlich modifizierten und strukturierten Sensoroberflächen untersucht werden. Des Weiteren war es möglich, Nanopartikel sowohl in einfachen, wässrigen Medien als auch in komplexen Flüssigkeiten (Saft, Wein, Sonnencreme) zu untersuchen, sichtbar zu machen und zu quantifizieren. Der Nachweis einzelner Nanopartikel mittels WF-SPRM eröffnet neue Perspektiven hinsichtlich der Entwicklung innovativer Sensorplattformen. In diesem Sinne wurde die WF-SPRM-Technologie zur Untersuchung von enzym-vermittelter Synthese von Nanopartikeln sowohl mit ungebundenem als auch mit an die Sensoroberfläche gekoppeltem Enzym erfolgreich eingesetzt.

Contents

1. Introduction

The introduction and the state of the art originate with minor adaptations from the published book chapter (sections 1–4):

Toward Ultrasensitive Surface Plasmon Resonance Sensors

SCHERBAHN, V., NIZAMOV, S., & MIRSKY, V. M.

Published in: *Label-Free Biosensing: Solid State Micro- and Nano Biosensors, Advanced Materials, Devices and Applications*. A. Poghossian & M. J. Schoening (Eds.), 2017, Springer.
DOI: 10.1007/5346_2017_21

Affinity sensors form one of the main classes of chemical sensors. An exact definition of this type of sensors could be found neither in IUPAC nor in other chemical literature. However, based on general logic of this commonly used term, it can be defined as a type of chemical sensor whose output signal is proportional to the concentration of analyte bound to the receptor layer. The story of affinity sensors is almost a century long and it was probably started with the first attempts to use optical techniques (for example, interferometry [1] or electrochemical methods [2]) to study adsorption processes. The next important step in establishing the concept of affinity sensing was an implementation of quartz microbalance [3, 4] – in combination with intensive development of semiconductor electronics. A whole measurement system was realized as a compact device. Namely, based on the quartz microbalance (in some cases, the words quartz crystal microbalance are also used), the main application fields of affinity sensors, such as affinity biosensors (immunosensors) or gas sensors were formulated. The next important step in the development of affinity sensors was the implementation of surface plasmon resonance (SPR). At the beginning of 1980's, the Swedish group [5] suggested to apply this physical phenomenon for chemical sensing. After this pioneer work, the first commercial SPR-sensor was developed by the Swedish company Pharmacia at the end of the 1980's; later, this part of the company was separated into BiaCore and then purchased by GE Healthcare [6, 7]. Further development occurred extremely fast. Before the pioneer work, the resonance of surface plasmons was known as a sophisticated physical effect only. Just 10–15 years later, the abbreviation "SPR" became well known not only to physicists but also to chemists and biologists while the method of SPR was established as a powerful instrument for real-time label-free investigation of interactions of (bio)molecules in biochemistry, pharmacology, supramolecular chemistry and in other fields of science and technology. Currently, over 20 different companies offer such devices.

1.1 State of the art

1.1.1 Surface plasmon resonance: Basic measurement configuration

The underlying physical principles of SPR are described in [8, 16, 17]. In the Kretschmann configuration, which is most frequently used in SPR instruments, the SPR effect is simply observed as a frustration of the total internal reflection of *p*-polarized light from a thin metallic layer deposited on the surface of a glass prism. This effect occurs due to the coupling of impinging light to the collective oscillations of electrons (surface plasmons) on the surface of the highly conducting metallic layer (for example, silver or gold). Oscillations of surface plasmons generate an electromagnetic wave that penetrates to both sides of this surface. The intensity of this electromagnetic wave decays exponentially, thus, it is called an evanescent wave. At resonance conditions, the incident light is almost completely coupled to the surface plasmons thus achieving

a manifold increase in the intensity of the evanescent wave. Small changes in the refractive index within the penetration depth of the evanescent wave change resonance conditions. This provides a way to make extremely sensitive measurements of adsorption of any species onto the resonant surface: just a few angstrom change in the mean thickness of the adsorbed layer leads to a measurable signal. In such instruments the p-polarized light beam is reflected from the thin metallic layer deposited on the surface of the glass prism (Fig. 1.1a). The reflectivity (ratio of reflected and incident light intensities) in this case depends on the coupling condition of incident light to surface plasmons:

$$k = \frac{2\pi}{\lambda}\sqrt{\frac{\epsilon_1\epsilon_2}{\epsilon_1+\epsilon_2}} = \frac{2\pi}{\lambda}\sqrt{\epsilon_0}\sin\theta \tag{1.1}$$

where k_x is the wavenumber, λ is the free-space wavelength of incident light, θ is its incidence angle, ϵ_0, ϵ_1 and ϵ_2 are complex dielectric permittivities of the glass, metal film and aqueous solution, correspondingly. The plot of the reflectivity of SPR biosensor versus incidence angle (and/or wavelength) shows a strongly pronounced dip. The exact position and shape of the reflectivity dip, caused by SPR, depends only on ϵ_2 if other parameters (ϵ_0, $\epsilon_1$and θ) remain constant. Thus, the SPR curve provides information on the dielectric permittivity (correspondingly, on refractive index n using the $\epsilon = n_2$ relation) near to the exposed metal surface (Fig. 1.1a). An example of such dependency of SPR curve is shown in Fig. 1.1. The SPR biosensor consists of a 50 nm gold layer deposited on the coupling glass prism exposed to the pure water. For a better adhesion of gold to the glass surface, a 2 nm thick chromium adhesive layer is considered. This layer was also taken into account in the calculations of the SPR effect; however, its influence on this effect is minor. In case of deposition of a thin organic layer (ϵ_p) on the gold surface, exposed to the aqueous solution (ϵ_a), the dielectric permittivity (ϵ_2) and the refractive index (n_2) of media near the gold surface are not homogeneous (Fig. 1.1a). To account for inhomogeneous distribution of refractive index near the gold surface ($\epsilon_2 = f(z)$, where z is distance from the surface) the concept of effective refractive index n_{eff} is useful [19]:

$$n_{eff} = \frac{2}{z_2}\int n_2(z)e^{\frac{-2z}{z_2}}dz \tag{1.2}$$

where $n_2(z)$ is the distribution of refractive index in aqueous media defined by refractive index of adsorbed layer (n_p) and bulk aqueous solution (n_a), z_2 is the penetration depth of the evanescent wave into the aqueous media.

In Fig. 1.1b, SPR curves were calculated for an organic layer with refractive index $n = 1.49$, which is close to that of proteins [20–22]. The deposition of a thin organic layer on the gold surface increases the effective refractive index and the whole SPR curve shifts to the right. This shift characterizes the thickness and the refractive index

of the organic layer. This is the main idea of SPR application in chemo- and biosensors: the high sensitivity of the resonance shift to minor changes of refractive index near the resonant layer (within the substantial penetration of the evanescent wave) allows one to use it as a highly sensitive refractometric transducer. Thus, the binding of analyte to the sensor surface (Fig. 1.2) as a change of the effective refractive index Δn_{eff} can be detected.

It follows from Eq. 1.1 that at constant optical properties (refractive index) of participating media, SPR effect is determined by the incidence angle of impinging light. However, most materials have a dispersion of refractive index whose value is dependent on the wavelength ($n = n(\lambda)$). Thus, the SPR effect is dependent on the

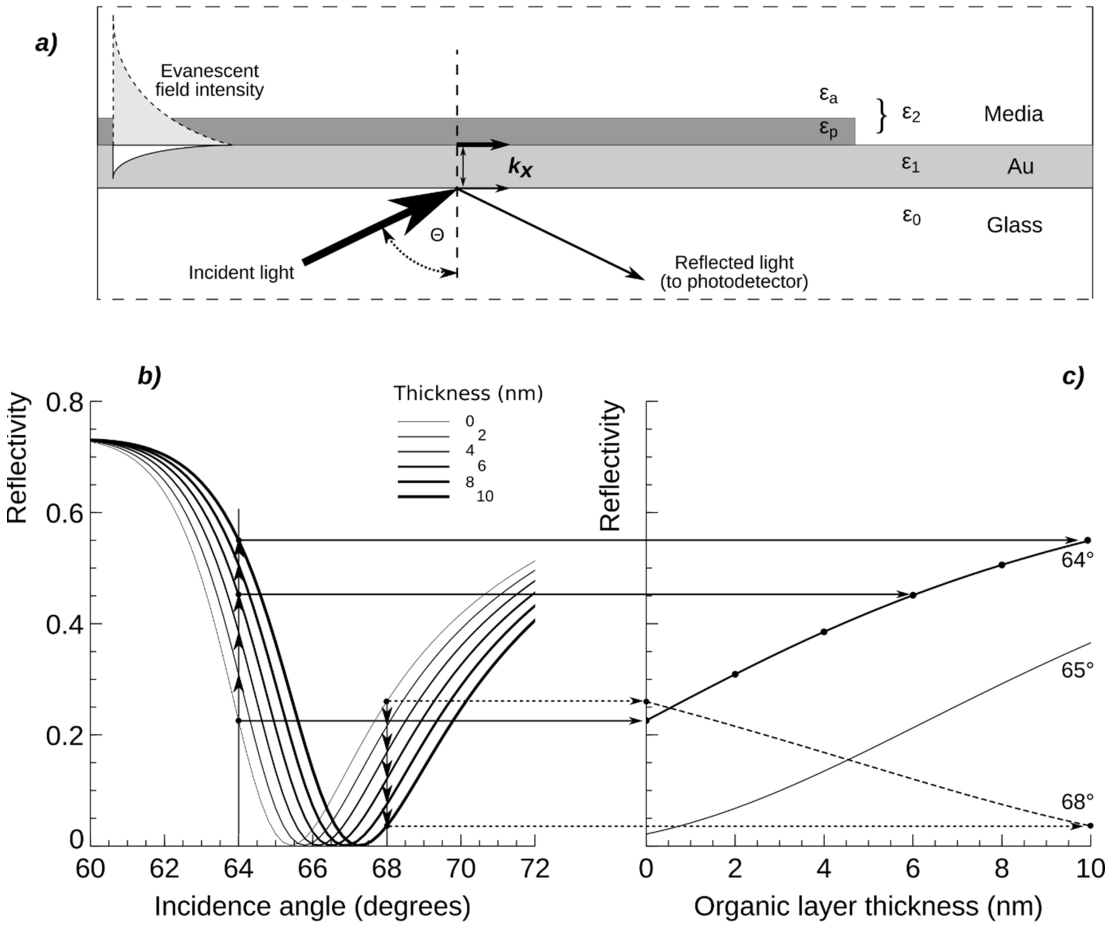

FIGURE 1.1: Kretschmann configuration for SPR measurement (a), SPR curves calculated for different thickness of organic layer on the metallic surface (b) and corresponding reflectivity changes measured at fixed incidence angle (64, 65 or 68 °) (c). Parameters for the calculation: metallic layer consists from 2 nm Cr and 50 nm Au layer (refractive indices: Cr: 3.105 + 3.327i, Au: 0.168 + 3.138i); glass (refractive index 1.615); wavelength: 650 nm; organic layer: refractive index 1.49; thickness of the organic layer: 0, 2, 4, 6, 8 or 10 nm. The organic layer is contacting with water at 22 °C (refractive index 1.3317). (Reproduced from [18])

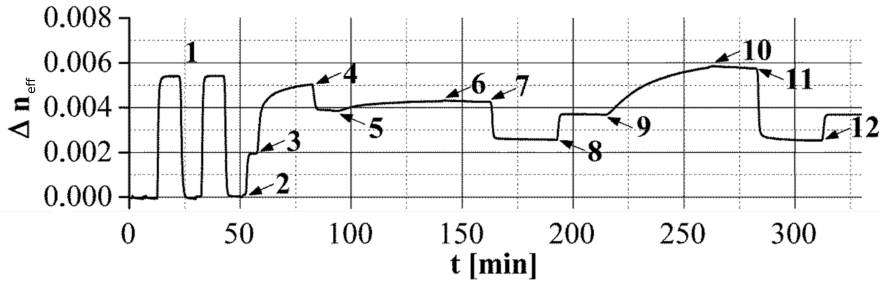

FIGURE 1.2: Typical SPR sensogram denoting the change of the effective refractive index (Δn_{eff}): (1) sensor calibration by subsequent injections of water and 600 mM NaCl in water. Next steps: (2) running buffer, (3) covalent coupling of human serum albumin (HSA), (4) running buffer, (5) monoclonal anti-HSA antibody, (6) running buffer, (7) elution buffer, (8) running buffer, (9) polyclonal anti-HSA, (10) running buffer, (11) elution buffer, (12) running buffer. (Reproduced from [23])

wavelength of the impinging light as well. Correspondingly, there are three prime approaches to realize a sensor based on SPR:

1. Fixing the wavelength of incident light and measuring the angular dependence of SPR reflectivity (the full SPR curve or just the angle of SPR dip, also known as an angular interrogation).

2. Fixing the incidence angle and measuring the wavelength dependence (SPR spectra, wavelength interrogation).

3. Fixing both the incidence angle and wavelength, measuring the intensity (or phase) of the reflected light.

The first approach is based on the fixation of the wavelength and on the measurement of the position of the SPR minimum (SPR angle) by variation of the incidence angle. This requires measurements at some angle range around the resonance angle. Namely, this approach was realized in the first commercial SPR device from Biacore and later in the SPR micromodule SPREETA developed by Texas Instruments. To exclude the necessity to use moveable parts, the angle dependence was measured for a divergent (or convergent) light beam using a linear array of photodiodes (the principle is described at www.biacore.com or in [24]). Using a rotating prism (it was realized in the device of Biosuplar) leads to lower sensitivity but allows one to extend the angle range. From the angle dependence of reflectivity, the resonance angle is determined as the angle of minimal reflectivity. The angle shift due to the adsorption characterizes the thickness of the adsorbed layer (Fig. 1.1b). In the second approach (wavelength interrogation), the dispersion of the dielectric permittivities leading to the wavelength dependence of SPR is exploited. The main contribution into this dependence is provided by the dispersion of metals, which can be described by the Drude model. By measuring the wavelength dependence of the reflected light at fixed incidence angle, the SPR effect can be measured as a dip in the reflection spectra. The position of this

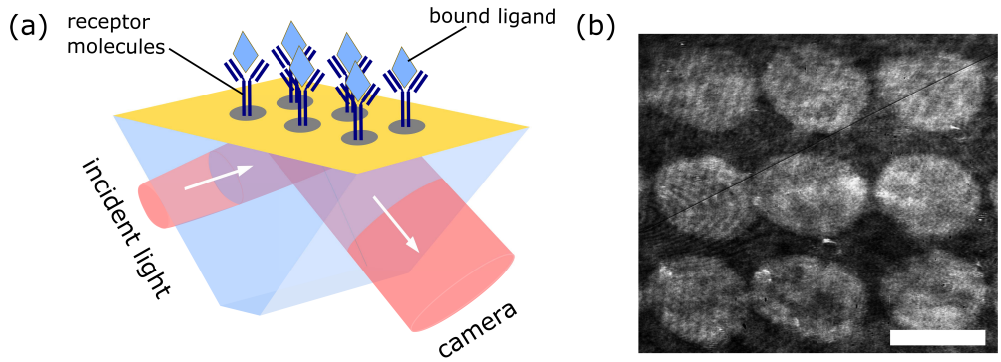

FIGURE 1.3: (a) Schematic of a sensor array in a SPR-imaging setup. (b) Integral SPR-image of a 3 x 3 sensor array prepared according to [19]. Scale bar 200 μm.

dip (its wavelength) characterizes the adsorption. Either approach is practically effective for measuring a single or few SPR signals. For the high-throughput application of SPR sensors, however, simultaneous measuring of many SPR signals is essential. An efficient way of implementing this is by imaging of SPR sensor surface. Since implementation of angular or wavelength interrogation for SPR imaging is difficult, in this case, the third approach is mainly used. In the third approach, both wavelength and angle of the incident light are fixed, and the intensity (in more advanced instruments – the phase) of the reflected light is measured. Such a case is shown in Fig. 1.1c where the light with a wavelength of 650 nm is incident at an angle of 64°, and due to an increase in the thickness of the organic layer the SPR curve shifts to the right resulting in an increase in the reflected light intensity. If the incidence angle is larger than the resonance angle (Fig. 1.1c, 68° curve), the sensor response becomes negative: an increase in the thickness of the organic layer results in decrease in the reflected light intensity. All three approaches to measure SPR are well presented in scientific literature [8, 9, 13]. The features of the approach based on the variation of angle or on simultaneous measurements at different angles were analyzed in [5, 25]. The measurements based on the variation of wavelength at fixed incident angle were discussed in [26–28]. This approach provides a high sensitivity at higher wavelengths, when the resonance is sharper, therefore it is often used in the near infra-red range [29, 30]. The approach based on the measurement of light intensity provides the simplest realization: such a device does need neither a spectrometer nor precise mechanical parts. At the same time, focusing of the image of the SPR sensor area on the image sensor (camera) enables an important extension of SPR technology – SPR imaging (SPRi) or SPR microscopy (SPRM) [31] (Fig. 1.3). The difference between these terms is only the magnification and lateral resolution. SPRi is mainly applied for characterization of homogenous films where a high magnification and/or resolution are not required [32]. The simultaneous real time imaging of the entire sensor surface in SPRM/SPRi has a lot of advantages, e.g., it provides a development of high-throughput, multiplexed

or self-referencing sensors [32–34] while their low lateral optical resolution is outweighed by extremely high sensitivity in transversal direction. Due to these features, SPRi is now widely used in surface science and in bioanalytical chemistry, particularly in chemo- and bio- sensing. The immobilization of capturing entities or ligands is usually carried out off-line by spotting of the selective ligands in a microarray format [35], as can be seen in Fig. 1.3. The binding of analytes leads to a change of the spot intensity that correlates with the amount of bound analyte. Examples of such applications are described in [36].

1.1.2 Main factors limiting the performance of SPR-based sensors

As shown by Eq. 1.1 and Eq. 1.2, SPR sensors are based on the transducing of effective refractive index (n_{eff}) of adjacent media into the optical response. Therefore, a SPR sensor can be used for measuring both physical and chemical effects that influence the refractive index within the penetration of the evanescent wave. This fact also explains the versatility and the wide application field of SPR sensors, as well as the fact that SPR sensors are inherently non-specific by the measured process. Therefore, the development of affinity chemo- and biosensors, where the sensor surface is specifically modified to detect an analyte, only partially solves the problem of the signal specificity. As the evanescent field penetrates into the background much beyond the receptor–analyte layer, the detected signal may also include changes in refractive index due to fluctuations, e.g., by temperature, composition of the background solution, inhomogeneous distribution of the analyte concentration in the background solution, or unspecific adsorption of other compounds. In addition, the measurement setup may also have mechanical drifts (influencing e.g., the actual incidence angle), temperature drifts (causing e.g., the change of refractive index of substrate and plasmonic layer on it), wavelength and/or polarization fluctuation of the light source, noise of the detector itself etc. Therefore, the resulting SPR signal contains contribution from both useful signal (e.g., due to specific adsorption of analyte) and undesired noise. Correspondingly, the applicability of SPR sensor for a particular case is determined by the value of the signal-to-noise ratio (SNR). Therefore, the improvement of SPR sensors can be roughly divided into two directions: (1) increasing of the useful signal or of SNR and (2) separation of the contributions of the surface layer (the layer of receptor and adsorbed analyte) and that of the bulk effect (effect of the background solution). The first goal is mainly achieved by optimization of the receptor layer, metallic resonant layer and instrumentation, as well as by development of new measurement configurations. The second goal is achieved by introduction of internal referencing into SPR sensing. Both aspects will be discussed in the next sections.

1.1.3 Increase of signal magnitude and singnal-to-noise ratio

1.1.3.1 Optimization of the receptor layer

First reports on application of SPR for chemical sensing and biosensing [5, 37] were performed using a silver resonant layer to investigate just physical adsorption. However, the further development of this technique was highly favoured by the discovery of an extremely strong gold-thiol bond [38]; which has resulted into intensive development of technology of self-assembled monolayers [39–42]. The interaction of thiolates with such metals, like gold or silver (as well as nickel, copper, mercury and few others), leads to the formation of a bond with an energy of ~50 kJ/mole [39, 42]. This value is essentially higher than the typical energy of a hydrogen bond, but is still few times lower than the typical energy of a covalent bond (~400 kJ/mole). The formation of self-assembled monolayers (SAM) by thiolated compounds on metallic surfaces has provided a solution for the long-term problem of biomolecule immobilization on metallic surfaces. The technology is well compatible with industrial needs. An expelling of non-thiolated compounds presented at much higher concentrations [43] decreases the requirements of surface purity. Therefore, since the middle of 1990's, the typical approach of immobilization of biomolecules on gold surface (or silver; other metals are used very seldom) has been based on the following steps: (i) deposition of a SAM of ω-functionalized (typically – carboxy-functionalized (–COOH)) alkylthiol, (ii) chemical conjugation of biomolecules to the functionalized groups of the SAM.

Numerous literature data demonstrate the possibility to use almost any type of thiolated molecules for the formation of SAM [39, 44–49]. However, from the thermodynamic point of view, a monomolecular layer (even with a high but finite binding energy to the surface) cannot be in equilibrium with a liquid containing a zero concentration of such molecules – it would lead to an infinitely high gradient of chemical potentials between the deposited layer and the volume phase. Therefore, one can expect only a strong suppression of kinetics of spontaneous desorption. This apparent stability is expected to increase with increasing of the energy of these molecules in the liquid phase. The spontaneous desorption can be simply measured using monitoring of the electrode capacitance [40] or radioactive approaches [50]. For –COOH alkylthiols the desorption rate becomes impossible to be measured by capacitive monitoring during 1000 min incubation if the length of the hydrophobic chain of these molecules reaches 15 methylene groups. Assuming an about 25 times ratio between electric capacities of coated and uncoated electrode and a ~0.5% sensitivity of the measurement, one obtains a desorption rate below 1 molecule from 10^6 molecules per second. The stability can be also improved by the cross-linkage of thiol molecules by immobilized proteins [40]. Another approach to improve the stability of the gold–thiol bond is based on the application of thiol compounds with two [51] or more [52, 53] thiol groups; in this case, the water solubility of the compound is essentially less important and even well soluble thiolates form very stable monolayers.

Chemical conjugation of receptor molecules to the functional group of formerly deposited SAM can be performed by different techniques [47, 54–56]. One of the mostly used techniques providing a well reproducible and highly effective immobilization is to form a peptide bond between the –COOH group of the SAM and the primary $–NH_2$ group of the biomolecule. This approach includes an activation of the –COOH group by water soluble 1-ethyl-3-(3-dimethylaminopropyl)carbodiimide (EDC) [57–59] followed by the reaction with the $–NH_2$ group. EDC is sometimes used in a mixture with an additional activating reagent, N-hydroxysuccinimide (NHS) [59, 60], which catalytically affects the reaction. To the immobilization approaches established during the last two decades also belongs the "click" chemistry [61, 62] and the oriented immobilization of antibodies through their preliminary oxidized sugar group [63]. However, due to a rather complicate chemistry and expensive reagents, the application of these techniques is still relatively limited. The development of technologies of SAM-based immobilization of biomolecules, which occurred in the same time as the introduction of SPR technology, was an extremely important promoting factor for the fast development and expansion of this type of affinity sensing. On the other hand, the progress in surface chemistry provided a possibility to make a precise design of the sensor surface and to realize conditions for maximal efficiency of SPR measurements. It was performed by introduction of three-dimensional receptor layers.

The typical size of protein molecules is 3–10 nm, but the penetration depth of the evanescent wave into aqueous phase is ~150 nm for 600 nm wavelength of the incident light increasing slightly superlinear till a penetration depth of ~750 nm for 1100 nm wavelength of the incident light [64]. Therefore, in measurements of monomolecular protein layers at 650 nm, their contribution into the effective refractive index is only a few percent. Correspondingly, the SPR signal is dominated by the refractive index of the media and the effect of protein layers is relatively lower. This was a motivation to immobilize receptors into three-dimensional matrix of hydrogel with a thickness of about 100 nm [6, 24, 65]. However, due to the necessity to provide a diffusion of the analyte through this hydrogel, it should be very porous. Moreover, the randomly immobilized receptor molecules are at some distance from the SPR sensor surface, thus decreasing their impact on the effective refractive index. However, already at the concentration of receptors equivalent to 1.5 monolayers, the overall SPR signal is larger than for the dense monolayer directly on the sensor surface [6]. Therefore, the implementation of this approach allows one to increase the SPR effect for several times due to the binding of analyte with the immobilized receptor [6].

1.1.3.2 Optimization of the reslonant layer

Two metals are mainly used in resonant layers for chemical sensors based on SPR – gold and silver. Only recently, aluminium also gained an attention due to its plasmonic properties in the blue range [66]. Gold is chemically much more stable than silver. On the other side, silver provides lower absorption losses in the visible and

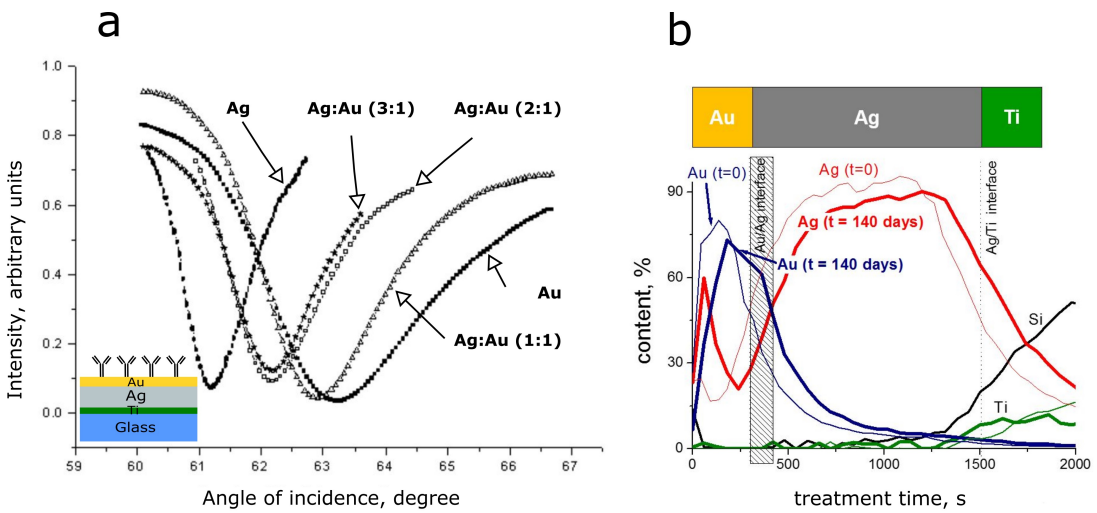

FIGURE 1.4: Bimetallic silver/gold (Ag/Au) resonant layers provide a more sharp surface plasmon resonance than gold solely (a) and were shown to be stable for at least 140 days at room temperature (b).

near infrared optical ranges; hence, it possesses a narrower resonance curve providing a higher SNR of SPR-based chemical sensors. To combine the advantages of both metals, a new structure of resonant metallic film based on bimetallic silver/gold (Ag/Au) layers was suggested (Fig. 1.4): a layer consisting mainly from silver but with a thin protective gold layer on the surface. An implementation of this idea for Ag/Au bimetallic layers with the ratio of thicknesses of 3:1 resulted in about 40% improvement of the SNR (Fig. 1.4a) [67]. This result was reproduced in [68]. It was also observed that thinner silver layers possess a high surface roughness limiting the sensor performance. The stability of the surface layer was so high that the authors have applied this sensor for electrochemical measurements; surprisingly, such sensors with immobilized receptors demonstrated a much higher improvement of SNR of up to 2.7. Later, bimetallic Au/Ag resonant layers were applied for sensitivity improvements in the experiments by the Biacore 3000 device [69]. The chips were stable during 6 cycles of measurements and regeneration.

The sensitivity of SPR sensors based on bimetallic layers of gold with silver, aluminium and copper was analyzed in [70]. It was shown that bimetallic Au/Ag resonant layers also increase the sensitivity of another type of SPR – long-range SPR [71]. Long range SPR is observed when a thin layer with low refractive index is deposited between glass prism and metallic resonant layer [72, 73]. This leads to a large increase of the penetration depth of evanescent wave and to a higher amplification of the magnitude of this wave. In this case, a substitution of the gold layer, separated from the glass prism by a 500–650 nm thick layer of magnesium fluoride, by a silver - gold bilayer resulted in a more sharp resonance [71]. The gold layer deposited on the surface of silver layer not only protects the silver layer against oxidative damage but also participates in the formation of resonant media for surface plasmons. However, it is

not necessary, and instead of gold, other chemically inert materials can be used. An interesting result was obtained in [74]: a deposition of 15–25 nm of titanium dioxide (TiO_2) on the surface of a silver resonant layer not only protects silver against oxidation but also increases the sensor sensitivity to changes of the refractive index for over 10 times. Discussions about Au/Ag bimetallic layers often lead to a criticism because of an expected very limited temporal stability: a mutual diffusion of metallic atom can lead to the formation of mixed metallic layer with poor chemical stability. However, an investigation of metal distribution performed by layer by layer laser ablation after 140 days storage at room temperature (the data were generously provided by Dr. A. Zybin) demonstrated that despite of measurable diffusion of silver atoms to the gold surface, the layered structure of the sample was still preserved (Fig. 1.4b).

There is a distinctly defined optimal thickness of the gold layer for defined refractive index of glass, resonant metal and dielectric phase near to the gold surface (e.g., water). Any deviation from the optimal geometry of layers leads to the less pronounced resonance. It was shown that even so small change of the root-mean-square (RMS) roughness as its increase from 1.31 to 1.40 nm leads to a decrease in sensor performance [75]. On the other hand, a formation of structures of the size comparable with the wavelength affects (like in nanostructured SPR sensors) the geometry of the evanescent wave. Considering a formation of these structures as an increase of roughness, one can expect less pronounced resonance peaks. In the same time, the change of the layer geometry due to formation of surface structures leads to the gradual change of the evanescent field from planar to spherical geometry resulting into a decrease of the penetration depth. Correspondingly, the influence of the adsorbed layer is amplified; the influence of the bulk phase on the SPR signal is attenuated. Such effect of SNR improvement was observed in [76, 77]. In contrary, in [78] only about 20% increase of sensitivity were observed. The increase of sensitivity for some types of columnar resonant films was studied experimentally and theoretically in [79, 80]. Notably, an increase of the microscopic area due to formation of different micro- and nanostructures increases possible number of immobilized receptor molecules.

A formation of nano- and microstructured resonant layers in a perspective may be a way for improvement of SPR sensors. However, it is a step into the direction of chemosensors based on localized SPR [81, 82] or terahertz metamaterials [83]; such sensing principles are out of scope of this chapter.

1.1.3.3 Optimization of the incident angle

In the approach with the fixed wavelength and incidence angle, the strongest SPR response (caused by a shift of the resonance curve) is observed when the incidence angle corresponds to the steepest part of the SPR curve. At such condition, the sensitivity (defined as $s = \frac{dR}{dn}$, where R is the reflectivity and n is the refractive index) exhibits its maximal value. Usually, SPR measurements are performed at this angle. [84, 85]: it provides the best detection limit if the noise is independent on the reflectivity. This

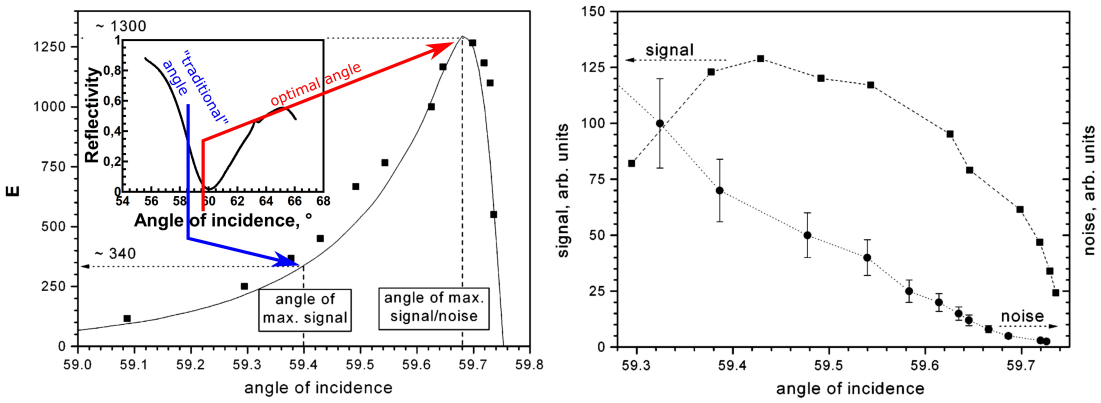

FIGURE 1.5: (a) Relative SPR sensitivity E in dependence on the reflection angle. Inset: resonance curve showing the measurement at "traditional" angle of incidence and in the optimized case. (b) SPR signal (squares) and corresponding noise (circles) measured in dependence on the angle of incidence. (Reproduced from [25])

may be the case if the noise level is determined by digitalization of the photodetector current. However, in the better-designed devices the noise is additionally determined by other factors, which lead to its dependence on the incidence angle. In particular, this is the case when a shot noise or fluctuations of the laser intensity are the main noise sources. Therefore, the noise dependence of the reflected intensity on the incidence angle should be taken into account for optimization of the detection limit. Such analysis was performed in [25]. The results of theoretical analysis demonstrate that for the case of shot noise the value $\frac{\frac{dR}{dn}}{\sqrt{R}}$ should be optimized instead of $\frac{dR}{dn}$ (Fig. 1.5). For detectors based on the charged coupled devices (CCD) at optimal light intensity or if the noise is limited by fluctuations of irradiation source, the value of $\frac{\frac{dR}{dn}}{R}$ should be optimized. These predictions were confirmed by experimental data [25]. Current fabrication technologies of gold-coated glasses for SPR applications cannot provide an exact thickness of resonant layer and its perfect smoothness. Therefore, even though SPR conditions are matched, the SPR reflectivity is not zero as it could be theoretically. In practice, some residual reflectivity is observed instead. Therefore, an enhancement of the SNR by optimization of the incidence angle requires measurements of the relative sensitivity versus the incidence angle for each gold-coated glass substrate. This is time consuming and can hardly be realized. However, taking into account that $\frac{dR}{dn}$ is proportional to $\frac{dR}{d\theta}$, an optimization of angle (for the case of CCD noise or fluctuations of light intensity) can be obtained from the angle dependence of reflectivity as a maximum of the absolute value of $\frac{\frac{dR}{d\theta}}{R}$. In analogy, for the shot noise the value of $\frac{\frac{dR}{d\theta}}{\sqrt{R}}$ can be optimized, as well. The measurements of the angle dependencies are provided by many commercial SPR devices. The analysis of this dependence calculated from experimental data (using Biosuplar-321 SPR spectrometer, $\lambda = 650$ nm, 50 nm Au on glass with $n = 1.6$) shows the value of the optimal angle to be ~ 0.2 ° before the resonance angle for negligible residual reflectivity and ~ 0.6 ° before the resonance angle

for 9% residual reflectivity.

The application of this optimization resulted into an improvement of the SNR for ~ 2 times for CCD detection or for ~ 3.5 times for photodiode detection in comparison with the measurements at maximal sensitivity. However, the calibration curve (SPR response dR versus dn change of effective refractive index) at the angle of enhanced detection power deviates more from linear dependency compared to such calibration curve at traditional incidence angle. For most of SPR applications, such deviation is tolerable and can be corrected by calibration. The developed approach was further applied for numerous applications including the detection of nanoparticles by wide-field SPR microscopy [86–90].

1.1.3.4 Instrumental improvement of SPR sensitivity

A number of techniques for improvement of SPR sensitivity is based on the development of new measurement technologies without any modification of the resonant- or receptor layers. Some of them, which include a referencing relative to the bulk phase, form a large and special group of SPR techniques and will be discussed in the next section. A drastic improvement of SPR sensitivity can be achieved by measuring the phase shift of the reflected light [91–96], however, this requires complicated, often environment susceptible, optical setups. Along with that, without further complication of measurement principle, the high sensitivity leads to a small measurement range. For these reasons, in practical applications the intensity-sensitive SPR sensors have found much wider adoption than phase-sensitives ones.

An improvement of sensitivity was reached by using a bi-cell photodetector [97]: a small shift in the position of SPR minimum angle is detected as the differential signal of this photodetector. A normalization of the differential signal to the sum of the photodiode signals allowed one to exclude an influence of ambient light.

Several methods based on modulation techniques were suggested. The method based on small modulation of the incidence angle by a piezo-electrical actuator was reported in [98]. At resonance conditions, the reflectance signal detected by a lock-in amplifier equals to zero. The resonance shifts are measured as a deviation from zero or through a feedback signal, which adjusts the angle of incidence to match resonance conditions changed due to the sorption. Another modulation-based approach was realized by means of a tuneable acousto-optical filter [99].

Zybin *et al.* suggested a modulation based on using two lasers with different wavelengths [100]. This idea was implemented by using the wavelength modulation without moving instrumental components. Unlike spectroscopic scanning of the wavelength, in the double-wavelength approach only two laser beams with different wavelengths irradiate in parallel the same surface area [100]. Illumination conditions are chosen so that for given SPR conditions the corresponding photodetector currents are equal (Fig. 1.6). However, the shift of SPR conditions will destroy this balance and resulting into an alternative current (AC) signal at the photodiode. Hence, AC signal

value was used to characterize the SPR shift and, consequently, the adsorption processes. Such referencing allows compensating not only the effect of ambient and/or scattered light but also of possible change in the resonance width. Later, this approach was extended for imaging [101]. A detection limit of $\Delta n \sim 2 \times 10^{-6}$ was achieved. However, this double-wavelength approach was realized exploiting lasers with very close wavelengths – 785 nm and 830 nm – leading to similar penetration depths of their evanescent waves: ~ 340 nm and ~ 380 nm, correspondingly [64]. The small difference between the penetration depths did not allow one to apply this approach for referencing to separate bulk and volume effects; therefore, it was performed by traditional macroscopic spatial referencing (section 2.1).

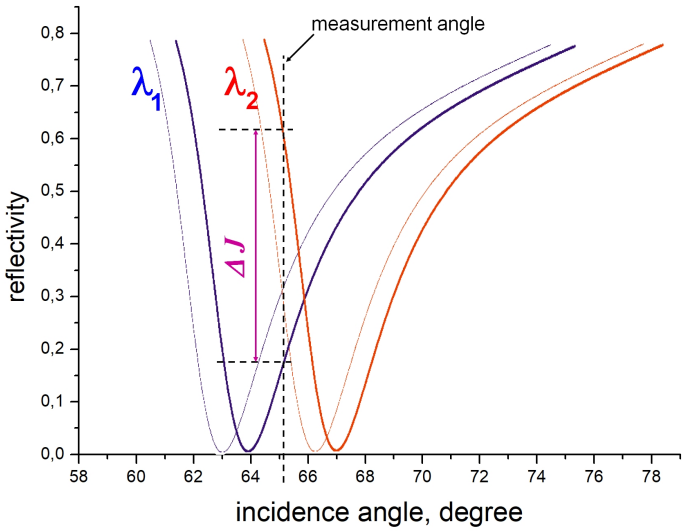

FIGURE 1.6: Differential SPR measurement at two wavelengths. The measurement point corresponds to the negative and positive slopes of the shorter (λ_1) and longer (λ_2) wavelengths, correspondingly.

References

[1] F. E. Bartell and C. K. Sloan, "An interferometric investigation of adsorption by pure carbon from non-aqueous binary systems," *J. Am. Chem. Soc.*, vol. 584, no. 1927, pp. 1637–1643, 1929.

[2] B. B. Damaskin, O. A. Petrii, and V. Batrakov, *Adsorption of Organic Compounds on Electrodes*. Plenum Press, New York, 1972.

[3] G. Sauerbrey, "Verwendung von Schwingquarzen zur Wägung dünner Schichten und zur Mikrowägung," *Z. Phys.*, vol. 155, no. 2, pp. 206–222, 1959.

[4] W. H. King, "Piezoelectric sorption detector," *Anal. Chem.*, vol. 36, no. 9, pp. 1735–1739, 1964.

[5] B. Liedberg, C. Nylander, and I. Lunström, "Surface plasmon resonance for gas detection and biosensing," *Sens. Actuator.*, vol. 4, no. C, pp. 299–304, 1983.

[6] S. Lofas, M. Malmqvist, I. Ronnberg, E. Stenberg, B. Liedberg, and I. Lundstrom, "Bioanalysis with surface plasmon resonance," *Sens. Actuators, B*, vol. 5, no. 1-4, pp. 79–84, 1991.

[7] B. Liedberg, C. Nylander, and I. Lundström, "Biosensing with surface plasmon resonance - how it all started," *Biosens. Bioelectron.*, vol. 10, no. 8, pp. 1–9, 1995.

[8] J. Homola, *Surface Plasmon Resonance Based Sensors*. Springer, 2006.

[9] R. B. M. Schasfoort and A. McWhirter, "SPR Instrumentation," *Handb. Surf. Plasmon Reson.*, pp. 35–80, 2008.

[10] J. Homola, "Present and future of surface plasmon resonance biosensors," *Anal. Bioanal. Chem.*, vol. 377, no. 3, pp. 528–539, 2003.

[11] G. Safina, "Application of surface plasmon resonance for the detection of carbohydrates, glycoconjugates, and measurement of the carbohydrate-specific interactions: a comparison with conventional analytical techniques. A critical review.," *Anal. Chim. Acta*, vol. 712, pp. 9–29, jan 2012.

[12] X. D. Hoa, A. G. Kirk, and M. Tabrizian, "Towards integrated and sensitive surface plasmon resonance biosensors: a review of recent progress.," *Biosens. Bioelectron.*, vol. 23, pp. 151–60, sep 2007.

[13] J. Homola, S. S. Yee, and G. Gauglitz, "Surface plasmon resonance sensors: review," *Sensors Actuators B Chem.*, vol. 54, no. 1, pp. 3–15, 1999.

[14] M. Puiu and C. Bala, "SPR and SPR imaging: recent trends in developing nanodevices for detection and real-time monitoring of biomolecular events," *Sensors*, vol. 16, no. 6, p. 870, 2016.

[15] E. Kretschmann and H. Raether, "Radiative decay of non-radiative surface plasmons excited by light," *Z. Naturforsch.*, vol. 23, no. November 1968, pp. 2135–2136, 1968.

[16] A. D. Boardman, *Electromagnetic Surface Modes*. Chichester; New York: Wiley, 1982.

[17] H. Raether, *Surface Plasmons on Smooth and Rough Surfaces and on Gratings*. 1988.

[18] S. Nizamov, V. Scherbahn, and V. M. Mirsky, "Self-referencing SPR-sensor based on integral measurements of light intensity reflected by arbitrarily distributed sensing and referencing spots," *Sensors Actuators B Chem.*, vol. 207, pp. 740–747, 2015.

[19] L. S. Jung, C. T. Campbell, T. M. Chinowsky, M. N. Mar, and S. S. Yee, "Quantitative interpretation of the response of surface plasmon resonance sensors to adsorbed films," *Langmuir*, vol. 14, no. 19, pp. 5636–5648, 1998.

[20] T. L. Mcmeekin, M. Wilensky, and M. L. Groves, "Refractive indeces of proteins in relation to amino acid composition and specific volume," *Biochem. Biophys. Commun.*, vol. 7, no. 2, pp. 151–156, 1962.

[21] R. Barer and S. Tkaczyk, "Refractive index of concentrated protein solutions," *Nature*, vol. 173, no. 4409, pp. 821–822, 1954.

[22] J. Vörös, "The density and refractive index of adsorbing protein layers," *Biophys. J.*, vol. 87, no. 1, pp. 553–561, 2004.

[23] F. Klemm, R. Johnson, and V. M. Mirsky, "Binding of protein nanoparticles to immobilized receptors," *Sensors Actuators B*, vol. 208, pp. 616–621, 2015.

[24] B. Liedberg, I. Lundström, and E. Stenberg, "Principles of biosensing with an extended coupling matrix and surface plasmon resonance," *Sensors Actuators B. Chem.*, vol. 11, no. 1-3, pp. 63–72, 1993.

[25] A. Zybin, D. Boecker, V. M. Mirsky, and K. Niemax, "Enhancement of the detection power of surface plasmon resonance measurements by optimization of the reflection angle," *Anal. Chem.*, vol. 79, no. 11, pp. 4233–4236, 2007.

[26] T. Akimoto, S. Sasaki, K. Ikebukuro, and I. Karube, "Effect of incident angle of light on sensitivity and detection limit for layers of antibody with surface plasmon resonance spectroscopy," *Biosens. Bioelectron.*, vol. 15, no. 7-8, pp. 355–362, 2000.

[27] N. S. Eum, D. E. Kim, S. H. Yeom, B. H. Kang, K. J. Kim, C. S. Park, and S. W. Kang, "Variable wavelength surface plasmon resonance (SPR) in biosensing," *BioSystems*, vol. 98, no. 1, pp. 51–55, 2009.

[28] T. Akimoto, S. Wada, and I. Karube, "A surface plasmon resonance probe without optical fibers as a portable sensing device," *Anal. Chim. Acta*, vol. 610, no. 1, pp. 119–124, 2008.

[29] B. P. Nelson, A. G. Frutos, J. M. Brockman, and R. M. Corn, "Near-infrared surface plasmon resonance measurements of ultrathin films," *Anal. Chem.*, vol. 71, no. 18, pp. 3928–3934, 1999.

[30] A. G. Frutos, S. C. Weibel, and R. M. Corn, "Near-infrared surface plasmon resonance measurements of ultrathin films. 2. Fourier transform SPR spectroscopy," *Anal. Chem.*, vol. 71, no. 18, pp. 3935–3940, 1999.

[31] B. Rothenhausler and W. Knoll, "Surface plasmon microscopy," *Nature*, vol. 332, pp. 615–617, apr 1988.

[32] J. M. Brockman, B. P. Nelson, and R. M. Corn, "Surface plasmon resonance imaging measurements of ultrathin organic films," *Annu. Rev. Phys. Chem.*, vol. 51, pp. 41–63, 2000.

[33] C. T. Campbell and G. Kim, "SPR microscopy and its applications to high-throughput analyses of biomolecular binding events and their kinetics," *Biomaterials*, vol. 28, no. 15, pp. 2380–2392, 2007.

[34] D. Boecker, A. Zybin, K. Niemax, C. Grunwald, and V. M. Mirsky, "Noise reduction by multiple referencing in surface plasmon resonance imaging," *Rev. Sci. Instrum.*, vol. 79, no. 2, pp. 2–8, 2008.

[35] C. E. H. Berger, T. A. M. Beumer, R. P. H. Kooyman, and J. Greve, "Surface plasmon resonance multisensing," *Anal. Chem.*, vol. 70, no. 4, pp. 703–706, 1998.

[36] X. Guo, "Surface plasmon resonance based biosensor technique: a review," *J. Biophotonics*, vol. 5, no. 7, pp. 483–501, 2012.

[37] C. Nylander, B. Liedberg, and T. Lind, "Gas detection by means of surface plasmon resonance," *Sensors and Actuators*, vol. 3, no. C, pp. 79–88, 1982.

[38] R. G. Nuzzo and D. L. Allara, "Adsorption of bifunctional organic disulfides on gold surfaces," *J. Am. Chem. Soc.*, vol. 105, no. 13, pp. 4481–4483, 1983.

[39] A. Ulman, "Formation and structure of self-assembled monolayers," *Chem. Rev.*, vol. 96, no. 4, pp. 1533–1554, 1996.

[40] M. Riepl, V. M. Mirsky, I. Novotny, V. Tvarozek, V. Rehacek, and O. S. Wolfbeis, "Optimization of capacitive affinity sensors: Drift suppression and signal amplification," *Anal. Chim. Acta*, vol. 392, no. 1, pp. 77–84, 1999.

[41] V. M. Mirsky, "New electroanalytical applications of self-assembled monolayers," *Trends Anal. Chem.*, vol. 21, no. 6-7, pp. 439–450, 2002.

[42] J. C. Love, L. A. Estroff, J. K. Kriebel, R. G. Nuzzo, and G. M. Whitesides, "Self-assembled monolayers of thiolates on metals as a form of nanotechnology," *Chem. Rev.*, vol. 105, no. 4, pp. 1103–1169, 2005.

[43] T. Hirsch, A. Shaporenko, V. M. Mirsky, and M. Zharnikov, "Monomolecular films of phthalocyanines: formation, characterization, and expelling by alkanethiols," *Langmuir*, vol. 23, no. 8, pp. 4373–4377, 2007.

[44] A. Stewart, S. Zheng, M. R. McCourt, and S. E. J. Bell, "Controlling assembly of mixed thiol monolayers on silver nanoparticles to tune their surface properties," *ACS Nano*, vol. 6, no. 5, pp. 3718–3726, 2012.

[45] R. M. Crooks and A. J. Ricco, "New organic materials suitable for use in chemical sensor arrays," *Acc. Chem. Res.*, vol. 31, no. 5, pp. 219–227, 1998.

[46] U. Glebe, J. E. Baio, L. Árnadóttir, U. Siemeling, and T. Weidner, "Molecular suction pads: Self-assembled monolayers of subphthalocyaninatoboron complexes [BCl{Subpc'(SR)6 }] on gold," *ChemPhysChem*, vol. 14, no. 6, pp. 1155–1160, 2013.

[47] S. Ferretti, S. Paynter, D. A. Russell, K. E. Sapsford, and D. J. Richardson, "Self-assembled monolayers: a versatile tool for the formulation of bio-surfaces," *Trends Anal. Chem.*, vol. 19, no. 9, pp. 530–540, 2000.

[48] N. Faucheux, R. Schweiss, K. Lützow, C. Werner, and T. Groth, "Self-assembled monolayers with different terminating groups as model substrates for cell adhesion studies," *Biomaterials*, vol. 25, no. 14, pp. 2721–2730, 2004.

[49] E. Ostuni, L. Yan, and G. M. Whitesides, "The interaction of proteins and cells with self-assembled monolayers of alkanethiolates on gold and silver," *Colloids and Surfaces B-Biointerfaces*, vol. 15, no. 1, pp. 3–30, 1999.

[50] J. B. Schlenoff, M. Li, and H. Ly, "Stability and self-exchange in alkanethiol monolayers," *J. Am. Chem. Soc.*, vol. 117, no. 50, pp. 12528–12536, 1995.

[51] J. Noh, H. S. Kato, M. Kawai, and M. Hara, "Surface and adsorption structures of dialkyl sulfide self-assembled monolayers on Au(111)," *J. Phys. Chem. B*, vol. 106, no. 51, pp. 13268–13272, 2002.

[52] N. Phares, R. J. White, and K. W. Plaxco, "Improving the stability and sensing of electrochemical biosensors by employing trithiol-anchoring groups in a six-carbon self-assembled monolayer," *Anal. Chem.*, vol. 81, no. 3, pp. 1095–1100, 2009.

[53] Z. Li, R. Jin, C. A. Mirkin, and R. L. Letsinger, "Multiple thiol-anchor capped DNA-gold nanoparticle conjugates.," *Nucleic Acids Res.*, vol. 30, no. 7, pp. 1558–1562, 2002.

[54] G. T. Hermanson, *Bioconjugate Techniques*. Academic Press, third edit ed., 2013.

[55] N. K. Chaki and K. Vijayamohanan, "Self-assembled monolayers as a tunable platform for biosensor applications," *Biosens. Bioelectron.*, vol. 17, no. 1-2, pp. 1–12, 2002.

[56] J. J. Gooding and D. B. Hibbert, "The application of alkanethiol self-assembled monolayers to enzyme electrodes," *Trends Anal. Chem.*, vol. 18, no. 8, pp. 525–533, 1999.

[57] N. Wrobel, M. Schinkinger, and V. M. Mirsky, "A novel ultraviolet assay for testing side reactions of carbodiimides.," *Anal. Biochem.*, vol. 305, no. 2, pp. 135–138, 2002.

[58] H. Yamada, T. Imoto, K. Fujita, K. Okazaki, and M. Motomura, "Selective modification of aspartic acid-101 in lysozyme by carbodiimide reaction.," *Biochemistry*, vol. 20, no. 17, pp. 4836–4842, 1981.

[59] Z. Pei, H. Anderson, A. Myrskog, G. Dunér, B. Ingemarsson, and T. Aastrup, "Optimizing immobilization on two-dimensional carboxyl surface: pH dependence of antibody orientation and antigen binding capacity," *Anal. Biochem.*, vol. 398, no. 2, pp. 161–168, 2010.

[60] B. Johnsson, S. Löfås, and G. Lindquist, "Immobilization of proteins to a carboxymethyldextran-modified gold surface for biospecific interaction analysis in surface plasmon resonance sensors," *Anal. Biochem.*, vol. 198, no. 2, pp. 268–277, 1991.

[61] H. C. Kolb, M. G. Finn, and K. B. Sharpless, "Click chemistry: diverse chemical function from a few good reactions," *Angew. Chemie - Int. Ed.*, vol. 40, no. 11, pp. 2004–2021, 2001.

[62] J. Mehlich and B. J. Ravoo, "Click chemistry by microcontact printing on self-assembled monolayers: a structure–reactivity study by fluorescence microscopy," *Org. Biomol. Chem.*, vol. 9, no. 11, pp. 4108–4415, 2011.

[63] G. Fleminger, E. Hadas, T. Wolf, and B. Solomon, "Oriented immobilization of periodate-oxidized monoclonal antibodies on amino and hydrazide derivatives of Eupergit C.," *Appl. Biochem. Biotechnol.*, vol. 23, no. 2, pp. 123–37, 1990.

[64] S. Nizamov and V. M. Mirsky, "Self-referencing SPR-biosensors based on penetration difference of evanescent waves.," *Biosens. Bioelectron.*, vol. 28, pp. 263–269, oct 2011.

[65] L. G. Fägerstam, Å. Frostell-Karlsson, R. Karlsson, B. Persson, and I. Rönnberg, "Biospecific interaction analysis using surface plasmon resonance detection applied to kinetic, binding site and concentration analysis," *J. Chromatogr. A*, vol. 597, no. 1-2, pp. 397–410, 1992.

[66] M. W. Knight, N. S. King, L. Liu, H. O. Everitt, P. Nordlander, and N. J. Halas, "Aluminum for plasmonics," *ACS Nano*, vol. 8, no. 1, pp. 834–840, 2014.

[67] S. A. Zynio, A. V. Samoylov, E. R. Surovtseva, V. M. Mirsky, and Y. M. Shirshov, "Bimetallic layers increase sensitivity of affinity sensors based on surface plasmon resonance," *Sensors*, vol. 2, pp. 62–70, 2002.

[68] P. Zhai, J. Guo, J. Xiang, and F. Zhou, "Electrochemical Surface Plasmon Resonance Spectroscopy at Bilayered Silver/Gold Films," *J. Phys. Chem. C*, vol. 111, no. 2, pp. 981–986, 2007.

[69] Y. Chen, R. S. Zheng, D. G. Zhang, Y. H. Lu, P. Wang, H. Ming, Z. F. Luo, and Q. Kan, "Bimetallic chips for a surface plasmon resonance instrument.," *Appl. Opt.*, vol. 50, no. 3, pp. 387–391, 2011.

[70] D. Nesterenko, R. Saif Ur, and Z. Sekkat, "Surface plasmon sensing with different metals in single and double layer configurations," *Appl. Opt.*, vol. 51, no. 27, pp. 6673–6682, 2012.

[71] M. Zekriti, D. Nesterenko, and Z. Sekkat, "Long-range surface plasmons supported by a bilayer metallic structure for sensing applications," *Appl. Opt.*, vol. 54, no. 8, pp. 2151–2157, 2015.

[72] R. Slavík and J. Homola, "Simultaneous excitation of long and short range surface plasmons in an asymmetric structure," *Opt. Commun.*, vol. 259, pp. 507–512, mar 2006.

[73] J. T. Hastings, J. Guo, P. D. Keathley, P. B. Kumaresh, Y. Wei, S. Law, and L. G. Bachas, "Optimal self-referenced sensing using long- and short- range surface plasmons.," *Opt. Express*, vol. 15, pp. 17661–17672, dec 2007.

[74] S. H. El-Gohary, M. Choi, Y. L. Kim, and K. M. Byun, "Dispersion curve engineering of TiO2/silver hybrid substrates for enhanced surface plasmon resonance detection," *Sensors*, vol. 16, no. 9, pp. 1442–1452, 2016.

[75] X. Chen, M. Pan, and K. Jiang, "Sensitivity enhancement of SPR biosensor by improving surface quality of glass slides," *Microelectron. Eng.*, vol. 87, no. 5-8, pp. 790–792, 2010.

[76] C. Genslein, P. Hausler, E.-M. Kirchner, R. Bierl, A. J. Baeumner, and T. Hirsch, "Detection of small molecules with surface plasmon resonance by synergistic plasmonic effects of nanostructured surfaces and graphene," *Procedings SPIE*, vol. 10080, no. 100800F-4, 2017.

[77] C. Genslein, P. Hausler, E. M. Kirchner, R. Bierl, A. J. Baeumner, and T. Hirsch, "Graphene-enhanced plasmonic nanohole arrays for environmental sensing in aqueous samples," *Beilstein J. Nanotechnol.*, vol. 7, no. 1, pp. 1564–1573, 2016.

[78] K. Pang, W. Dong, B. Zhang, S. Zhan, and X. Wang, "Sensitivity-enhanced and noise-reduced surface plasmon resonance sensing with microwell chips," *Meas. Sci. Technol.*, vol. 26, no. 085104, p. 8pp, 2015.

[79] A. Shalabney and I. Abdulhalim, "Electromagnetic fields distribution in multilayer thin film structures and the origin of sensitivity enhancement in surface plasmon resonance sensors," *Sensors Actuators, A Phys.*, vol. 159, no. 1, pp. 24–32, 2010.

[80] A. Shalabney, C. Khare, B. Rauschenbach, and I. Abdulhalim, "Sensitivity of surface plasmon resonance sensors based on metallic columnar thin films in the spectral and angular interrogations," *Sensors Actuators, B Chem.*, vol. 159, no. 1, pp. 201–212, 2011.

[81] A. Vaskevich and I. Rubinstein, "Localized Surface Plasmon Resonance (LSPR) Spectroscopy in Biosensing," in *Handb. Biosens. Biochips*, p. Four:26, 2008.

[82] O. Kedem, A. B. Tesler, A. Vaskevich, and I. Rubinstein, "Sensitivity and optimization of localized surface plasmon resonance transducers," *ACS Nano*, vol. 5, no. 2, pp. 748–760, 2011.

[83] C. Drexler, T. Shishkanova, C. Lange, S. N. Danilov, D. Weiss, S. D. Ganichev, and V. M. Mirsky, "Terahertz split-ring metamaterials as transducers for chemical sensors based on conducting polymers: a feasibility study with sensing of acidic and basic gases using polyaniline chemosensitive layer," *Microchim. Acta*, vol. 181, no. 15-16, pp. 1857–1862, 2014.

[84] J. Shumaker-Parry and C. Campbell, "Quantitative methods for spatially resolved adsorption/desorption measurements in real time by surface plasmon resonance microscopy," *Anal. Chem*, vol. 76, no. 4, pp. 918–929, 2004.

[85] B. P. Nelson, T. E. Grimsrud, M. R. Liles, R. M. Goodman, and R. M. Corn, "Surface plasmon resonance imaging measurements of DNA and RNA hybridization adsorption onto DNA microarrays," *Anal. Chem.*, vol. 73, no. 1, pp. 1–7, 2001.

[86] A. Zybin, Y. A. Kuritsyn, E. L. Gurevich, V. Temchura, K. Überla, and K. Niemax, "Real-time detection of single immobilized nanoparticles by surface plasmon resonance imaging," *Plasmonics*, vol. 5, no. 1, pp. 31–35, 2010.

[87] A. Zybin, V. Shpacovitch, J. Skolnik, and R. Hergenröder, "Optimal conditions for SPR-imaging of nano-objects," *Sensors Actuators, B Chem.*, vol. 239, pp. 338–342, 2016.

[88] S. Nizamov, O. Kasian, and V. M. Mirsky, "Individual detection and electrochemically assisted identification of adsorbed nanoparticles by using surface plasmon microscopy," *Angew. Chemie - Int. Ed.*, vol. 55, pp. 1–6, 2016.

[89] S. Nizamov, V. Scherbahn, and V. M. Mirsky, "Detection and quantification of single engineered nanoparticles in complex samples using template matching in wide-field surface plasmon microscopy," *Anal. Chem.*, vol. 88, no. 20, pp. 10206–10214, 2016.

[90] V. Scherbahn, S. Nizamov, and V. M. Mirsky, "Plasmonic detection and visualization of directed adsorption of charged single nanoparticles to patterned surfaces," *Microchim. Acta*, vol. 183, no. 11, pp. 2837–2845, 2016.

[91] A. N. Grigorenko, A. A. Beloglazov, P. I. Nikitin, C. Kuhne, G. Steiner, and R. Salzer, "Dark-field surface plasmon resonance microscopy," *Opt. Commun.*, vol. 174, no. January, pp. 151–155, 2000.

[92] A. Kabashin and P. Nikitin, "Interferometer based on a surface-plasmon resonance for sensor applications," *Quantum Electron.*, vol. 27, no. 7, pp. 653–655, 1997.

[93] P. I. Nikitin, A. N. Grigorenko, A. Beloglazov, M. V. Valeiko, A. I. Savchuk, O. A. Savchuk, G. Steiner, C. Kuhne, A. Huebner, and R. Salzer, "Surface plasmon resonance interferometry for micro-array biosensing," *Sensors Actuators, A Phys.*, vol. 85, no. 1, pp. 189–193, 2000.

[94] S. G. Nelson, K. S. Johnston, and S. S. Yee, "High sensitivity surface plasmon resonace sensor based on phase detection," *Sensors Actuators B Chem.*, vol. 35, no. 1-3, pp. 187–191, 1996.

[95] M. Piliarik, H. Vaisocherová, and J. Homola, "A new surface plasmon resonance sensor for high-throughput screening applications," *Biosens. Bioelectron.*, vol. 20, no. 10 SPEC. ISS., pp. 2104–2110, 2005.

[96] M. Kashif, A. Bakar, N. Arsad, and S. Shaari, "Development of phase detection schemes based on surface plasmon resonance using interferometry," *Sensors*, vol. 14, no. 9, pp. 15914–15938, 2014.

[97] N. J. Tao, S. Boussaad, W. L. Huang, R. A. Arechabaleta, and J. D'Agnese, "High resolution surface plasmon resonance spectroscopy," *Rev. Sci. Instrum.*, vol. 70, no. 12, pp. 4656–4660, 1999.

[98] C. E. H. Berger and J. Greve, "Differential SPR immunosensing," *Sensors Actuators, B Chem.*, vol. 63, no. 1, pp. 103–108, 2000.

[99] M. J. Jory, G. W. Bradberry, P. S. Cann, and J. R. Sambles, "A surface-plasmon-based optical sensor using acousto-optics," *Meas. Sci. Technol.*, vol. 6, no. 8, pp. 1193–1200, 1995.

[100] A. Zybin, C. Grunwald, V. M. Mirsky, J. Kuhlmann, O. S. Wolfbeis, and K. Niemax, "Double-wavelength technique for surface plasmon resonance

measurements: basic concept and applications for single sensors and two-dimensional sensor arrays.," *Anal. Chem.*, vol. 77, pp. 2393–2399, apr 2005.

[101] D. Boecker, A. Zybin, V. Horvatic, C. Grunwald, and K. Niemax, "Differential surface plasmon resonance imaging for high-throughput bioanalyses," *Anal. Chem.*, vol. 79, no. 2, pp. 702–709, 2007.

1.2 Aim and scope of the thesis

Among optical measurement techniques, surface plasmon resonance (SPR) and its extensions SPR imaging (SPRi) or SPR microscopy (SPRM) have become key technologies to sensitively measure and monitor binding/affinity processes on surfaces. In spite of a comparable high sensitivity, the SPR is still under continuous development regarding instrumental and methodological aspects. The major drawback, intrinsically accompanying SPR measurements, is the separation between the signal obtained by surface interactions and that due to bulk effects (section 1.1.2). By overcoming this issue, a higher signal-to-noise-ratio (SNR) is expected resulting in a lower limit of detection (LOD). Within this scope, several approaches were suggested to improve the performance of SPR sensing e.g. by optimization of the receptor and resonant layers as well as of the measurement setup and instrumentation (section 1.1.3).

The main goal of this thesis relies on application of different techniques and tools to improve the performance in SPR sensing. Two main directions were pursued to attain this goal: (1) implementation of an internal referencing and (2) application of wide-field (WF)-SPRM to detect single nanoparticles on modified surfaces. The results are presented as four published articles referring to sections 2.1–2.4 and as one article in preparation referring to section 2.5.

The first task of the present thesis was to realize a self-referencing SPR sensor based on heterogeneously micro-patterned self-assembled monolayers (SAM) consisting of sensing and referencing areas. To develop such micro-patterned SAM – key feature enabling the self-referencing effect – a contact-less dispensing (spotting) technique was applied. The results are part of section 2.1. In order to assess, mainly to visualize, the micro-patterned SAM, an ionic referencing in wide-field (WF)-SPRM was implemented, which is considered as the second task of the thesis. This approach relies on application of electrolytes with a high molar refraction of either anions or cations to patterned SAM bearing different functional surface properties. The results are described in section 2.2.

The third task, in the same time representing the second direction of this work, was to apply the WF-SPRM technology in combination with spatio-temporal referencing to detect, to visualize and to characterize single nanoparticles on modified surfaces (sections 2.3–2.5). In the first part, WF-SPRM was applied to investigate adsorption behavior of single nanoparticles from simple aqueous media to both homogeneous and heterogeneous, micro-patterned surface coatings bearing different properties (section 2.3). Whereas in the second part, unlike in simple aqueous media, a template matching approach in WF-SPRM was applied to detect and to quantify single engineered nanoparticles in complex media such as wine, juice and sun cream (section 2.4). In the third part, the WF-SPRM technology was applied to detect, to visualize and to quantify enzymatically formed nanoparticles. This approach was suggested as a promising base for novel ultra-sensitive (bio)sensing applications (section 2.5).

2. Results

The results are presented as four published articles in peer-reviewed journals (sections 2.1–2.4) and as one manuscript in preparation (section 2.5) to be submitted to a peer-reviewed journal.

Section 2.1: Self-referencing SPR-sensor based on integral measurements of light intensity reflected by arbitrarily distributed sensing and referencing spots

Section 2.2: Ionic referencing in surface plasmon microscopy: visualization of the difference in surface properties of patterned monomolecular layers

Section 2.3: Plasmonic detection and visualization of directed adsorption of charged single nanoparticles to patterned surfaces

Section 2.4: Detection and quantification of single engineered nanoparticles in complex samples using template matching in wide-field surface plasmon microscopy

Section 2.5: Plasmonic detection and visualization of single enzymatically synthesized nanoparticles by means of wide-field surface plasmon resonance microscopy

2.1 Self-referencing SPR-sensor based on integral measurements of light intensity reflected by arbitrarily distributed sensing and referencing spots

NIZAMOV, S., SCHERBAHN, V., & MIRSKY, V. M.

Published in: Sensors and Actuators B: Chemical, 207, 740–747. (2015)
DOI: 10.1016/j.snb.2014.10.022

2.1.1 Abstract

A new approach for self-referencing in SPR biosensors is reported. The method is technologically simple and applicable for a wide range of existing SPR instrumentation with Kretschmann configuration. It is based on the micropatterning of the sensor area with sensing and referencing areas whose shape and distribution can be chosen arbitrarily and their characteristic sizes are larger than the plasmons propagation length. Provided that roughly a half of the area is used as the sensing area while its optical thickness is different from that of the referencing area, an integral measurement of the intensity of the reflected light over such a patterned surface near the summary resonance conditions exhibits self- referencing properties. An over ten-fold suppression of the effect caused by the variation of the bulk refractive index was observed.

2.1.2 Introduction

Since the introduction of biosensors based on surface plasmon resonance (SPR) [1], they quickly become one of the most popular transducing approaches in affinity sensors [2]. SPR transducers are sensitive to the refractive index of surrounding media. Because an increase of the refractive index near sensing surface is a direct consequence of adsorption, this approach can be applied for different analytes: biopolymers (proteins, DNA etc), toxins, drugs, ions, etc [3]. However, such versatility has also a drawback: the SPR sensors are sensitive to many other effects which also influence the refractive index of media.

In the typical case of implementation of SPR biosensing technologies, a parallel p-polarized light beam is reflected from thin metallic layer deposited on the surface of glass (see Fig. 2.1a). The reflectivity (ratio of reflected and incident light intensities) in such case depends on the coupling condition of incident light to surface plasmons, which is described by well-known relation for the wavenumber k_x:

$$k_x = \frac{2\pi}{\lambda}\sqrt{\frac{\epsilon_1\epsilon_2}{\epsilon_1+\epsilon_2}} = \frac{2\pi}{\lambda}\sqrt{\epsilon_0}\sin\theta \tag{2.1}$$

where λ is the free-space wavelength of incident light, its incidence angle, ϵ_0 , ϵ_1 and ϵ_2 are dielectric permittivities of the glass, metal film and aqueous solution correspondingly. A plot of the reflectivity of SPR biosensor versus incidence angle (and/or wavelength) shows a strongly pronounced dip, whose exact position and shape depends also on ϵ_2 thus providing information on the environment near exposed metal surface (Fig. 2.1a). On Fig. 2.1 such curves are shown for SPR biosensor consisting of 50 nm gold layer with 2 nm Cr adhesion layer deposited on the coupling prism with high refractive index (F2, n = 1.6). The gold layer is exposed to water. The deposition of a thin organic layer on the gold surface shifts the curve to the right (see Fig.2.1b). This shift characterizes the thickness and the refractive index of the layer. In many cases both incidence angle and wavelength of the incident light are fixed. Such case is shown in the Fig. 2.1c: the light with the wavelength 650 nm is incident at an angle of 64°. In response to increasing thickness of the organic layer a shift of the SPR curve to the right is observed, this leads to an increase of intensity of the reflected light. Usually the point with the highest slope on the descending part of SPR curve is taken (like shown at 64°). This is not a mandatory requirement, moreover, fixing of the incidence angle closer to the SPR minimum (e.g. at 65°) improves signal to noise ratio even despite the loss of the absolute magnitude in of the light intensity changes [4]. If the incidence angle is larger than the resonance angle (Fig. 2.1c, 68° curve), the sensor response becomes negative: an increase in the thickness of the organic layer results in the decrease in the reflected light intensity.

However, SPR curves are shifted not only because of the changes of layer thickness or its composition: a contribution of the bulk solution behind this layer might be even more important. The SPR-sensor measures the change of the effective refractive index near metal surface [5]:

$$n_{eff} = \frac{2}{z_2} \int n_2(z) e^{\frac{-2z}{z_2}} dz \tag{2.2}$$

where $n_2(z)$ is the distribution of refractive index in aqueous media defined by dielectric permittivity of adsorbed layer ϵ_p and bulk aqueous solution ϵ_a, z_2 is the penetration depth of the evanescent wave. For the described sensor layout the penetration depth is about 190 nm, therefore the contribution of a few nm's thick organic layer is much smaller than the contribution of the bulk solution. It leads to cross-sensitivity of SPR sensor to variations of solute concentration or temperature. This is especially critical in many biosensing applications: a change of temperature for 0.1 °C would lead to changes of the refractive index for 8×10^{-6} [6], which is higher than the effect due to adsorption of analytes with low molecular weight. That is why the referencing in SPR biosensors is very important, otherwise the useful signal can be masked by changes of the refractive index in the bulk.

A number of referencing approaches for SPR sensors were suggested. A common approach is based on introduction of a dedicated referencing channel, spatially separated from the sensing one and coated by a material with a decreased affinity to the analyte of interest. Subtracting the signal of the referencing channel from the signal of

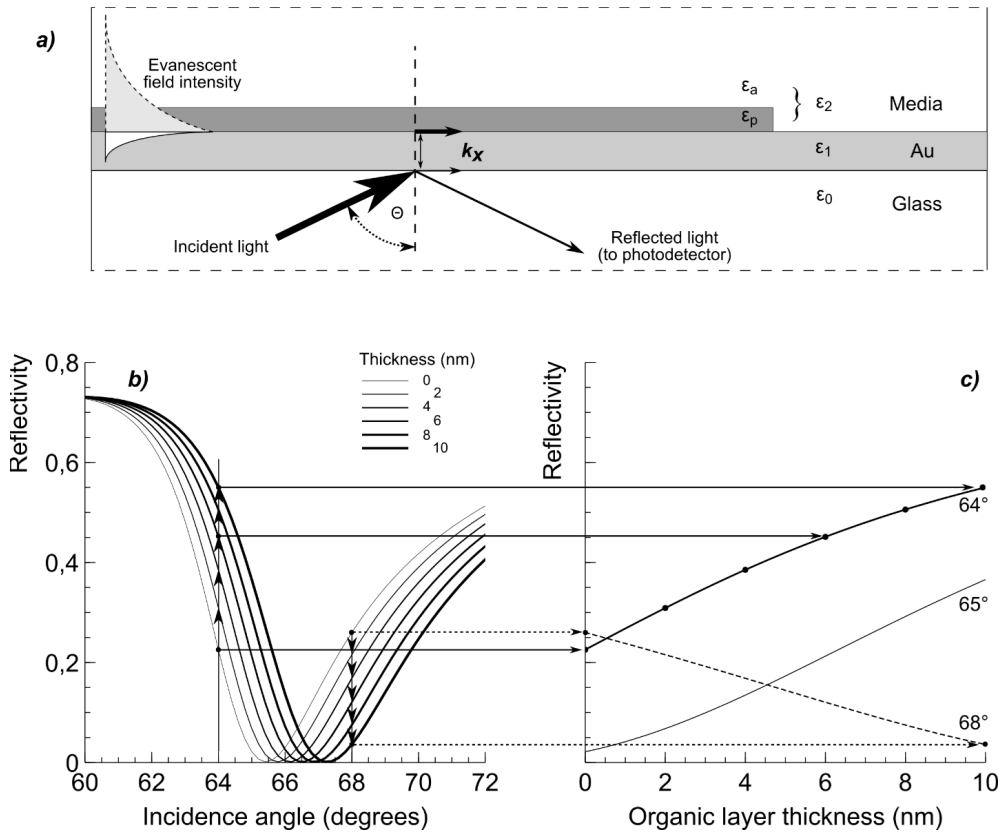

FIGURE 2.1: Kretschmann configuration for SPR measurement (a), SPR curves calculated for different thickness of organic layer on the metallic surface (b) and corresponding reflectivity changes measured at fixed incidence angle (64, 65 or 68 °). Parameters for the calculation: metallic layer consists from 2 nm Cr and 50 nm Au layer (refractive indices: Cr: 3.105 + 3.327i, Au: 0.168 + 3.138i); glass (refractive index 1.615); wavelength: 650 nm; organic layer: refractive index 1.49; thickness of the organic layer: 0, 2, 4, 6, 8 or 10 nm. The organic layer is contacting with water at 22 °C (refractive index 1.3317).

the sensing channel, possible changes of the volume refractive index [7, 8] can be compensated. The overall efficacy of such spatial referencing is increased by scaling down mean distance between the sensing and referencing spots into microscopic range while maintaining macroscopic value of total area of the sensing and referencing spots; this approach named as distributed referencing was suggested in [9]. The idea of having separate reference and sensing area in the same flow cell was extended in to an array of microfludic cells [10]. Separate measurements of SPR phase shifts in the referencing and sensing spots can be used for self-referencing as well [11]. A diffraction grating formed by the sensing and referencing strip shaped spots were used for inherent self-referencing [12]. Also other realizations of self-referencing SPR transducing based on the patterning of sensing and referencing spots were suggested. In [13–15] the reference channel was implemented using a 12-18 nm thick dielectric (Ta_2O_5) layer. Alternatively, a 35 nm thick plasma polymerized hexamethyldisiloxane layer was used [16]. Two distinct spectral bands, associated with SPR in the sensing and referencing spots, were measured by spectrophotometer and quantified simultaneously.

The spectral readout is poor compatible with SPR imaging mode which is of high importance for sensor arrays and high-throughput techniques. This was a motivation for the development of self-referencing techniques based on SPR imaging at single wavelength. In [17] two kinds of multilayer spots were used in pairs: differing by Ti sublayer of either 4 or 12 nm, on the top of which a 200 nm aluminum oxide layer and a 40 nm gold layer were deposited. SPR response in each pair of these elements showed an increased SPR sensitivity. In [18, 19] a microwell array in the gold layer or in the glass substrate was described, bottom of wells and their surroundings serve as sensing or referencing areas.

Spatial separation of sensing and referencing spots results in a loss of precious sensor surface. Another frequent drawback is a requirement of these technique for a pre- or post-determination of the positions of sensing and referencing spots. This was a motivation for the development of other self-referencing techniques which discriminate signals from surface and volume effects using the same sensor surface. These methods are based on strong dependence of penetration depth of evanescent wave on the surface plasmons mode [20, 21] or wavelength [22–26]. To satisfy the conditions for simultaneous excitation of surface plasmons and long-range plasmons with much higher penetration depth, a dielectric layer between coupling prism and metallic layer should be deposited. In [26] simultaneous excitation of surface plasmons at two wavelengths with a three times difference in penetration depth were used to suppress variations of the bulk refractive index.

Here we describe a novel method of self-referencing in SPR biosensors, which is based on integral measurement of light intensity reflected by microstructured surface whereas incidence angle is chosen close to its SPR minimum. An important advantage of this technique is a possibility to implement it into the most existing SPR devices without any modification of hardware.

2.1.3 Principle of the measurement technology

Let us consider the parts of the resonance curves, corresponding to the 2 nm and 6 nm thick organic layer (Fig. 2.1b), for better visualization these parts are presented magnified in the Fig. 2.2b. Assume that the 2 nm thick layer represents the referencing area (for example, a self-assembled monolayer with minimized adsorption of analyte and other compounds contained in the analyte solution) while the 6 nm layer represents the sensing area (for example, a self-assembled monolayer with immobilized antibodies for selective binding of the analyte). Here we suppose that the inherent thickness of the receptors layer is about 4 nm, which is a typical protein size. Assume that SPR signal is being measured (integrated) over some area which contains both sensing and referencing areas in approximately 50/50 ratio (Fig. 2.2a). The pattern structure is not important and can be arbitrary, but the minimal feature size of the pattern should be larger than the propagation length of plasmons. In such conditions the total SPR response can be represented as a sum of separate SPR responses from both sensing

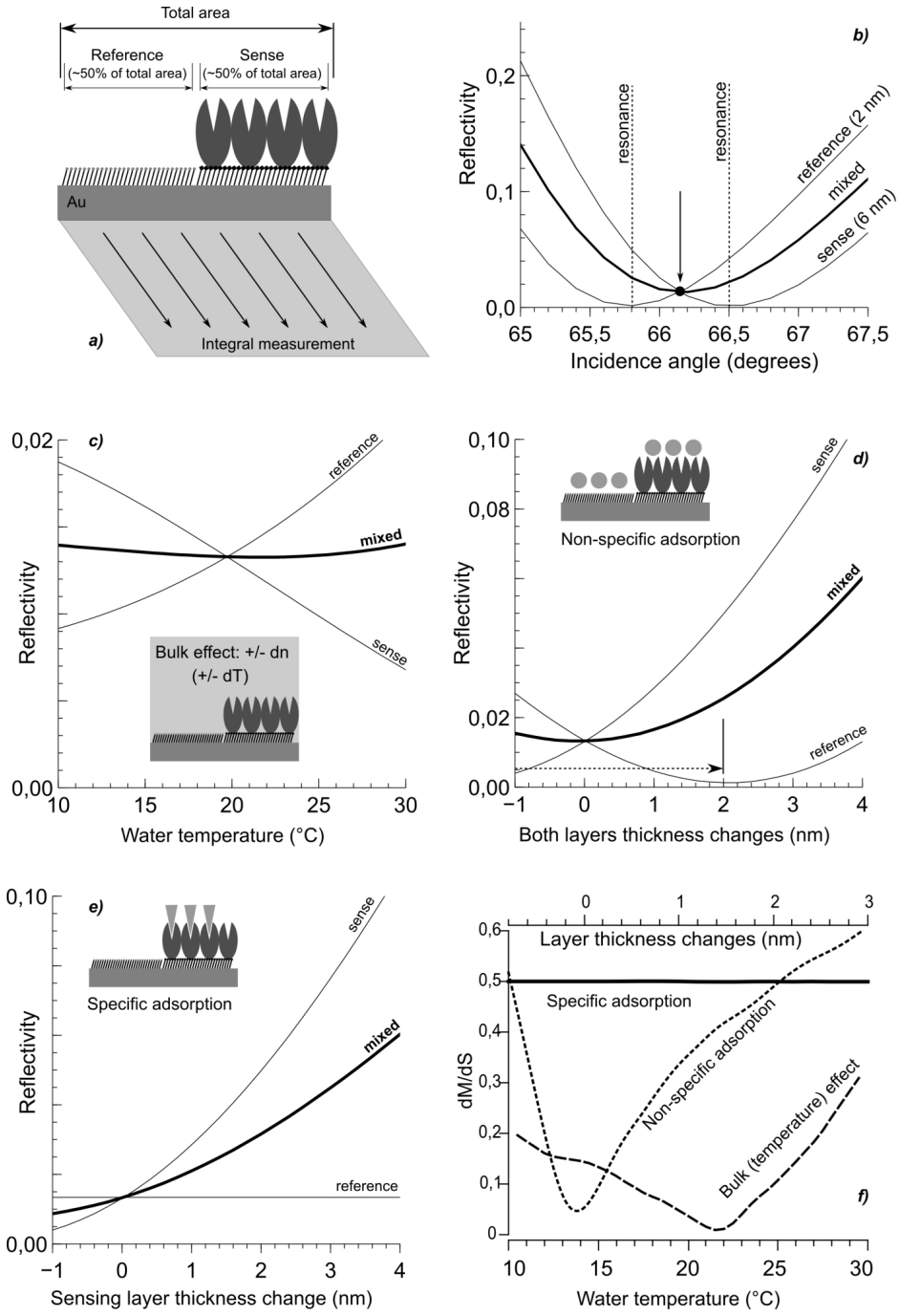

FIGURE 2.2: Principle of the new measurement technology and numerical analysis. Calculated SPR signals for the mixed surface with arbitrary pattern including 50 % of sensing area and 50 % of referencing area (a) are shown in the panel (b) for separated referencing and sensing areas as well as for their mixture. Temperature variation leads to the signals at both sensing and referencing spots but its influence is essentially compensated when detected integrally at the mixed area (c). SPR signal corresponding to non-specific adsorption is also suppressed manifold (d) while the signal corresponding to specific adsorption is only twice attenuated (e). A quantitative efficiency of self-referencing is indicated in (f), dM/dS indicates the ratio of integral signal change in the mixed area to the signal change in the sensing area. The parameters are described in the Fig. 2.1 and in the text.

and referencing areas. The surface with a feature size of the pattern below 100 nm exhibits SPR behavior typical for homogenous layers, the surface with a features sizes the pattern of more than 10 μm exhibits purely bimodal SPR behavior, the intermediately sized patterns exhibit the mixture of mono- and bi-modal SPR responses [27]. Therefore, the integral SPR curve is the weighted arithmetic mean of the SPR curves of the respective sensing and referencing areas where the weights are defined by surfaces of these areas. The minimum of the integral SPR is placed between their minima (denoted by arrow on the Fig. 2.2b). It is to note that in this point, where the integral SPR curve exhibits minimum, both SPR curves corresponding to sensing and referencing spots are actually not in their minima and therefore have notable SPR response to the changes of the effective refractive index. However, as noted above (see Fig. 2.2c), their responses to the same change have opposite polarity, therefore the changes affecting both curves simultaneously in the same way are mutually compensated. The difference in the slope of these curves can be compensated by corresponding adjustment of the ratio of surfaces of sensing and referencing areas so that the products of slope and occupied surface for the sensing and referencing areas have equal absolute values but opposite signs. This can be also reached by adjustment of slopes by slightly shifting the incidence angle from the total minimum. In Fig. 2.2c we show the calculated responses of the referencing and sensing areas to the changes of the bulk refractive index of aqueous solution for 1700 μRIU, this corresponds to the changes of temperature of this solution from 10 °C till 30 °C [6]. The integral signal shows an effective suppression of these signal changes. Similar signal suppression is observed if the thicknesses of the both areas are simultaneously changed for the same value (for example, due to unspecific adsorption). The suppression range is limited by approximately a half of the difference of thicknesses of sensing and referencing areas (Fig. 2.2d–f) because in order to maintain the opposing polarities of SPR signals of sensing and referencing areas and their mutual compensation, the incidence angle must remain between resonance angles corresponding to these areas. An application of this technique for compensation of non-specific requires that this adsorption has a quantitatively similar value for sensing and referencing areas; this may need an investigation and optimization of this process for each particular case [28–30] and is out of the scope of this work focused on the aspects of measurement technology. If the thickness of only sensing area is changed, no compensation occurs and a clear sensor response is observed (Fig. 2.2e). About two times attenuation of the total response due to the fact that only a part of the surface is used can be easily overcome by corresponding increase in signal amplification or incident light intensity. Fig. 2.2f demonstrates that an over 10 times suppression of bulk effects and non-specific adsorption can be achieved. The core idea of the new self-referencing technique includes such a patterning of the surface that approximately a half of it serves as a sensing area and has a different thickness compared to the rest (referencing) area. Notably, the arbitrary pattern of the surface

functionalization can be chosen, a presence of any regular structures or their determined positioning is not required. The measurement is performed over the whole area without separating sensing and referencing areas at the incidence angle close to the observed resonance angle. Further we present an experimental validation of this new approach.

2.1.4 Materials and Methods

2.1.4.1 Materials

16-Mercaptohexadecanoic acid, 11-mercaptoundecanol, EDC (1-ethyl-3-(3- dimethylaminopropyl)-carbodiimide), N-hydroxysuccinimide (NHS), human serum albumin (HSA), rabbit antibodies (whole serum) to HSA and glycine were from Sigma-Aldrich. Phosphate and ethanol (99.9 %) were from Merck, other chemicals from Roth. Deionized water additionally purified by ELGA-Classic was used for preparation of all working solutions. SPR slides consisting of glass (n=1.61) coated by 2 nm Cr and 50 nm Au were from Mivitec GmbH.

2.1.4.2 Surface functionalization

Prior to functionalization the SPR slides were cleaned by freshly prepared "piranha solution" (1:3 (v:v) mixture of H_2O_2/H_2SO_4), rinsed thoroughly with water, ethanol and dried at room temperature. *Caution: piranha solution reacts violently with most organic materials and must be handled with extreme care.* Various ω-functionalized alkylthiols were tested for preparation of patterned surfaces: OH-terminated alkylthiol (11-mercaptoundecanol, MU) or oligoethylene glycol -terminated alkylthiol (11-(mercapto-undecyl)tetra(ethylene glycol), MUTEG) for referencing area while 16-mercaptohexadecanoic acid (MHA) was used for coating of sensing area for subsequent covalent immobilization of HSA. The patterned surfaces were prepared in two steps. First, 5 mM dimethyl sulfoxide solution of MU or MUTEG was deposited by a non-contact dispenser sci-FLEXARRAYER-S3 covering about 40% of the total gold surface with an array of spots of about 150–250 μm diameter (Fig. 2.3). After 10 min incubation at room temperature in DMSO atmosphere the slide was rinsed three times with ethanol and incubated for 5 min in 1 mM MHA solution in ethanol; this leads to the coating of the rest gold area with MHA. Then the slide was rinsed three times with ethanol and dried. The differential SPR imaging of the surfaces patterned by this way (Fig. 2.3b, on example of the surface patterned by COOH- and NH_2-terminated alkylthiols, the details will be published elsewhere) shows that during such a treatment there is no replacement of the formerly deposited self-assembled monolayer. As a result, the gold surface is coated by an array of spots from MU or MUTEG while the rest part of the surface is coated by MHA.

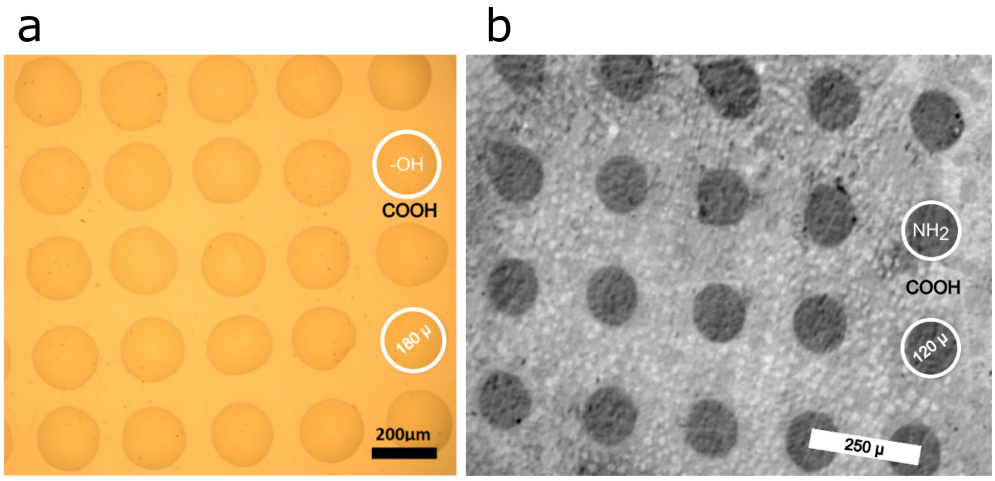

FIGURE 2.3: Illustration of patterned surfaces. a) Bright field microscopy of MU-containing DMSO droplets on the gold surface. The droplet diameter is about 200 μm, dot pitch is about 280 μm resulting in 40% surface coverage by the referencing area. b) An example of differential SPR imaging of the patterned surface containing ω-functionalized alkylthiols with amino- and carboxygroups (was not used for self-referencing).

2.1.4.3 SPR measurements

The sample solution was driven by peristaltic pump VICI Cheminert 08Y-0135L at flow rate of 180 μl/min. Sensor calibration was performed using two buffer solutions with known difference of their refraction indices: 12 mM phosphate buffer (pH 7.4) containing 140 mM NaCl and 12 mM phosphate buffer (pH 7.4) containing 240 mM NaCl. The covalent coupling of HSA to the carboxy-groups of MHA was performed by two different techniques: (i) as a one-pot reaction by addition of a 140 mM NaCl solution containing 2 mg/ml HSA and 10 mg/ml EDC or (ii) by activation of surface COOH-groups using addition of EDC/NHS (52.4 mM / 13.1 mM) solution in 100 mM MES at pH 5 an subsequent addition of 2 mg/ml HSA in the buffer solution consisting of 12 mM phosphate and 140mM NaCl (pH 7.4). Signal saturation during the first 20 min of immobilization and a short lifetime of activated groups [31, 32] allows to suggest that most of these group were inactivated during immobilization and subsequent 1-h washing with PBS. Removal of the bond antibodies was performed by treatment with aqueous solution of 10mM glycine containing 10 mM NaCl (pH 2).

Most SPR measurements were performed using commercial SPR setup Biosuplar-421. The beam in this device (and correspondingly the integration area for the measurements) has an elliptical shape of $\sim 4 \times 2$mm. Differential SPR imaging was performed using a homemade setup for SPR microscopy. All measurements were repeated at least three times. Numerical simulation was performed using transfer-matrix method and optical parameters as described in [26].

2.1.5 Results and discussion

The idea of self-referencing SPR-sensor with compensation of the bulk effect using micro-patterned surface with integral measurement of the reflected light was validated on an example of MU or MUTEG coated referencing area and MHA coated surface with immobilized HSA as sensing area (Fig. 2.3a). Thus, the refractive changes due to the specific binding of analyte (anti-HSA) might occur only in the functionalized area. Binding was measured on patterned SPR slides at incidence angles near the point of the steepest slope of the SPR curve and at the minimum of SPR curve from the whole surface.

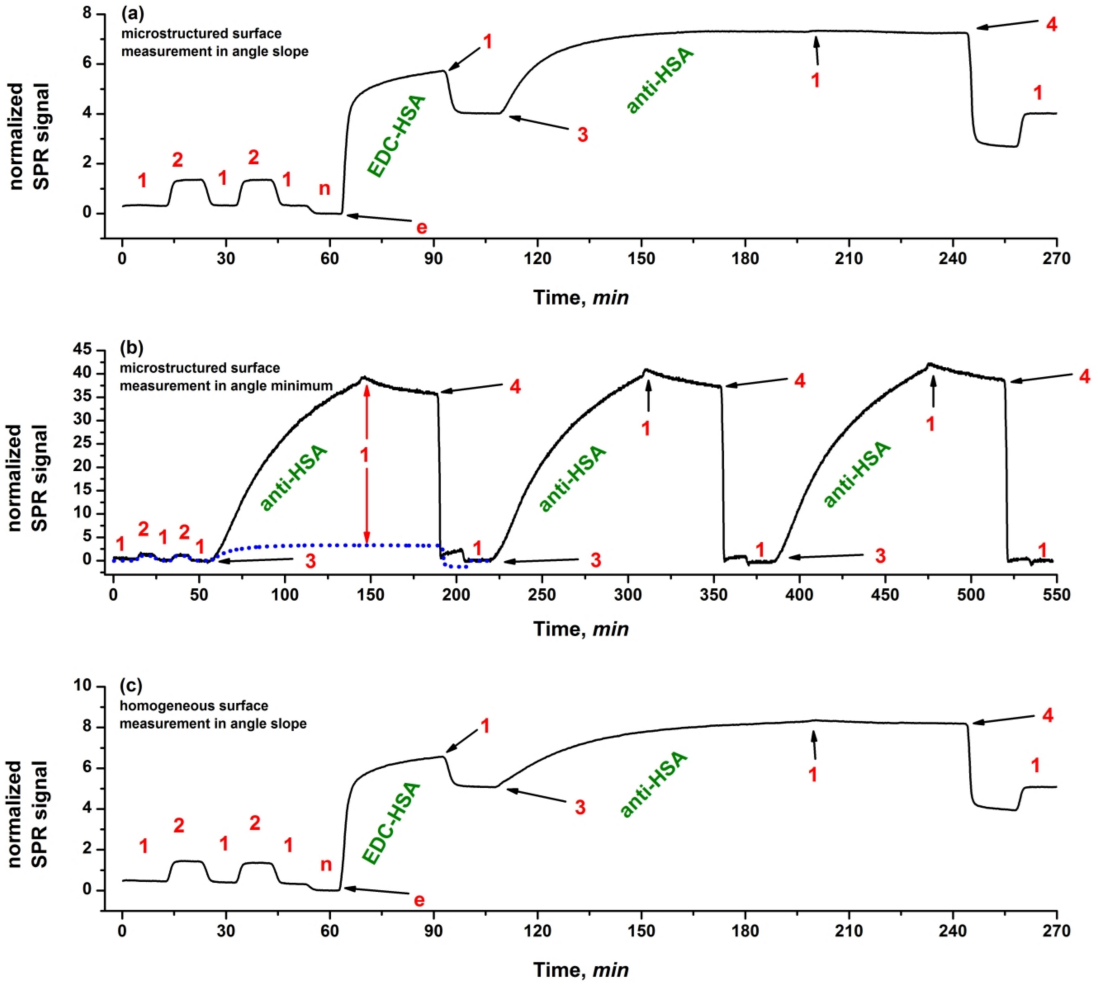

FIGURE 2.4: SPR responses measured on patterned surface containing 40 % coverage by MU and 60 % coverage by MHA (a, b) and on homogeneous surface coated by MHA (c) at the angle of the maximal slope (a, c) and at the resonance angle (b). The panel (a) corresponds to the first part of the experiment while the panel (b) demonstrates the second part of the same experiment. Additions: (1) 12 mM PBS, 140 mM NaCl, pH 7.4; (2) 12 mM PBS, 240 mM NaCl, pH 7.4; (n) 140 mM NaCl; (e) 2mg/ml HSA, 10 mg/ml EDC in 140 mM NaCl; (3) 8 μg/ml anti-HSA, 12 mM PBS, 140 mM NaCl, pH 7.4; (4) 10 mM NaCl, 10 mM glycine, pH 2. The dashed line in the panel (b) shows the anti-HSA binding response from the panel (a) normalized to the magnitude of the response to the pulse of salt concentration (additions 1, 2).

The results of the SPR measurements are shown in Fig. 2.4. We compare our approach with the conventional one in terms of the ratio of SPR responses to the defined changes of the bulk refractive index induced by salt concentration pulse to the defined surface effect caused by binding of antibodies to the immobilized receptor (panels a, b). For comparison, the same experiment on not-structured surface was performed (panel c). First, an effect of known salt concentration pulses on SPR response was measured (Fig. 2.4, a or c, alternating additions 1 and 2). Then the covalent HSA immobilization to the sensing area coated by MHA was performed (Fig. 2.4, addition e). In the next step the binding of anti-HSA to the immobilized HSA was registered (addition 3). Then the bond anti-HSA was removed by acidic buffer (addition 4).

These measurements were performed at the incidence angle corresponding to the maximum slope of SPR curve, then the incidence angle was set to the observed SPR minimum. The same salt concentration pulses were applied (Fig. 2.4b, alternating additions 1 and 2) and three cycles of anti-HSA binding (additions 3) with subsequent regeneration by acidic buffer (addition 4) were performed. For direct comparison the curve from the Fig. 2.4a, addition 3 was normalized to the calibration signal and plotted (dashed line) side-to-side in the first cycle in the Fig. 2.4b. In comparison to the measurement at the angle of the highest slope (Fig. 2.4a, addition 3), the measurement in the minimum (Fig. 2.4b) demonstrates an essential increase of the ratio of the signal magnitude during anti-HSA binding to the signal magnitude during the salt concentration pulses. Over 10-times suppression of the bulk effect was achieved thus validating the idea of the self-referencing SPR sensor.

Similar measurements were also performed for different ratio of sensing and referencing areas and for different functionalization of the referencing area. In all cases an application of the suggested methodology offered manifold suppression of SPR response caused by changes of the bulk refractive index.

2.1.6 Conclusion

A new method for the self-referencing SPR sensor is suggested. It is based on the integral measurement of the light reflected from a microstructured surface containing a mix of sensing and referencing spots, therefore no separate measurement channel is required for the referencing. The approach is compatible with many existing instruments and does not need any changes in the measurement setups.

An implementation of the new approach requires a patterning of the receptor surface. It can be performed by different techniques, for example by using of different spotters (like we did), photolitography, microcontact printing or by using of microfluidic approach. In the preliminary experiments the technique was tested using microcontact chemical printing based on the combination of microcontact printing and chemical immobilization (manuscript in preparation). There is no special requirements for the patern geometry, but the feature size of the pattern in the direction of plasmon propagation has to be larger than the plasmon propagation length. The sensing and

referencing areas should have a different optical thicknesses resulting in the partial separation of their resonance curves. Application of a thicker layer for sensing area is preferable, but the opposite case is also possible. The optimal incidence angle should be adjusted depending on the surface coverage by sensing area, which can be in the range of 40-75 %. The goal of the current work is the proof of principle, therefore we only relied on the thickness difference obtained by immobilization of the protein receptor layer itself. This led to over ten times suppression of the effect of the bulk refractive index. It follows from the geometrical consideration of the compensation principle (Fig. 2.2b) that optimal suppression (maximal ratio of the sensor responses to the changes of the refractive index near resonant surface and in the bulk phase) could be obtained when the measurement angle corresponds to the maximal slope of the resonance curves for sensing and referencing areas. This requires about 10–20 nm difference in the thickness of sensing and referencing areas (Fig. 2.5a). The larger separation of these curves also increases the suppression range. The mechanism of the self-referencing approach was explained for the case of fixed wavelength when incidence angle is selected from resonance conditions (Fig. 2.5a). But the same principle can be analyzed by fixing of the incidence angle and choosing optimal wavelength (Fig. 2.5b). It is to note that measurement of complete spectra is not required, therefore both approaches are equivalent.

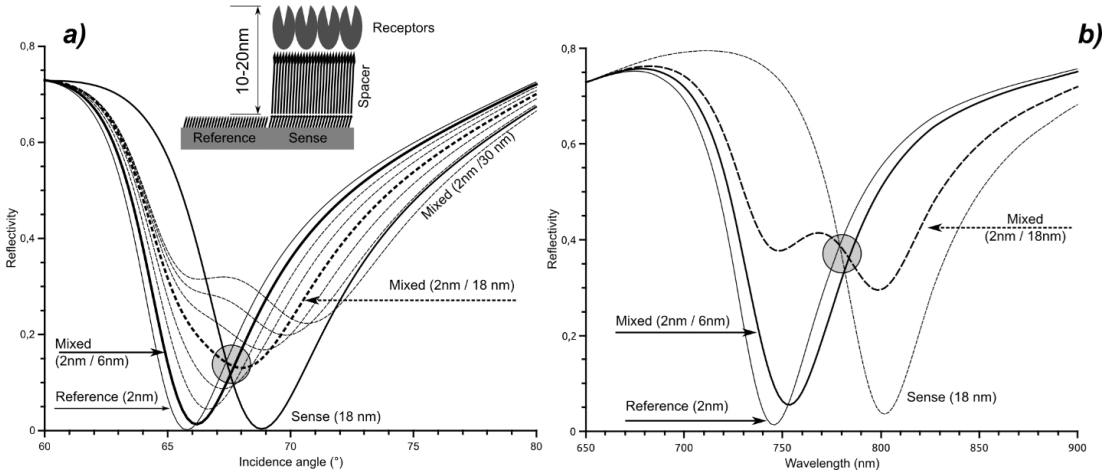

FIGURE 2.5: An increase of the height difference between sensing and referencing areas from 4 nm up to 30 nm leads to the better suppression (a). The method can be also realized in spectral domain (b): the incidence angle here is set to 62 degrees, the optimal measurement wavelength is then around 770 nm. The cross of the SPR curves for sensing and referencing area, where optimal conditions for method are expected, are denoted by grey circles.

Acknowledgement

Authors are grateful to Dr. K. Tonder and F. Klemm for the general assistance and discussions. A development of technology for the preparation of patterned surfaces was supported by EC Project "Nanodetector" (FP7-NMP-2011-SME-5, #280478).

References

[1] B. Liedberg, C. Nylander, and I. Lunström, "Surface plasmon resonance for gas detection and biosensing," *Sens. Actuator.*, vol. 4, no. C, pp. 299–304, 1983.

[2] J. Homola, *Surface Plasmon Resonance Based Sensors*. Springer, 2006.

[3] S. Scarano, M. Mascini, A. P. F. Turner, and M. Minunni, "Surface plasmon resonance imaging for affinity-based biosensors.," *Biosens. Bioelectron.*, vol. 25, no. 5, pp. 957–966, 2010.

[4] A. Zybin, D. Boecker, V. M. Mirsky, and K. Niemax, "Enhancement of the detection power of surface plasmon resonance measurements by optimization of the reflection angle," *Anal. Chem.*, vol. 79, no. 11, pp. 4233–4236, 2007.

[5] L. S. Jung, C. T. Campbell, T. M. Chinowsky, M. N. Mar, and S. S. Yee, "Quantitative interpretation of the response of surface plasmon resonance sensors to adsorbed films," *Langmuir*, vol. 14, no. 19, pp. 5636–5648, 1998.

[6] A. H. Harvey, J. S. Gallagher, and J. M. H. L. Sengers, "Revised Formulation for the Refractive Index of Water and Steam as a Function of Wavelength, Temperature and Density," *J. Phys. Chem. Ref. Data*, vol. 27, pp. 761–774, jul 1998.

[7] G. B. Sigal, M. Mrksich, and G. M. Whitesides, "Using surface plasmon resonance spectroscopy to measure the association of detergents with self-assembled monolayers of hexadecanethiolate on gold," *Langmuir*, vol. 13, no. 10, pp. 2749–2755, 1997.

[8] M. J. O'Brien II, S. Brueck, V. H. Perez-Luna, L. M. Tender, and G. P. Lopez, "SPR biosensors: simultaneously removing thermal and bulk-composition effects," *Biosens. Bioelectron.*, vol. 14, no. 2, pp. 145–154, 1999.

[9] D. Boecker, A. Zybin, K. Niemax, C. Grunwald, and V. M. Mirsky, "Noise reduction by multiple referencing in surface plasmon resonance imaging," *Rev. Sci. Instrum.*, vol. 79, no. 2, pp. 2–8, 2008.

[10] M. A. Eddings, J. W. Eckman, C. A. Arana, G. A. Papalia, J. E. Connolly, B. K. Gale, and D. G. Myszka, "'"Spot and hop": internal referencing for surface plasmon resonance imaging using a three-dimensional microfluidic flow cell array.," *Anal. Biochem.*, vol. 385, pp. 309–13, feb 2009.

[11] A. R. Halpern, Y. Chen, R. M. Corn, and D. Kim, "Surface plasmon resonance phase imaging," *Anal. Chem.*, vol. 83, no. 13, pp. 2801–2806, 2011.

[12] F. Yu, S. Tian, D. Yao, and W. Knoll, "Surface plasmon enhanced diffraction for label-free biosensing," *Anal. Chem.*, vol. 76, no. 13, pp. 3530–3535, 2004.

[13] J. Homola, H. B. Lu, G. G. Nenninger, J. Dostálek, and S. S. Yee, "A novel multichannel surface plasmon resonance biosensor," *Sensors Actuators B Chem.*, vol. 76, pp. 403–410, jun 2001.

[14] H. B. Lu, J. Homola, C. T. Campbell, G. G. Nenninger, S. S. Yee, and B. D. Ratner, "Protein contact printing for a surface plasmon resonance biosensor with on-chip referencing," *Sensors Actuators B Chem.*, vol. 74, pp. 91–99, apr 2001.

[15] C. Boozer, Q. Yu, S. Chen, C.-Y. Lee, J. Homola, S. S. Yee, and S. Jiang, "Surface functionalization for self-referencing surface plasmon resonance (SPR) biosensors by multi-step self-assembly," *Sensors Actuators B Chem.*, vol. 90, pp. 22–30, apr 2003.

[16] T. Akimoto, K. Ikebukuro, and I. Karube, "A surface plasmon resonance probe with a novel integrated reference sensor surface," *Biosens. Bioelectron.*, vol. 18, no. 12, pp. 1447–1453, 2003.

[17] M. Piliarik, H. Vaisocherová, and J. Homola, "Towards parallelized surface plasmon resonance sensor platform for sensitive detection of oligonucleotides," *Sensors Actuators B Chem.*, vol. 121, no. 1, pp. 187–193, 2007.

[18] A. Abbas, M. J. Linman, and Q. Cheng, "Patterned Resonance Plasmonic Microarrays for High-Performance SPR Imaging," *Anal. Chem.*, vol. 83, pp. 3147–3152, apr 2011.

[19] M. J. Linman, A. Abbas, C. C. Roberts, and Q. Cheng, "Etched Glass Microarrays with Differential Resonance for Enhanced Contrast and Sensitivity of Surface Plasmon Resonance Imaging Analysis," *Anal. Chem.*, vol. 83, pp. 5936–5943, aug 2011.

[20] R. Slavík, J. Homola, and H. Vaisocherová, "Advanced biosensing using simultaneous excitation of short and long range surface plasmons," *Meas. Sci. Technol.*, vol. 17, pp. 932–938, apr 2006.

[21] J. T. Hastings, J. Guo, P. D. Keathley, P. B. Kumaresh, Y. Wei, S. Law, and L. G. Bachas, "Optimal self-referenced sensing using long- and short- range surface plasmons.," *Opt. Express*, vol. 15, pp. 17661–17672, dec 2007.

[22] K. A. Peterlinz and R. Georgiadis, "In situ kinetics of self-assembly by surface plasmon resonance spectroscopy," *Langmuir*, vol. 12, no. 20, pp. 4731–4740, 1996.

[23] T. Zacher and E. Wischerhoff, "Real-time two-wavelength surface plasmon resonance as a tool for the vertical resolution of binding processes in biosensing hydrogels," *Langmuir*, vol. 18, no. 5, pp. 1748–1759, 2002.

[24] A. Zybin, C. Grunwald, V. M. Mirsky, J. Kuhlmann, O. S. Wolfbeis, and K. Niemax, "Double-wavelength technique for surface plasmon resonance

measurements: basic concept and applications for single sensors and two-dimensional sensor arrays.," *Anal. Chem.*, vol. 77, pp. 2393–2399, apr 2005.

[25] D. Boecker, A. Zybin, V. Horvatic, C. Grunwald, and K. Niemax, "Differential surface plasmon resonance imaging for high-throughput bioanalyses," *Anal. Chem.*, vol. 79, no. 2, pp. 702–709, 2007.

[26] S. Nizamov and V. M. Mirsky, "Self-referencing SPR-biosensors based on penetration difference of evanescent waves.," *Biosens. Bioelectron.*, vol. 28, pp. 263–269, oct 2011.

[27] A. Dhawan, M. Canva, and T. Vo-dinh, "Bimodal behavior and isobestic transition pathway in surface plasmon resonance sensing," vol. 20, no. 21, pp. 106–111, 2012.

[28] G. Lautner, Z. Balogh, V. Bardoczy, T. Meszaros, and R. E. Gyurcsanyi, "Aptamer-based biochips for label-free detection of plant virus coat proteins by SPR imaging," *Analyst*, vol. 135, no. 5, pp. 918–926, 2010.

[29] P. Cígler, V. Král, M. Kožíšek, J. Konvalinka, and V. M. Mirsky, "Anomalous adsorptive properties of HIV protease: Indication of two-dimensional crystallization?," *Colloids Surfaces B Biointerfaces*, vol. 64, no. 1, pp. 145–149, 2008.

[30] K. Nakanishi, T. Sakiyama, and K. Imamura, "On the adsorption of proteins on solid surfaces, a common but very complicated phenomenon," *J. Biosci. Bioeng.*, vol. 91, no. 3, pp. 233–244, 2001.

[31] J. Lahiri, L. Isaacs, J. Tien, and G. M. Whitesides, "A Strategy for the Generation of Surfaces Presenting Ligands for Studies of Binding Based on an Active Ester as a Common Reactive Intermediate:A Surface Plasmon Resonance Study," *Anal. Chem.*, vol. 71, pp. 777–790, feb 1999.

[32] N. Wrobel, M. Schinkinger, and V. M. Mirsky, "A novel ultraviolet assay for testing side reactions of carbodiimides.," *Anal. Biochem.*, vol. 305, no. 2, pp. 135–138, 2002.

2.2 Ionic referencing in surface plasmon microscopy: visualization of the difference in surface properties of patterned monomolecular layers

NIZAMOV, S., SCHERBAHN, V., & MIRSKY, V. M.

Published in: Analytical Chemistry, 89(7), 3873–3878. (2017)
DOI:10.1021/acs.analchem.7b00251

2.2.1 Abstract

An approach for visualization of patterned monomolecular layers in surface plasmon microscopy (SPM) is suggested. The development of hidden image in SPM is achieved by referencing of images obtained in the presence of electrolytes with a high molar refraction of either anions or cations. A formation of diffuse layer near the charged surface areas leads to the redistribution of ions. The ratio of SPM images allows one to visualize this redistribution and to distinguish surface areas with different properties. The approach is unobtrusive and robust; it can be used with most surface plasmon resonance (SPR) imaging instruments.

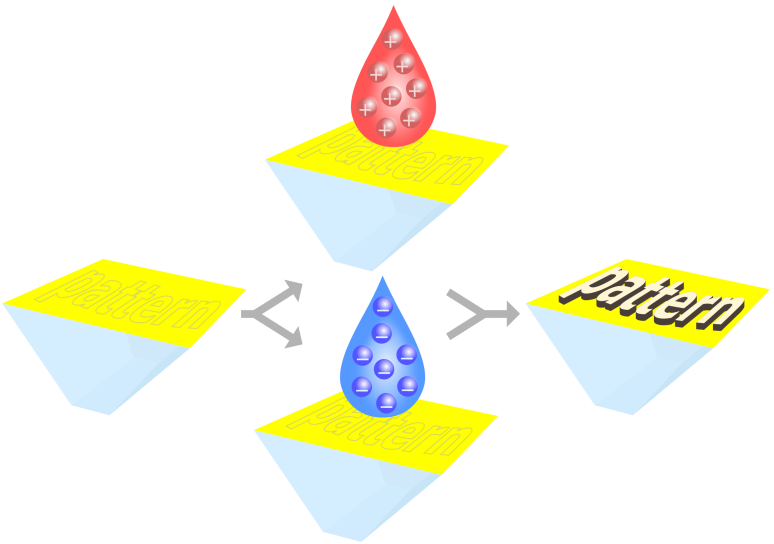

FIGURE 2.6: Graphical abstract

2.2.2 Introduction

SPR sensors are based on the detection of changes of the reflected light due to the change of the refractive index in close vicinity to the metallic sensor surface [1]. The

sensor surface can be coated by receptors to make the response specific to particular analytes. To alleviate a contribution of unspecific binding and possible effect of fluctuations of temperature, light intensity, etc., different types of referencing were suggested [2–4]. An implementation of referencing channels into SPR technique can be easily done by using of SPR in imaging format (surface plasmon microscopy, SPM[1] [5]). This approach provides also such additional features as an increase of sensitivity using chemometric techniques or an increase of throughput due to measurement of many sensing spots simultaneously.

Immobilization of receptor on the metallic sensor surface (usually gold or silver are used) is often performed through deposition of self-assembled monolayers of thiolated compound with functional groups further used for conjugation with different receptors (antibodies, antigens, DNA, aptamers, etc.) [6]. A formation of the patterned sensor surface can be performed at the level of self-assembled monolayers. However, the signal difference between differently coated spots in pattern can be so small that their recognition by SPM is not reliable. The SPM signal due to variation of the incidence angle for 0.1° or of the thickness of the metallic layer for 0.5 nm is comparable with the effect of 1 nm of organic adsorbate (Fig. 2.13, Supplementary). Thus, the effect of the small changes in the thicknesses of the adsorbate layer on the gold surface can be easily overwhelmed by the inhomogeneity of the glass substrate, gold layer, illumination, impurities and other factors that influence the resonance conditions. Therefore, the determination of the position of sensing and referencing spots, which is required for many applications of sensor arrays and/or referencing techniques [2], may be problematic in case of the small difference in their optical properties. Since the formation and application of sensor arrays is usually done separately (using different techniques and instruments), one has to rely on spatial reproducibility of the array formation and its alignment within the instruments. This complicates the development, investigation and quality control of the sensor array.

We propose here an effective and reliable approach for visualization of spots with different surface properties independent of their thickness and optical properties. The approach is easily and unobtrusively applicable in each SPR imaging system. It is based on the fact that the distribution of ions near sensor surface is determined by their interaction with the surface (Fig. 2.7). Applying the electrolyte solutions with very different contribution of anions and cations into the total refractive index of solutions, the difference in surface properties over the whole sensor area is visualized.

2.2.3 Principle

SPR sensors measure the changes in the refractive index (RI) near a metallic surface within the penetration of evanescent wave [1, 7]. To account for inhomogeneous distribution of RI within the penetration volume, the concept of the effective refractive

[1] also denoted as (wide-field) surface plasmon resonance microscopy, (WF)-SPRM

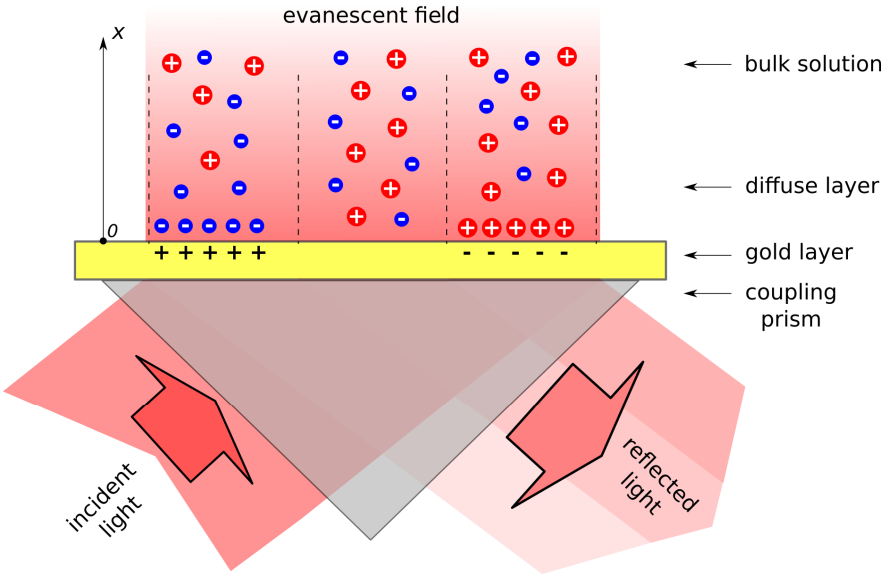

FIGURE 2.7: SPR response is influenced by redistribution of ions near charged surface. Notably, the thickness of the diffuse layer at concentrations above 10 μM is less than the penetration depth of the evanescent wave.

index for SPR was suggested [8]:

$$n_{eff} = \frac{2}{I_p} \int_0^\infty n(x) * e^{\frac{-2x}{I_p}} dx \tag{2.3}$$

where n_{eff} is the effective RI of the media, in which the RI distribution has the shape of $n(x)$, and x axis is normal to the sensor surface. I_p defines the penetration depth of the evanescent wave whose intensity decays exponentially with $(-x/I_p)$ factor with the distance from the surface x (Fig. 2.7). For the typical SPR setup (630–650 nm wavelength, 45–50 nm thick gold sensor layer, and the aqueous solutions with $n \sim 1.33$), I_p is ~ 170–190 nm [3].

On the other side, the RI profile near the sensor surface is determined by the concentration profile of ions near it. According to the Boltzmann distribution used in the Gouy-Chapman model, the concentration profile of ionic species of the 1:1 electrolyte near a charged surface depends on the electrical potential φ and the molar bulk volume concentration c:

$$c_+(x) = ce^{-\frac{e\varphi}{kT}}, \quad c_-(x) = ce^{+\frac{e\varphi}{kT}} \tag{2.4}$$

where e is the elementary charge, k is the Bolzmann constant, and T is the absolute temperature. According to Gouy-Chapman theory, the electrical potential decays exponentially:

$$\varphi = \varphi_0 e^{-\kappa x} \tag{2.5}$$

where φ_0 is the surface potential and κ^{-1} is the Debye length. At 25 °C the Debye length (in nanometers) for 1:1 electrolyte of concentration c is:

$$\kappa^{-1} = \frac{0.33}{\sqrt{c}}. \tag{2.6}$$

In absolutely pure water at pH = 7, $\kappa^{-1} \sim 1$ μm, but already at concentration of 1mM of 1:1 electrolyte it drops to just 9.6 nm. Thus, at c > 1 mM the concentration profile of ions near the charged surface $c_+(x)$, $c_-(x)$ asymptotically reaches the bulk concentration c at distances much less than the penetration depth: $\kappa^{-1} << I_p$ (Fig. 2.8). This leads to the deviation of the effective RI from the bulk RI for the effect caused by redistribution of ions near charged surface (Fig. 2.8): an excess of the counter-ions and a depletion of the co-ions in this region (see Fig. 2.7). It is to note, however, that different ions having nominally the same absolute charge are not optically equivalent and possess different molar refraction. Molar refraction of anions and cations in solutions are not measurable separately, only the total RIs for neutral compounds are available. An estimation of the partial ionic contributions can be done by comparison of RIs of homologous salt solutions (Table 2.1, ordered by valence and mass of ions).

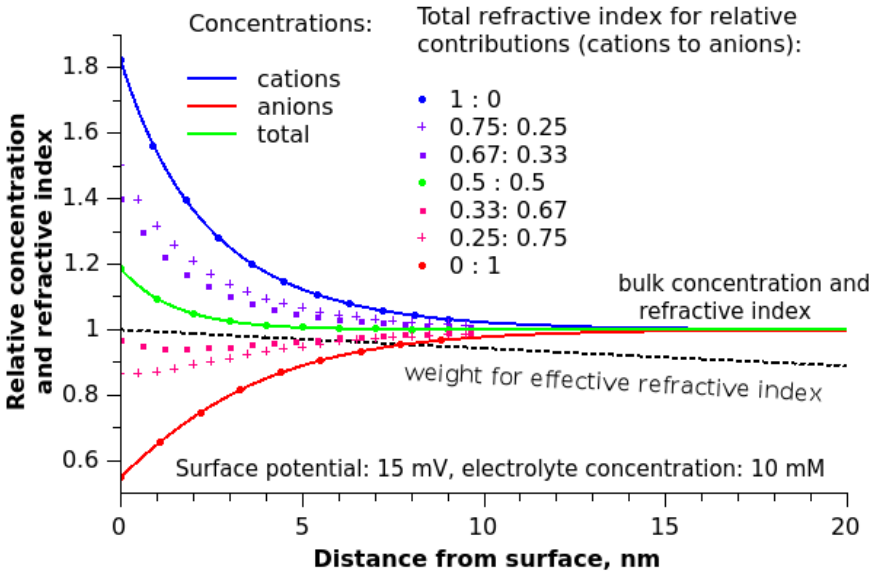

FIGURE 2.8: The concentration profile of ions and the resulting refractive index profile for different relative ionic contributions, normalized to their values in bulk solution. Hypothetical 1:1 electrolytes with different relative contributions of anions and cations (from 1:0 to 0:1) into total refractive index were considered).

For the salts which are "homologous" to NaCl (all sodium salts and all chlorides, Tab. 2.1) an influence of the anions is much higher than that of the cations. The molar refraction of anions increases with the increase of their atomic mass: F^- < Cl^- < Br^- < I^- series. Whereas only a slight increase of the impact of cations is observed from Li^+ to Cs^+ and from Mg^{2+} to Ba^{2+} (note that at the same molar concentration, the real

amount of chloride ions doubles for bivalent cations). These can be explained by the increase of molar refraction of monoatomic ions with the amount of electrons on the external shell and its distance to the nuclei (or, with polarizability which is directly connected to refractivity [9]).

The separation of the total refractive index into the sum of ionic refractions is just an approximation [9]. Nevertheless, this model [9] and literature data [10] suggest that by choosing of the right compound, one can achieve that SPR response to electrolyte solution is predominated by either anions or cations (Fig. 2.8).

TABLE 2.1: Molar refractive indices of diluted aqueous electrolytes. Units: 10^{-6} RIU/mM. The data for compounds were recalculated from [10] for ~ 500 mM solutions, 20°C and 589 nm (except marked with * which are from the suppliers). The data for ions are from [9].

	Anions	OH^-	F^-	Cl^-	CH_3COO^-	NO_3^-	Br^-	I^-
Cations		4.7	2.2	8.6	13.9	10.4	12.2	19.0
H^+	-0.3			8.3	4.4	7.9		
Li^+	0.1			9.0				
NH_4	4.7	0.9		10.3				
Na^+	0.7	11.0	5.2*	10.1	11.3	9.3	14.1	
K^+	2.7	10.6	3.4*	9.8		9.2	13.9	21.5
Ag^+	5.1					17.7		
Cs^+	6.9			12.7				
Mg^{2+}	-0.7			23.3				
Ca^{2+}	1.6			25.8				
Sr^{2+}	2.7			27.4				
Ba^{2+}	5.2			30.0				

Therefore, for extraction of contribution of the double layer to the effective RI, we suggest to use a measurement of SPR response using electrolytes with a large disproportion in molar refraction of ions. In case of negatively charged surface the large excess of cations is expected and vice versa (Fig. 2.7). The amount of the counter-ions attracted to the charged surfaces is higher than the amount of the repelled co-ions (Fig. 2.8). This effect being enhanced by the choice of the type of counter ions possessing a higher molar refraction provides prevailing effect of the counter-ions on SPR signal. Such ionic referencing can be further amplified by subsequent application of two electrolytes providing higher contributions of anions (as counter ions for positively charged surface areas) and cations (as counter ions for negatively charged surface areas). The difference in SPR responses to these electrolytes is mainly defined by the distribution of surface charges through the sensor surface. In the current work we apply this principle for visualization of patterned monomolecular layers.

2.2.4 Experimental section

11-Mercaptoundecanoic acid (C10-COOH), 11-amino-1-undecanethiol hydrochloride, benzyltrimethylammonium chloride (BTMA), sodium citrate tribasic dehydrate, citric acid monohydrate, sodium chloride, sodium salycilate were purchased from Sigma Aldrich (www.sigmaaldrich.com). Di-sodium hydrogen phosphate, sodium dihydrogenphosphate monohydrate and boric acid were purchased from Merck (www.merck.com). 11-(Mercaptoundecyl)-trimethylammonium chloride (C11-$N^+(CH_3)_3Cl^-$) was purchased from ProChimia Surfaces (www.prochimia.com). Glycerol (> 99.5 %) was purchased from Roth (www.calrroth.com). 1 mM buffer solutions with pH 5 (citric acid / sodium citrate tribasic dehydrate), pH 7 (di-sodium hydrogen phosphate / sodium dihydrogenphosphate monohydrate), and pH 9 (boric acid) were used. The SPM was described elsewhere [11, 12]. Shortly, 642 nm SM-fiber coupled laser diode with current and temperature controllers (LP642-SF20, LDC205C and TED200C correspondingly) from Thorlabs (www.thorlabs.com) were used for illumination. The light was collimated and passed through Glan polarizer. Images acquired by MT9P031 mono-chrome CMOS image sensor, were analyzed by homemade software [12]. The sensors consist of ~ 45 nm gold layer on the SF-10 glass prisms (Phasis SARL, Switzerland). They were cleaned for 20 s by freshly prepared "piranha solution" (1:3 v:v mixture of 32% H_2O_2/H_2SO_4), rinsed thoroughly with water and ethanol, and dried at room temperature. *Caution: piranha solution reacts violently with most organic materials and must be handled with extreme care.* The surface patterning was performed in two steps [5, 11]. 10 mM of C11-$N^+(CH_3)_3$ Cl^- solution in DMSO were deposited by a non-contact dispenser to form an array of spots of about 100–250 μm diameter with a dot pitch of 200–300 μm. After 20-min-incubation in saturated DMSO vapor, the droplets on the gold surface were washed away and rinsed thoroughly by DMSO and by ethanol. The rest surface was functionalized by 10 min. incubation in 1 mM C10-COOH in ethanol. Finally, the prism was rinsed by ethanol, dried and mounted into the SPM device. The sample suspension was pumped by a solenoid-operated micropump (Biochem Valve, 130SP1220-1TP, 12V-DC, www.biochemfluidics.com) at a flow rate of 1 ml/min. 5–6 min washing with the background buffer was performed between injections of other solutions.

2.2.5 Results

The main intention of this work is to characterize unobtrusively the patterned functionalization of the gold surfaces. Such surfaces can be used for charge-selective adsorption and detection of nanoparticles [11, 12], for self-referencing SPR biosensors [4], for distributed referencing [2] or for SPR sensor arrays [13]. In [11], the gold surface was patterned by the array of spots, functionalized with one type of ω-terminated alkyl thiol (typically, $-NH_2$ or $-N(CH_3)_3{}^+$ terminated), whereas the rest was coated by

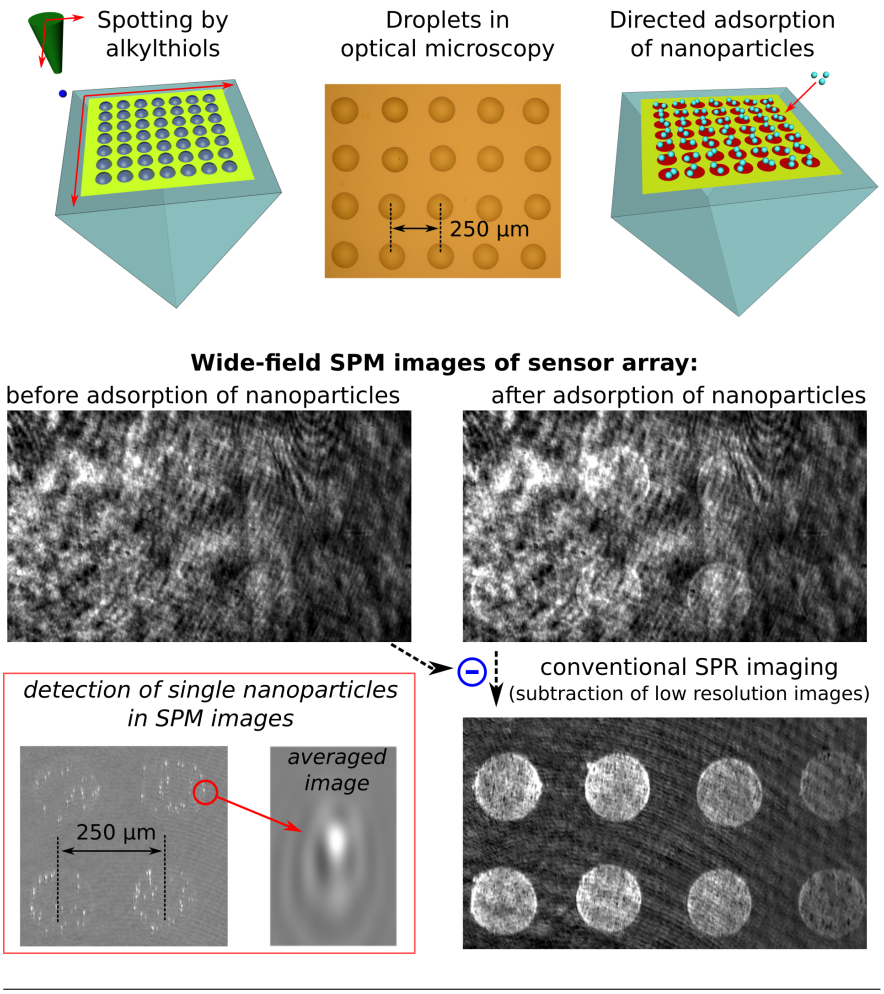

FIGURE 2.9: Deposition of the patterned monomolecular layer on the gold surface of SPR sensor and its application for directed adsorption of nanoparticles [11]. In the middle line SPM (at maximal contrast) of the patterned sensor surface before (left) and after (right) binding of negatively charged 40 nm gold nanoparticles. Patterning: 11-mercaptoundecyltrimethylammonium chloride (spots, $-N(CH_3)_3^+$), 11-mercaptoundecanoic acid (rest surface, –COOH). The spots become barely visible in raw SPM images after adsorption of nanoparticles. In the bottom line: the same measurement was proceeded by dynamic referencing (taking the ratio of two subsequent frames), allowing detection and imaging of single nanoparticles [11, 12] (middle, a magnified averaged image of single nanoparticles is shown left), and by static referencing (subtracting the single image chosen as a back-ground from each other one) as in conventional SPR imaging (right).

another alkyl thiol (–COOH terminated). A deposition of the patterned monomolecular layer on the gold surface of SPR sensor was performed using ink-jet spotting (Fig. 2.9). The spots were formed by droplets of the corresponding alkyl thiol solution in DMSO deposited as a grid array with a 200–300 μm pitch (image of these droplets on the gold surface, obtained by bright-field optical microscopy, is shown in the middle upper panel of Fig. 2.9). Then the sensor surface was rinsed (before complete evaporation of droplets), incubated in the solution of another alkyl thiol, rinsed again, dried and finally set into the SPM setup for imaging.

The influence of ω-terminating functional group on the effective RI is very small

(in comparison with variation of SPR conditions over the field of view); therefore, such patterned layers can hardly be visualized directly. The spots become visible upon adsorption of a large number of charged nanoparticles to the oppositely charged spots; this is especially evident after subtraction of the background (Fig. 2.9). Using wide-field SPM approach with differential image processing [12], one can detect even single nanoparticles during their adsorption [11]. This can be considered as a method for visualization of patterned monomolecular layers on its own. However, an adsorption of nanoparticles is influenced by a number of different factors [11]; this makes such visualization approach not reliable. Additionally, mainly irreversible adsorption of nanoparticles [14] makes such surfaces unsuitable for further applications.

To solve these problems, ionic referencing of surface properties was suggested. This approach relies on different concentration profiles of anions and cations near the charged surface and on disproportion in their contributions to the total RI.

The choice of inorganic ions with large molar refraction is quite broad for anions, but not for cations (Table 2.1). Organic ions provide much wider choice, and they are heavier; moreover, the compounds with aromatic moieties possess an easily polarizable π-electrons system. Therefore, for this work, four compounds with very different contribution of ions into the total RI of solutions were chosen (Table 2.1):

- glycerol (non-ionic)
- sodium chloride (low cationic and anionic contributions)
- sodium salicylate (low cationic and high anionic contributions)
- benzyltrimethylammonium chloride (high cationic and medium anionic contributions)

The use of glycerol as a non-ionic and low-adsorptive solute allows calibration of SPR response without effects of the surface properties. Then we used sodium chloride to get a base line to detect an influence of the replacement of its cation or anion by organic ones with much larger molar refraction. The even larger ratio of anionic to cationic molar refraction can be achieved using Li and F salts. After formation of patterned monomolecular layers on the sensor surface, it was imaged by SPM during sequentially flushing it with different electrolytes interleaved with buffer solutions (Fig. 2.10). The array consists of the spots of $-NH_2$ -terminated alkyl thiol with 250 μm pitch; the rest is coated with –COOH -terminated alkyl thiol. The response from the whole surface (mean image intensity) is shown by black line. pH influence was studied too (Fig. 2.13, Supplementary). The pH dependence for sodium chloride can be hardly recognized, whereas for the electrolytes with high anionic or cationic contributions it is noticeable.

Glycerol is a non-ionic compound; therefore, its concentration near the charged surface does not differ from bulk concentration. Correspondingly, the integral signals on Fig. 2.10 were normalized to the glycerol response.

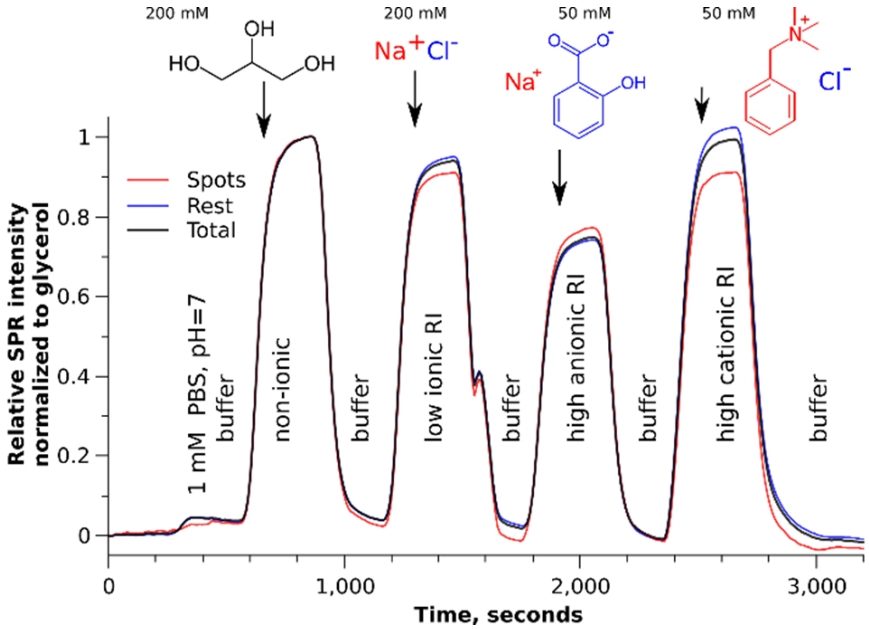

FIGURE 2.10: SPR responses to the sequence of solutions of 200 mM glycerol, 200 mM NaCl, 50 mM sodium salicylate, 50 mM benzyltrimethylammonium chloride. The responses are normalized to the effect of glycerol.

The raw SPM images of the same measurement are shown in Fig. 2.11. All images on Fig. 2.11 are gray scale intensity normalized: i.e., the mean value is subtracted, the intensities within the range [-3σ:+3σ] (σ – standard deviation) are scaled to the full possible image intensity scale. Thus the intensity normalization (or contrast stretching) emphasizes the image details and scales the image intensity to the optimal human perception. As it can be seen on Fig. 2.11 (upper line), no structure of the array is recognizable in raw SPM images. The main reason for this was described above: the difference in optical length of two functionalized coatings is too small to be seen on such field of view, especially, with not perfectly homogeneous surface. These inhomogeneities are overemphasized on Fig. 2.11 (upper line) due to contrast stretching. Since the sensor surface is patterned by alkyl thiols with $–NH_2$ and –COOH terminal groups, different surface areas possess opposite pH-dependent surface charge. This leads to different distribution of counter-ions in the diffuse layer. To reveal this difference raw SPM images for all solutions (including buffer) were mutually referenced to each other. For the referencing the pixel-to-pixel ratio of images [15] was taken. The histograms of ratio images were calculated after contrast stretching and presented in Fig. 2.11 as a matrix. Without loss of information, we can consider only a diagonal part of this matrix excluding diagonal elements as well.

The results were obtained for pH of solutions equal to 5, 7 and 9. In most cases the obtained histograms are similar to normal distribution and are only slightly pH dependent. But the referencing of the highly anionic RI solutions to the highly cationic RI solutions exhibits a clear bimodal distribution which is mostly pronounced for pH 7.

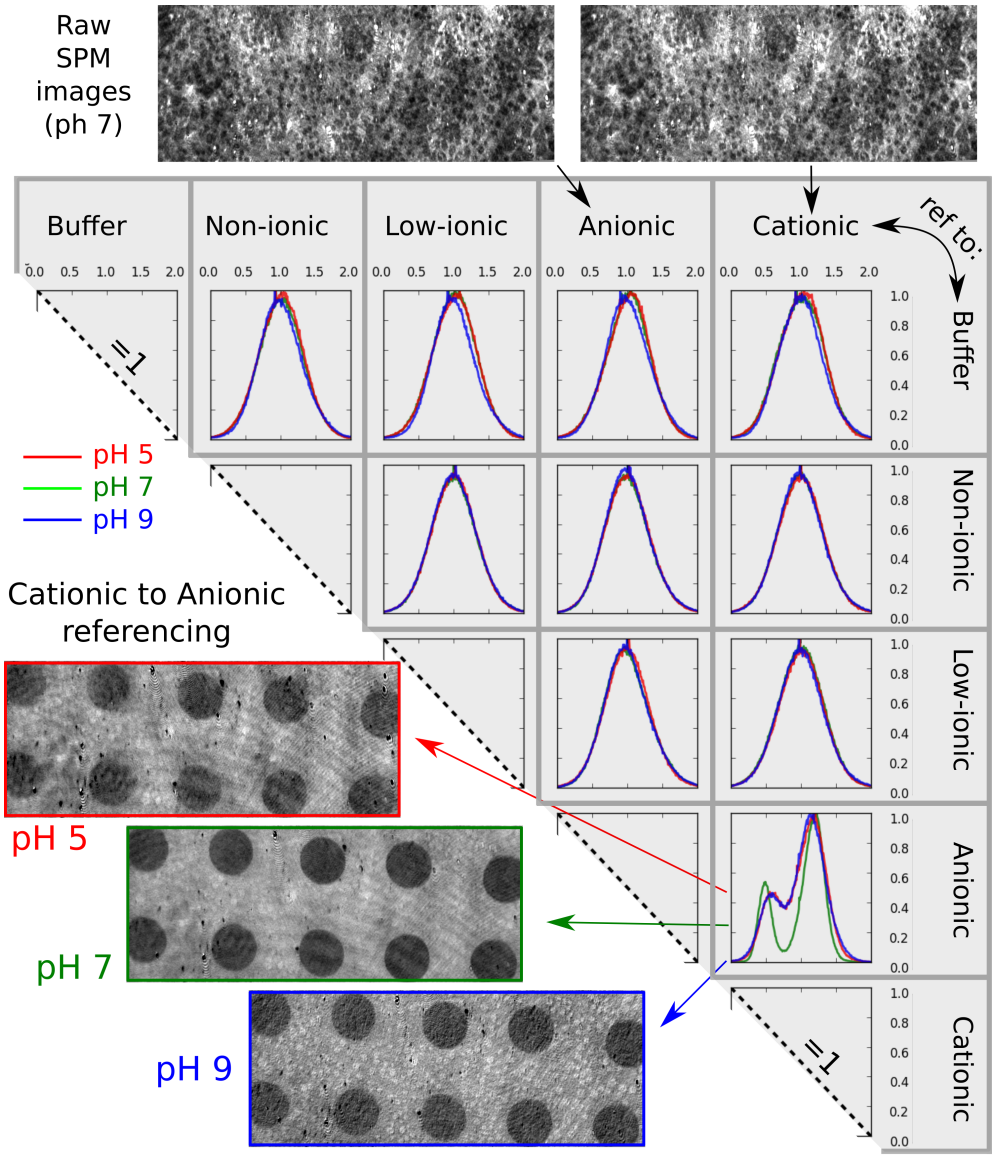

FIGURE 2.11: Ionic referencing using pixel-to-pixel ratio of images measured in two solutions indicated as the column and row of the corresponding cell of the table. All images are intensity normalized thus overemphasizing the details on the image. The curves indicate normalized intensity histograms. Raw SPM images are shown in the upper line.

The corresponding contrast-stretched ratio images are shown in the left bottom part of Fig. 2.11. The surface pattern of monomolecular layers, being not recognizable in raw SPM images, is clearly represented after such a procedure. The ratio image obtained for pH 7 (Fig 2.11) was segmented to two binary masks corresponding to two peaks of its histogram. Using these masks, the total SPR response presented in Fig. 2.10 was separated to signals from two types of coated areas – the spots and the rest of the surface. The results confirmed different SPR responses of these areas in the presence of ions with large molar refraction. The proposed approach is well explained by general principles of surface electrostatics and SPR. Redistribution of ions in the diffuse layer

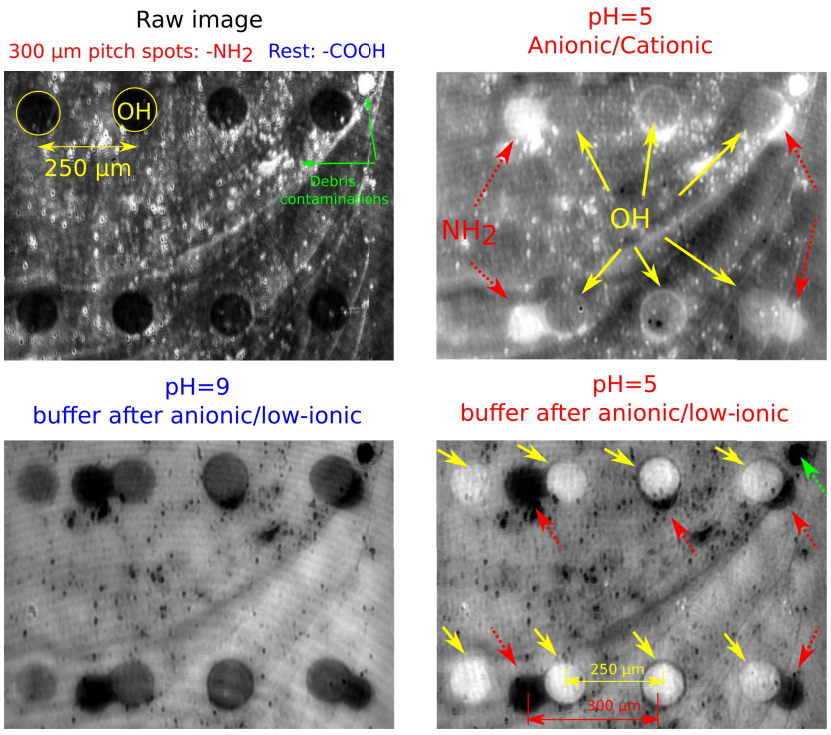

FIGURE 2.12: Gold surface coated by deposition of two overlapped arrays of spots of –OH and –NH_2 terminated alkyl thiols. The rest surface was coated by –COOH terminated alkyl thiol.

near the sensor surface was governed by Coulomb interactions. pH influence on the surface charge leading to some difference in SPR curves (Fig. 2.14, Supplementary), can be also used for ionic referencing. However, the use of the same electrolyte at two different pH for referencing leads to essentially lower contrast than the use of two electrolytes (with large molar refraction of cations and anions correspondingly) at the same pH. Another approach for SPM visualization of different surface properties can be based on physical adsorption. In Fig. 2.12 SPM image of the surface coated by three types of ω-terminated alkyl thiols is shown. Here we intended to deposit two arrays of spots – the first one with –OH and the second with –NH_2 terminal groups; the rest part of the surface was coated by –COOH terminated alkyl thiol. For the disambiguation purposes, the –OH and –NH_2 spots were formed in lines with pitch 250 μm and 300 μm correspondingly. However, one can see in the raw SPM images –OH spots only. To visualize both types of spots, the same procedure of flushing with few electrolyte solutions was applied (Fig. 2.12). The surface areas with –NH_2 terminal groups, being not recognizable in raw SPM images, can be visualized using ionic referencing (Fig. 2.12, upper right panel). It can be also observed that –OH spots overlap fully or partially with –NH_2 spots, however this is not clearly visible because of low contrast between –OH spots and –COOH area. The distinct visualization of all types of coatings was achieved by taking SPM image in buffer after injection of sodium salicylate as the reference. In this case, the –OH and –NH_2 spots are visualized in contrast

to the rest surface and also in contrast to each other (Fig. 2.12, bottom line). This may be explained by different interaction of salicylate anions with three types of coating.

2.2.6 Conclusion

Surface functionalization with different types of thiols is a well-established approach in sensor technology. However, in many cases different functionalization of sensor surface cannot be visualized directly. For this purpose, a visualization of the surface charge of sensor arrays using specifically chosen electrolyte solutions is suggested. It is to note, that this can be done in-situ, at fixed angle and wavelength of incident light, without applying any auxiliary method (e.g. electrochemical modulation or measurement [16, 17]), just by successive flushing of the surface by solutions providing either some adsorption to the deposited self-assembled monolayers or a participation in the formation of electrical double layer near charged self-assembled monolayers. The approach is very robust; it can be applied for the wide range of coating compounds and does not require high quality coatings. For the further contrast improvement, the enhancement of SPR signals by electrically driven adsorption of ions [18] can be considered.

The suggested approach is based on the deviation of contribution of surface layer into refractive index. This deviation should be taken into account when electrolytes with known volume refractive index are used for calibration of SPR systems. The effect can be complicated by potential influence on adsorption of ions [18] or by protonation/deprotonation [19]. To exclude a possible systematic error due to surface effects described in this work, the calibration should be done by addition of low adsorbing non-electrolytes (i.e. glycerol or glucose solutions).

Acknowledgement

The work was supported by FP7 EC Project "Nanodetector" (FP7-NMP-2011-SME-5, #280478). An assistance of Dr. K. Tonder is acknowledged.

References

[1] R. B. M. Schasfoort and A. McWhirter, “SPR Instrumentation,” *Handb. Surf. Plasmon Reson.*, pp. 35–80, 2008.

[2] D. Boecker, A. Zybin, K. Niemax, C. Grunwald, and V. M. Mirsky, “Noise reduction by multiple referencing in surface plasmon resonance imaging,” *Rev. Sci. Instrum.*, vol. 79, no. 2, pp. 2–8, 2008.

[3] S. Nizamov and V. M. Mirsky, “Self-referencing SPR-biosensors based on penetration difference of evanescent waves.,” *Biosens. Bioelectron.*, vol. 28, pp. 263–269, oct 2011.

[4] S. Nizamov, V. Scherbahn, and V. M. Mirsky, "Self-referencing SPR-sensor based on integral measurements of light intensity reflected by arbitrarily distributed sensing and referencing spots," *Sensors Actuators B Chem.*, vol. 207, pp. 740–747, 2015.

[5] B. Rothenhausler and W. Knoll, "Surface plasmon microscopy," *Nature*, vol. 332, pp. 615–617, apr 1988.

[6] J. C. Love, L. A. Estroff, J. K. Kriebel, R. G. Nuzzo, and G. M. Whitesides, "Self-assembled monolayers of thiolates on metals as a form of nanotechnology," *Chem. Rev.*, vol. 105, no. 4, pp. 1103–1169, 2005.

[7] B. Liedberg, C. Nylander, and I. Lundström, "Biosensing with surface plasmon resonance - how it all started," *Biosens. Bioelectron.*, vol. 10, no. 8, pp. 1–9, 1995.

[8] L. S. Jung, C. T. Campbell, T. M. Chinowsky, M. N. Mar, and S. S. Yee, "Quantitative interpretation of the response of surface plasmon resonance sensors to adsorbed films," *Langmuir*, vol. 14, no. 19, pp. 5636–5648, 1998.

[9] M. Yizhak, *Ions in Solution and their Solvation*. John Wiley & Sons, Inc., 2015.

[10] D. R. Lide, *CRC Handbook of Chemistry and Physics*. Boca Ralton, FL: CRC Press, 2005.

[11] V. Scherbahn, S. Nizamov, and V. M. Mirsky, "Plasmonic detection and visualization of directed adsorption of charged single nanoparticles to patterned surfaces," *Microchim. Acta*, vol. 183, no. 11, pp. 2837–2845, 2016.

[12] S. Nizamov, V. Scherbahn, and V. M. Mirsky, "Detection and quantification of single engineered nanoparticles in complex samples using template matching in wide-field surface plasmon microscopy," *Anal. Chem.*, vol. 88, no. 20, pp. 10206–10214, 2016.

[13] C. T. Campbell and G. Kim, "SPR microscopy and its applications to high-throughput analyses of biomolecular binding events and their kinetics," *Biomaterials*, vol. 28, no. 15, pp. 2380–2392, 2007.

[14] S. Nizamov, O. Kasian, and V. M. Mirsky, "Individual detection and electrochemically assisted identification of adsorbed nanoparticles by using surface plasmon microscopy," *Angew. Chemie - Int. Ed.*, vol. 55, pp. 1–6, 2016.

[15] R. Radke, S. Andra, O. Al-Kofahi, and B. Roysam, "Image change detection algorithms: a systematic survey," *Image Process. IEEE Trans.*, vol. 14, no. 3, pp. 294–307, 2005.

[16] C. MacGriff, S. Wang, P. Wiktor, W. Wang, X. Shan, and N. Tao, "Charge-Based Detection of Small Molecules by Plasmonic-Based Electrochemical Impedance Microscopy," *Anal. Chem.*, vol. 85, pp. 6682–6687, jul 2013.

[17] K. J. Foley, X. Shan, and N. J. Tao, "Surface Impedance Imaging Technique," *Anal. Chem.*, vol. 80, pp. 5146–5151, jul 2008.

[18] L. V. K., N. Shavkat, and M. V. M., "The Role of Anion Adsorption in the Effect of Electrode Potential on Surface Plasmon Resonance Response," *ChemPhysChem*, vol. 18, pp. 1552–1560, mar 2017.

[19] K. P. Fears, S. E. Creager, and R. A. Latour, "Determination of the Surface pK of Carboxylic- and Amine-Terminated Alkanethiols Using Surface Plasmon Resonance Spectroscopy," *Langmuir*, vol. 24, pp. 837–843, feb 2008.

Supporting information

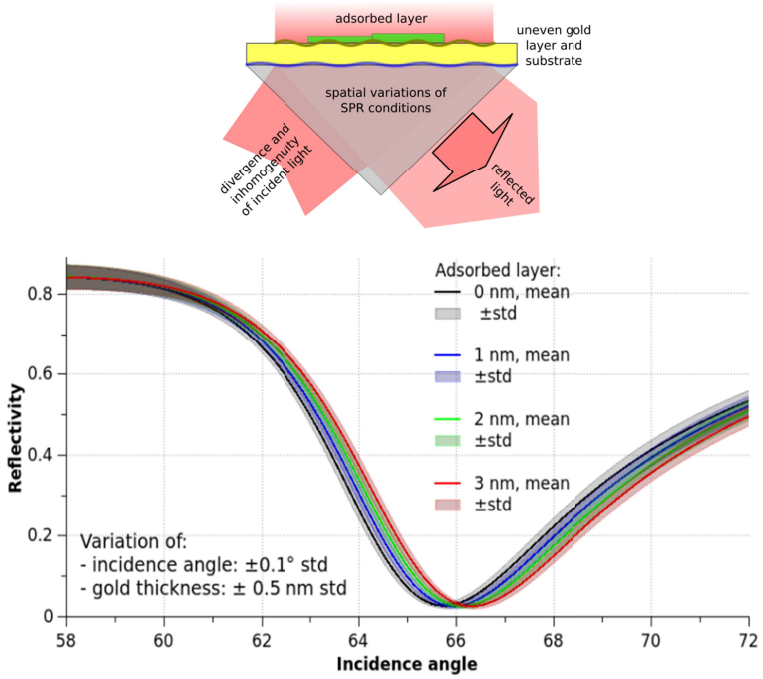

FIGURE 2.13: Variations of SPR curves for small variations of incidence angle and gold layer thickness. SPR curves for organic (PMMA) layers with thicknesses from 0 to 3 nm are shown.

Small variations of incidence angle and the thickness of gold layer already lead to very large variations of SPR curve (Fig. 2.13). For the calculation of SPR curves the transfer matrix method was used. The following parameters were used (refractive index and reference in parentheses): wavelength is 635 nm, the semi-infinite layer of F2 glass (1.616), 1 nm Ni layer (1.964+3.729j), 45 nm Au layer (0.179+3.069j), polymethylmetacrilate layer (PMMA, 1.489 [1]), semi-infinite layer of water (1.332 [2]). 1000 random variations of angle deviation and gold thickness deviation were simulated, for obtained simulation results the mean value and standard deviations were calculated. Just a 0.5 nm change in the thickness of the gold layer, which is roughly twice the diameter of gold atom, may influence light reflectivity at fixed wavelength as much as a 1 nm thick adsorbed layer. Thus, the effect of the small changes in the thicknesses and optical properties of the organic layer adsorbed over the gold surface can be easily overwhelmed by the effect of unevenness of the substrate or gold layer, by inhomogeneity of illumination or by other factors influencing resonance conditions. Most of these factors do not change during the measurement; therefore, their influence is systematic and can be compensated by corresponding referencing. For the investigation of adsorption/desorption kinetics this systematic deviation remains insignificant. However, this influence is essential if the referencing for initial stage is impossible. This is the case in analysis of surface patterning by SPR microscopy.

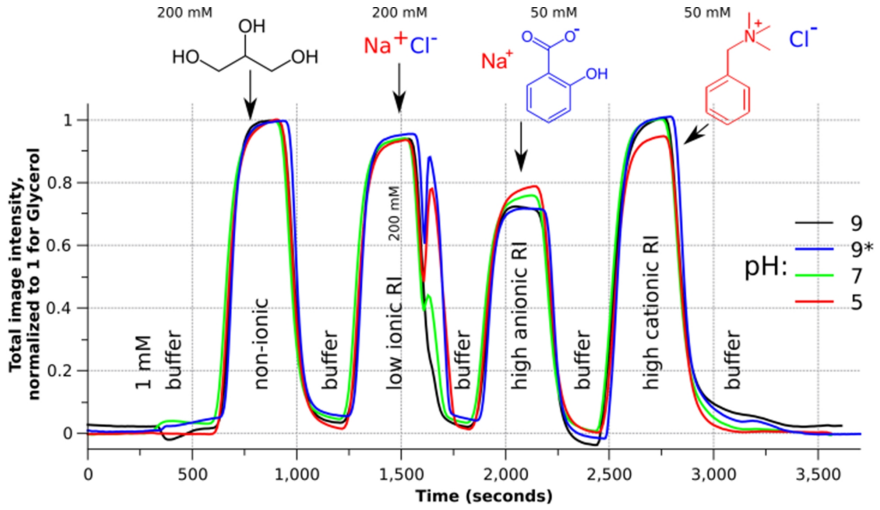

FIGURE 2.14: Integral SPR responses on the sequence of solutions with addition of glycerol, sodium chloride, sodium salicylate and benzyltrimethylammonium chloride at different pH.

References:

[1] S. N. Kasarova, N. G. Sultanova, C. D. Ivanov, I. D. Nikolov. Analysis of the dispersion of optical plastic materials. Opt. Mater. 2007, 29, 1481–1490.
doi:10.1016/j.optmat.2006.07.010.

[2] The International Association for the Properties of Water and Steam. Release on the Refractive Index of Ordinary Water Substance as a Function of Wavelength, Temperature and Pressure. 1997, Erlangen, Germany.

2.3 Plasmonic detection and visualization of directed adsorption of charged single nanoparticles to patterned surfaces

SCHERBAHN, V.,NIZAMOV, S., & MIRSKY, V. M.

Published in: Microchimica Acta, 183(11), 2837–2845. (2016)
DOI: 10.1007/s00604-016-1956-7

2.3.1 Abstract

It has recently been shown that surface plasmon microscopy (SPM[2]) allows single nanoparticles (NPs) adsorbing to the sensor surfaces to be detected and analyzed. The authors have applied this technique to study the adsorption of single metallic and plastic NPs. Binding of gold NPs (40, 60 and 100 nm in size) and of 100 nm polystyrene NPs to gold surfaces modified by differently ω-functionalized alkyl thiols was studied first. Self-assembled monolayers (SAM) with varying terminal functions including amino, carboxy, oligo(ethylene glycol), methyl, or trimethylammonium groups were deposited on gold films to form surfaces possessing different charge and hydrophobicity. The affinity of NPs to these surfaces depends strongly on the type of coating. SAMs terminated with trimethylammonium groups and carboxy group display highly different affinity and therefore were preferred when creating patterned charged surfaces. Citrate-stabilized gold NPs and sulfate-terminated polystyrene NPs were used as negatively charged NPs, while branched polyethylenimine-coated silver NPs were used as positively charged NPs. It is shown that the charged patterned areas on the gold films are capable of selectively adsorbing oppositely charged NPs that can be detected and analyzed with ~ 1 ng mL^{-1} detection limit.

2.3.2 Introduction

Detection, quantification, and characterization of nanoparticles of biological origin or engineered nanomaterials is the actual challenge of different fields of analytical science, including food and environmental safety, bioanalytics, and medical diagnostics [1–4]. Several methods to detect single nanoparticles (NPs) were reported [5]. One of such techniques is based on surface plasmon resonance (SPR) which belongs to the highly sensitive refractometric transducers [6] and has become a routine technique for investigation of interactions of biomolecules [7, 8]. This approach has been also realized as an imaging system (SPR imaging or SPM – surface plasmon microscopy) [9].

The sensitivity of SPR devices is limited by fluctuations of refractive index of aqueous environment [10, 11] and can be increased by corresponding referencing. This referencing was performed using the measurements at two different wavelengths

[2] also denoted as (wide-field) surface plasmon resonance microscopy, (WF)-SPRM

[12, 13] or at closely placed sensing and referencing spots [14, 15], while the mathematical procedure was realized using image analysis [14], electrical [12] or optical [15] subtraction. It has been recently demonstrated that adsorption of NPs to the resonant layer of SPR sensors provides well measurable signals. A high sensitivity of this approach is also based on the referencing: a few μm vicinity around these NPs in course of their adsorption is compared with the rest of the sensor surface.

Two SPM approaches for detection of single nanoparticles have been developed [5, 16–20]. Both are based on the excitation of surface plasmons in Kretschmann configuration. But the optical system used for coupling and imaging of the sensor surface under conditions of plasmon resonance can be implemented either by using of a high-numerical aperture (high NA) microscope objective [5, 16, 17] or by using separate objectives and camera tilted according to Scheimpflug principle [18–20]. The high-NA approach allows one to acquire highly resolved low distortion images but leads to the limitation of the field of view, which is in this case typically smaller than 100 μm x 80 μm (< 0.01 mm^2). Using this approach, metallic and organic nanoparticles have been detected and binding of DNA modified gold nanoparticles to the surface coated by a complementary DNA sequence have been shown [21]. The technique can be used also in air [22, 23] where the difference in the refractive index between analyte and environment is much higher. It was also applied for detection of viruses [24] and for tracking of mitochondria in the living cells [25].

Another approach, contrarily to the high-NA approach, is based on the conventional SPM [9] where the incident light is coupled to a plasmonic sensor layer by a glass prism (Fig. 2.15). This approach leads to a lower numerical aperture of this optical system and to a correspondingly lower optical resolution. However, the sensitivity is still sufficient for detection of single nanoparticles. Such a configuration has been used for detection of single polystyrene nanoparticles (PS NPs) and HIV virus like particles (HIV-VLP) [18, 19]. Despite of the lower spatial resolution, this configuration has an important advantage: the monitored (imaged) surface is much larger – typically few mm^2. Therefore, this approach has a higher dynamic range and lower limits of detection – starting from below 10^6 NPs mL^{-1} up to 10^{10} NPs mL^{-1} thus covering the whole ppb concentration range [26, 27]. The large sensor surface also provides more possibilities for the investigation of the binding of NPs to different surfaces. Moreover, it can be used for deposition of different receptors and for formation of sensor arrays; this is demonstrated in the present work.

We report here a comparative investigation of interaction of citrate stabilized gold nanoparticles (cit-Au NPs) and sulfate-terminated polystyrene nanoparticles (sPS NPs) with various surfaces formed by self-assembly monolayers (SAM) of ω-functionalized alkyl thiols. First, the influence of ionic strength and surface coatings on the binding of cit-Au NPs and sPS NPs was studied. Then, the binding of nanoparticles to the surface patterned by deposition of spots with different ω-functionalized alkyl thiols was registered. The direct detection and visualization of adsorption of single NPs to

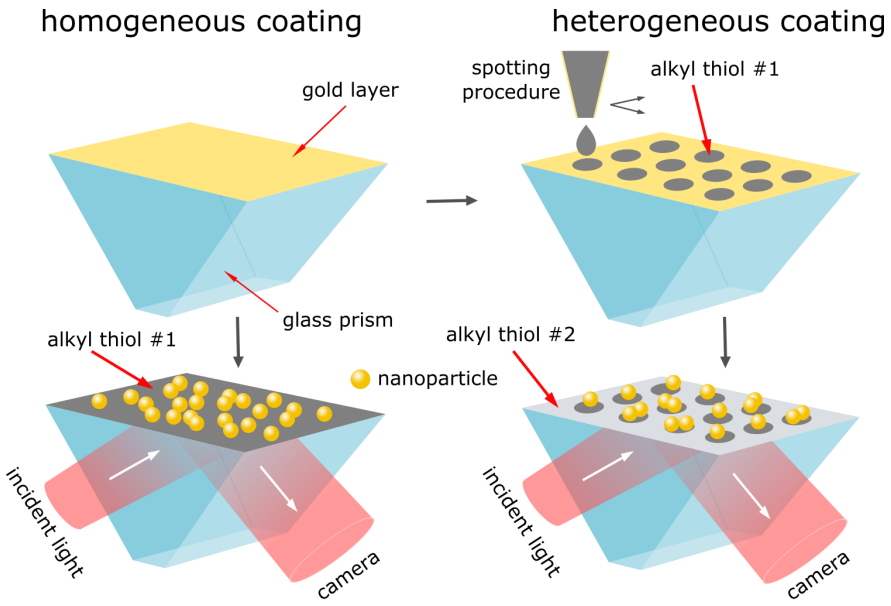

FIGURE 2.15: Self-assembled monolayers of ω-functionalized alkyl thiols were deposited on the gold layer as a homogeneous coating (left panel) or as a patterned layers consisting of two types of ω-functionalized alkyl thiols (right panel). The binding of nanoparticles to such surfaces was detected by surface plasmon microscopy.

the differently functionalized sensor surfaces enables ultrasensitive and unambiguous characterization of NP-surface interaction. A brief schematic illustration of the study is depicted in Fig. 2.15. Negatively charged cit-Au NPs and sPS NPs, and positively charged branched-polyethylenimine-coated silver nanoparticles (bPEI-Ag NP) were applied. The results indicate that the electrostatic interaction is essential for a selective binding of NPs. Therefore, the surfaces patterned by oppositely charged ω-functionalized alkyl thiols can be used as sensors to determine the sign of the surface charge of nanoparticles.

2.3.3 Materials and methods

2.3.3.1 Materials

11-Mercaptoundecanoic acid (C10-COOH), (11-Mercaptoundecyl)tetra(ethylene glycol) (C11-$(EG)_4$-OH), 1 Undecanethiol (C10-CH_3), 11 Mercaptoundecyl amine hydrochloride (C11-NH_2), were purchased from Sigma Aldrich. 11-(Mercaptoundecyl)trimethylammonium chloride (C11-$N^+(CH_3)_3$ Cl^-) was purchased from ProChimia Surfaces (www.prochimia.com), 100 nm latex beads (sulfate-terminated polystyrene nanoparticles, sPS-NPs) and citrate stabilized gold nanoparticles (20 nm, 40 nm, 60 nm and 100 cit-Au NPs) from Sigma Aldrich, sodium citrate from Sigma-Aldrich, 99.9 % ethanol, boric acid and phosphate salts from Merck, dimethyl sulfoxide (DMSO) and sodium chloride (NaCl) from Roth (www.carlroth.com). Branched-polyethylenimine-coated 60 nm silver nanoparticles (bPEI-Ag NP) were purchased from nanoComposix.

All solutions were prepared using deionized water additionally purified by ELGA-Classic system (elgalabwater.com). All suspensions of nanoparticles were diluted to a final concentration of $\sim 1 \times 10^8$ NP mL^{-1}.

The control measurements of hydrodynamic size and ζ-potential of nanoparticles were performed at pH 5 (1mM citrate), pH 7 (1.2 mM phosphate), and pH 9 (1 mM boric acid) using Malvern Zetasizer Nano ZS (www.malvern.com).

2.3.3.2 Functionalization of sensor surface

Prior to functionalization, the gold coated sensor prisms were cleaned for ~120 s by freshly prepared "piranha solution" (1:3 v : v mixture of 32% H_2O_2/H_2SO_4), rinsed thoroughly with water and ethanol, and dried at room temperature. *Caution: piranha solution reacts violently with most organic materials and must be handled with extreme care.* In the next step, the cleaned prisms were put in 1mM ethanolic solution of the corresponding ω-functionalised alkyl thiol, and were incubated overnight at room temperature. Before usage, the prisms were rinsed thoroughly by ethanol, and were dried by air.

The patterned C11-$N^+(CH_3)_3$ Cl^- / C10-COOH surfaces were prepared in two steps. First, 10 mM of C11-$N^+(CH_3)_3$ Cl^- solutions in DMSO were deposited by a non-contact dispenser sci FLEXARRAYER-S3 (www.scienion.com) forming an array of spots of about 100–250 μm diameter with a dot pitch of 200–300 μm. After 20 min incubation in DMSO atmosphere at room temperature, the spotted gold surface was rinsed thoroughly by DMSO and by ethanol followed by incubation in ethanolic solution of 1 mM C10-COOH for 10 min – at this step, the rest of the gold area is functionalized [15]. Due to very slow exchange kinetics of alkyl thiols [28, 29] we assume that this procedure does not lead to any essential modification of the formerly coated spots by C11-$N^+(CH_3)_3$ Cl^- alkyl thiol. Then, the prism was rinsed by ethanol, dried, and mounted in the SPM device.

2.3.3.3 Surface plasmon microscopy setup

The setup for SPM was developed within the EC-FP7 project "Nanodetector" (www.nanodetector.eu). 642 nm SM-fiber coupled laser diode with current and temperature controllers (LP642-SF20, LDC205C and TED200C correspondingly) were from Thorlabs (www.thorlabs.com). Light was collimated by the 16 mm focus length objective (MVL16, Thorlabs, www.thorlabs.de) and directed through 14 mm free aperture Glan polarizer (EksmaOptics, www.eksmaoptics.com) set to the p-polarisation (with regard to the gold coated prism surface). Gold coated sensors consist of SF–10 ($n = 1.72$) glass prisms with 43–45 nm gold layer on 3–5 nm titanium adhesive layer. The slope of the SPR curve and correspondingly the absolute value of the signal of the SPR reflected light shows its maximum at approximately 0.3–0.5 of the SPR reflectivity [30]. However, taking into account the relative changes (the ratio of signal changes to the

mean signal value), the highest signal-to-noise ratio is expected at the angle much closer to the SPR minima [31]. Moreover, in close vicinity to SPR minimum the reflected light intensity tends to zero which makes more affordable a registration of small changes caused by adsorption of nanoparticles. Therefore, the measurements were performed at the angle 0.1–0.3 degrees before SPR minimum. The image was formed on a MT9P031 monochrome CMOS image sensor. The image sensor has a 2592×1944 pixels resolution with a pixel size of 2.2 μm. The images with field of view of about 1.3–1.5 mm^2 were read at ~15 frames per second at full resolution by the Beagleboard-XM single-board computer, averaged over 16 consecutive frames and recorded by PC for further analysis by the homemade software. Initial version of this software was reported in [23] whereas the advanced version based on cluster analysis of images and template matching algorithms was presented in [27].

2.3.3.4 Measurement sequence

The sample suspension was pumped by a solenoid-operated micro-pump (Biochem Valve, 130SP1220-1TP, 12V-DC, www.biochemfluidics.com) at a flow rate of 1 mL min^{-1}. The measurement was started by calibration of the system in the units of the refractive index; it was performed by pumping of a 1.5 mL pulse of the background solution containing additionally 20 mM NaCl. After a washing step, 1.5 mL suspensions of each type of nanoparticles (40 nm, 60 nm, 100 nm cit-Au NPs and 100 nm sPS NPs) were pumped through the flow cell with a washing step in between by 1.5–5 mL of the background solution. The investigation of NPs binding on homogeneously modified surface was performed in 1.2 mM phosphate buffer with and without 200 mM NaCl at pH 7. The calibration was performed in the corresponding buffer containing 20 mM NaCl or 180 mM NaCl (in case of using 200 mM NaCl in the background solution). When using patterned surfaces, no calibration step was performed and, additionally, 60 nm bPEI-Ag NPs suspended in pure water were investigated.

2.3.4 Results and discussion

2.3.4.1 Characterization of nanoparticles

As the work was performed with commercial nanoparticles, their characterization was limited to measurements of ζ-potential and hydrodynamic diameter. The measurements were performed using dynamic light scattering. As shown in Table 2.2, the obtained size values are very close to the data of supplier: the deviation for "100 nm" NPs was below 10 %. No statistically significant changes of their measured size were observed after an increase of the ionic strength by the addition of 200 mM NaCl or after 1-day-incubation at room temperature. An increase of pH from 5 up to 9 leads to a monotonous change in ζ-potential of cit-Au NPs in 1 mM buffer without NaCl with values about -30 mV to -46 mV (Table 2.2). In the presence of 200 mM NaCl the absolute value of the ζ-potential decreases down to the range between 6 mV and -11

TABLE 2.2: ζ-potential and hydrodynamic size of sulfate-terminated polystyrene nanoparticles (sPS NPs) and citrate stabilized gold nanoparticles (cit-Au NPs) at different conditions.

Buffer composition			**sPS NPs**		**cit-Au NPs**	
Buffer	[NaCl] mM	pH	ζ-potential mV	Hydrodynamic diameter, nm	ζ-potential mV	Hydrodynamic diameter, nm
1 mM citrate	0	5	-23.5±1.9	N/A	-29.5±0.9	N/A
1 mM phosphate	0	7	-47.7±5.0	93.9±1.4	-37.2±0.9	109.9±0.6
1 mM boric acid	0	9	-27.4±1.8	N/A	-5.	N/A
1 mM citrate	200	5	-7.4±0.3	N/A	-5.7±0.9	N/A
1 mM phosphate	200	7	-23±1.7	98.5±4.1	-8.7±0.8	109.3±0.3
1 mM boric acid	200	9	-17.7±1.5	N/A	-11.4±0.6	N/A

mV. It can be explained by electrostatic screening where in the presence of 200 mM NaCl the Debye length decreases from 3.6 nm down to 0.7 nm. The surface charge of sPS NPs is determined by sulfate groups which are completely deprotonated in the used pH-range. The observed non-monotonous dependence of the ζ-potential on pH can be explained by adsorption of phosphate ions from the phosphate buffer. Notably, the relatively low values of ζ-potentials at 200 mM NaCl did not lead to aggregation of nanoparticles.

2.3.4.2 Visualization of nanoparticles on the surface

Once a nanoparticle has bound on the sensor surface, it causes a weak optical signal, which can be visualized only after some pre-processing [23]. The crucial step of this analysis is a formation of the differential record acting as a dynamic correction of the background and providing a possibility to compensate not only the static background signal but also some background drift. The result of this operation is the intensity change (differential frame) between two subsequent frames caused mainly by adsorbed (or desorbed) NPs. Therefore the number of images of NPs in each differential frame characterizes the number of nanoparticles adsorbed to (or desorbed from) the surface during the time between two subsequent frames which is ~1.1 s in full resolution.

The penetration depth of evanescent field into aqueous environment is about 200 nm for 650 nm wavelength [12]. Therefore, we can expect that we detect NPs on the surface or at the distance till ~200 nm from the surface. The traveling speed of NPs in aqueous suspension depends on their size; 1.6 m s^{-1} for 10 nm NPs and 5.2 $\times$ 10^{-2} m s^{-1} for 100 nm NPs [32]. Considering the penetration depth of the evanescent field for the 642 nm laser wavelength as ~200 nm, the traveling time of NPs within this region is ~0.1 μs and 4 μs, for 10 nm and 100 nm NPs, respectively, if these NPs are moving perpendicular to the surface. This time is much shorter than the time between subsequent averaged frames, which is ~1.1 s. Therefore, we cannot expect well measurable signals from NPs bouncing from the surface.

The size and shape of the obtained images of adsorbed NPs is the result of complicated interference of the incident, reflected, and diffracted light. These images do

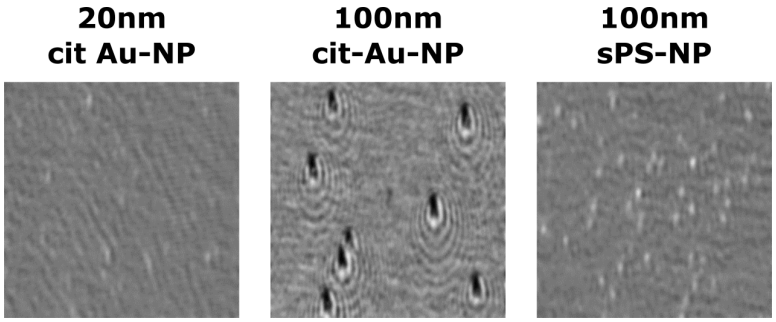

FIGURE 2.16: Differential images showing image intensity patterns of nanoparticles on a surface coated by C11-$N^+(CH_3)_3$ Cl^- alkyl thiol. 20 nm (a), 100 nm citrate stabilized gold nanoparticles (b), and 100 nm sulfate-terminated polystyrene nanoparticles (c) at concentrations ~ 5 $\times$ 10^8 nanoparticles mL^{-1}, except 10^8 nanoparticles mL^{-1} for 100 nm citrate stabilized gold nanoparticles. Image size: 300 $\times$ 300 pixels (~ 0.02 mm^2)

not correspond to the real size and shape of NPs and look like a dark or bright oval spot oval or more complex shapes surrounded by one or more ovals (Fig. 2.16). Their shape is very close to that obtained by theoretical calculations [33, 34]. It is logical to expect that the differential images of the adsorbed and desorbed NPs look like photographic "positives" and "negatives". Therefore, the detailed quantitative analysis of the number and time dependent evolution of these images allows one to get quantitative information on adsorption and desorption of NPs to/from the surface [26, 27]. As single NPs are detectable, their minimal adsorption rate corresponds to one NP per reasonable measurement time. The adsorption rate of one NP per second per total sensor area corresponds to ~ 10^8 nanoparticles mL^{-1} or ~ fM. The optimal concentration range for the detection technology was found to cover the whole ppb range (1–1000 ng mL^{-1}) [27]. An increase of the measurement time and/or sensor area lead to further improvement of the detection limit.

2.3.4.3 Detection of single nanoparticles on surfaces homogeneously coated by self-assembled monolayers

In order to identify the best SAMs for creating heterogeneously patterned sensor surfaces, we first monitored the adsorption behavior of cit Au and sPS NPs on homogeneously coated surfaces. Additionally, we investigated the influence of the higher ionic strength (salinity) on the adsorption of these NPs. For coatings, five types of ω-functionalized alkyl thiols with different terminal moieties were selected: C11-NH_2, C11-$N^+(CH_3)_3$ Cl^-, C10-COOH, C11-EG_4-OH and C10-CH_3. 20, 40, 60, 100 nm cit-Au NPs and 100 nm sPS NPs were used. All types of NPs showed a negative value of ζ-potential (Tab. 2.2) caused by citrate adsorbed on gold NPs or by sulfate groups of plastic NPs. Adsorption of these nanoparticles was studied at pH 7 at low ionic strength (Fig. 2.17a) and in the presence of 200 mM NaCl (Fig. 2.17b). Quantitative comparison based on normalization to C11-$N^+(CH_3)_3$ coated surface possessing the highest adsorption rate, is shown in Fig. 2.17c–f. The values of the Debye lengths in

the buffer solutions with- and without 200 mM NaCl are 3.6 nm and 0.7 nm, correspondingly. Thus, at low ionic strength a strong adsorption of all studied nanoparticles to the positively charged surface formed by C11-NH_2 and C11-$N^+(CH_3)_3$ was observed (Fig. 2.17a, A–B). Oppositely, no binding of sPS or 40 and 60 nm cit-Au NPs to the negatively charged surfaces formed by C10-COOH occurred (Fig. 2.17a, C). This clearly indicates the role of electrostatic interaction in the adsorption of nanoparticles.

Unlike on C11-NH_2 and C11-$N^+(CH_3)_3$ coatings, the behavior of 100 nm cit-Au NPs on C10-COOH and C11-EG_4-OH coatings was quite different: it was possible to observe some weak signals corresponding to two types of images, while one of these images looked like a negative of another one. The magnitude of these signals is much lower than in the case of adsorption to the two positively charged surfaces. Probably, in this case we detect NPs which adsorb/desorb from the surface within one frame. The shortness of NPs' stay on the surface and the exponential decay of their image intensity with the distance to the sensor lead to much weaker signals compared to usual signals from firmly adsorbed NPs. In the case of smaller NPs, such transient signals are not measurable.

In the absence of specific adsorption of sodium and chloride ions, the addition of 200 mM NaCl leads to a decrease of the Debye length down to 0.7 nm and of the absolute values of the surface potentials. Therefore, one can expect a decrease of electrostatic interaction and a subsequent decrease of adsorption of negatively charged NPs to the positively charged surfaces but also a decrease of electrostatic repulsion of these NPs from the negatively charged surface. Such effect was really observed for C11-NH_2 and C11-$N^+(CH_3)_3$ coated surfaces. In this case, a decrease of the number of adsorbed NPs was observed (Fig. 2.17c–f). Notably, in the presence of 200 mM NaCl, a strong adsorption of NPs to the C10-COOH coated surfaces was observed. Therefore, a decrease of the electrostatic barrier leads to adsorption caused by other types of interactions (i.e., Van der Waals attraction). The same adsorption behavior of NPs is observed for the C11-EG_4-OH coated surface, but in this case the physical nature of the energetic barrier is rather unclear.

Direct electrostatic interaction is not expected for C10-CH_3 coating. According to [35], such surfaces can adsorb OH^- ions, but the observed adsorptive properties of these surfaces (Fig. 2.17c–f) are more typical for the positively charged surfaces. The observed influence of the surface coating indicates that the process is not completely limited by diffusion. We cannot exclude some contribution of gravitation into binding of NPs, but the observed influence of the surface coating indicates that this effect is not very strong. An attempt to separate a contribution of the adsorption and of the diffusion processes into the observed adsorption rate will be presented elsewhere.

The results demonstrate that the surface coated by C11-$N^+(CH_3)_3$-terminated alkyl thiol provides the most effective binding of negatively charged nanoparticles. Such coating type can be used as an unselective one for detection of nanoparticles; namely, this coating was applied in our recent work focused on detection and characterization

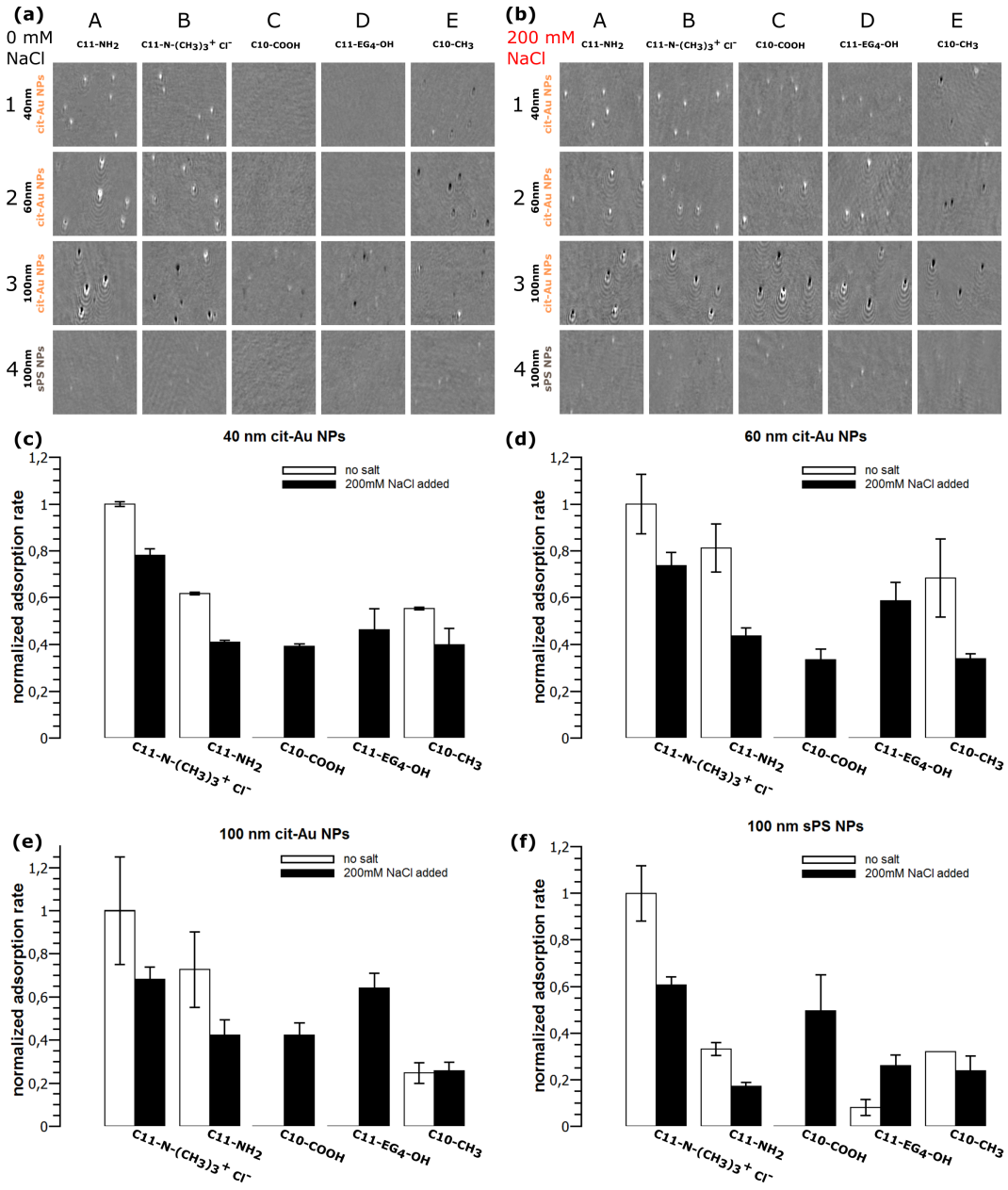

FIGURE 2.17: Differential SPM images of nanoparticles adsorbed on the sensor surface coated by C11-NH_2 (A), C11-$N^+(CH_3)_3$ Cl^- (B), C10-COOH (C), C11-EG_4-OH (D) and C10-CH_3 (E) - alkylthiols. Detection of nanoparticles without (a) and with (b) 200 mM sodium and their corresponding adsorption rates at a concentration of 10^8 nanoparticles mL^{-1} (c–f). The SPM images are cutouts with 300 px × 300 px (~ 0.02 mm^2) from the full visible sensor area (2592 px × 1944 px, ~ 1.3 mm^2).

of nanoparticles in complex media [27]. Albeit few times weaker, the adsorption of nanoparticles to the C11-EG_4-OH coated surface was observed at high ionic strength; thus indicating that such a surface cannot be reliably applied in analytics of NPs as a negative control.

2.3.4.4 Directed binding of single nanoparticles to the patterned surfaces

The highest adsorption rates of negatively charged cit-Au NPs and sPS NPs are observed for the C11-$N^+(CH_3)_3$ Cl^--coating whereas the lowest adsorption rates were observed for C10-COOH coated surface at low ionic strength (Fig. 2.17c-f). These two coatings, providing maximal contrast for binding of NPs, were selected for surface patterning. Using a non-contact piezoelectric dispenser, droplets of $N^+(CH_3)_3$ Cl^- terminated alkyl thiol were deposited to the gold surface. Then, the space between droplets was coated by C10-COOH alkyl thiol. The results of adsorption of different negatively charged NPs to such patterned surface are shown in Fig. 2.18 and in Video 1 (Supplementary material), while the adsorption of the positively charged bPEI-Ag NPs is presented in Fig. 2.19 and in Video 2 (Supplementary material). The measurements were performed at low ionic strength. A clear selectivity of adsorption of all negatively charged NPs to the C11-$N^+(CH_3)_3$ Cl^--coated spots was observed. Almost no binding of 40- and 60 nm cit-Au NPs to the surface coated by C10-COOH was observed, while this selectivity was some lower for sPS NPs and large cit-Au NPs, probably due to the contribution of the gravitation force. Similar results were also obtained for patterned surfaces containing spots with C16-NH_2 and the rest area with C10-COOH.

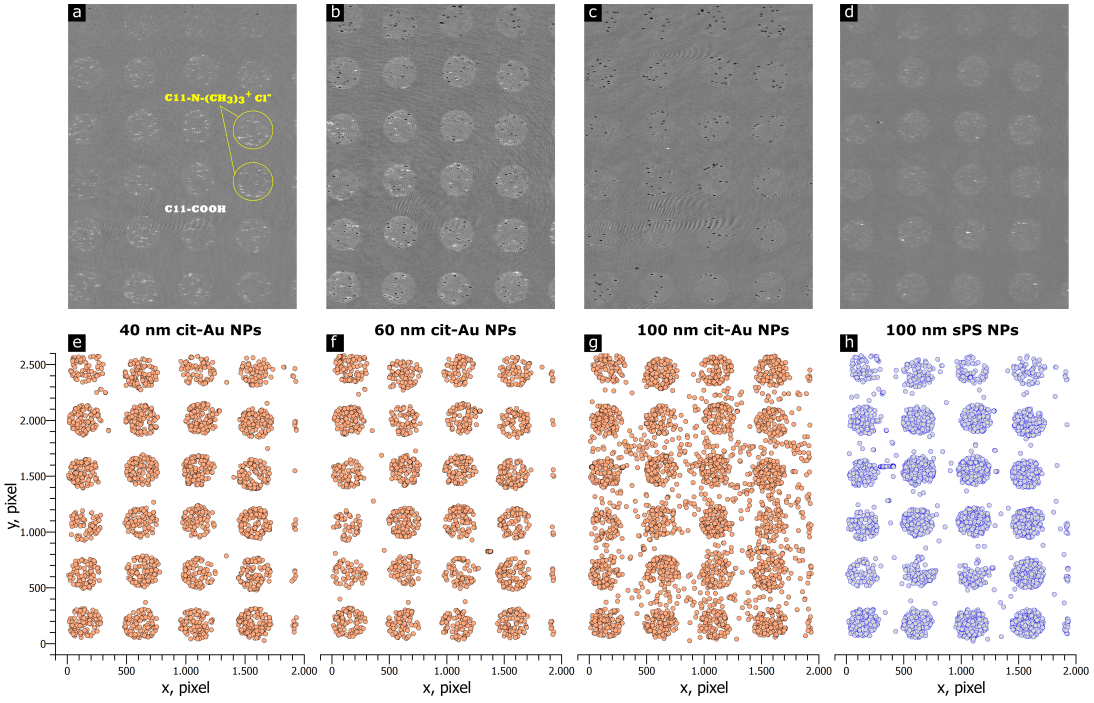

FIGURE 2.18: Visualization of selective adsorption of negatively charged nanoparticles without addition of sodium chloride on a surface coated by spots with C11-$N^+(CH_3)_3$ Cl^-(120–130 μm spot diameter) surrounded by a coating with C10-COOH alkyl thiol. Upper panel: Differential SPM images. Bottom panel: Visualization of nanoparticles adsorbed within 90 s. Visible area is ~ 1.3 mm^2.

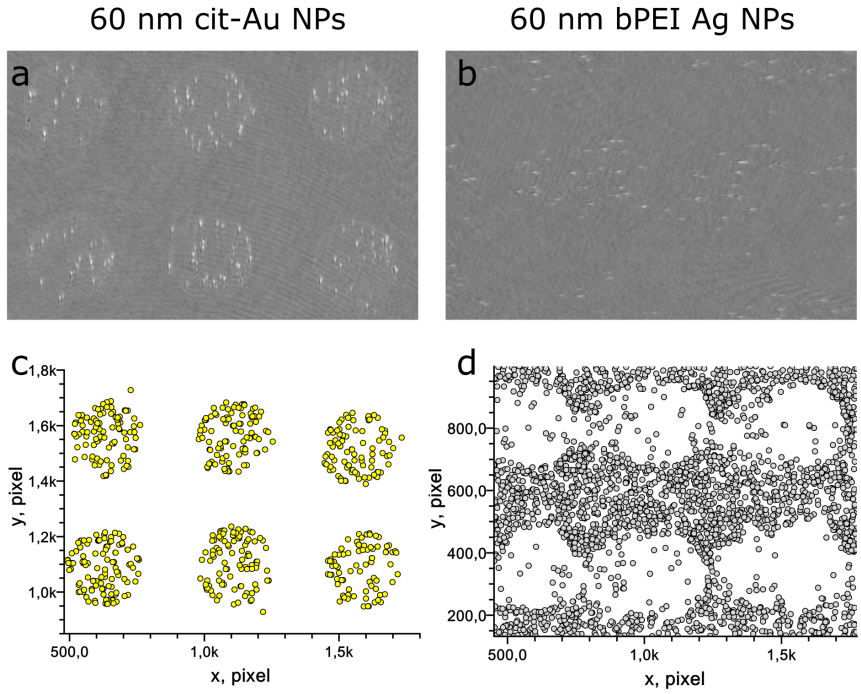

FIGURE 2.19: Visualization of selective adsorption of negatively charged citrate stabilized gold nanoparticles (left pannel) and positively charged branched-polyethylenimine coated silver nanoparticles (right pannel) without addition of sodium chloride on a surface coated by spots with C11-$N^+(CH_3)_3$ Cl^- (120–130 μm spot diameter) and C10-COOH coated area in-between. Differential SPM images (a-b). Visualization of single nanoparticles adsorbed within 90 s (c–d). Visible area is ~ 0.3 mm^2.

The behavior of the positively charged bPEI-Ag NPs showed an opposite effect: they adsorbed to the negatively charged C10-COOH coated part of the sensor surface (Fig. 2.19). The results demonstrate that SPM in combination with the patterned surfaces coated by ω-terminated alkyl thiols with oppositely charged functional groups can be used to distinguish positively and negatively charged NPs.

2.3.5 Conclusion

Wide-field SPM is the real-time label-free optical method for detection of NPs at ppb concentration range. We have applied it for investigation of binding of single nanoparticles to sensor surfaces coated by differently ω-functionalized alkyl thiols. The observed a difference in the adsorption rates to different surfaces indicates on the possibility to develop sensor arrays for analysis of nanoparticles. The concept was proved using the simplest array consisting of patterns with positively charged spots whereas the rest area was coated by negatively charged alkyl thiols. A strong difference in binding of charged nanoparticles to the oppositely charged parts of the surface was observed. This effect can be used for separation of NPs based on the difference in their charge. Additional parameters, which can be used to control the binding of nanoparticles to surfaces, include pH and ionic strength.

The direct detection and visualization of adsorption of single NPs to the differently functionalized sensor surfaces enables ultrasensitive and unambiguous characterization of NP-surface interaction. Besides applications in analytics and basic research, this can be used for nanotoxicology studies. To achieve this aim, the adsorption of nanoparticles to biomimetic surfaces (e.g. coated by phosphatidylcholine and by polysaccharides from glycocalyx) can be determined and compared with toxicity of nanoparticles towards cell lines. Thus, the nanotoxicity related Quantified Structure Activity Relationship (QSAR) for selected nanoparticles can be determined.

Acknowledgement

The work was supported by FP7 EC Project "Nanodetector" (FP7-NMP-2011-SME-5,280478). We are grateful to all project partners for discussions and suggestions. An assistance of Dr. K. Tonder is acknowledged. The authors are grateful to Professors Erik Bakker, Michal Borkovec, Reinhard Niessner and Otto S. Wolfbeis for constructive comments and fruitful suggestions during the discussion of this work.

References

[1] P. H. Hoet, I. Brüske-Hohlfeld, and O. V. Salata, "Nanoparticles – known and unknown health risks," *J. Nanobiotechnology*, vol. 2, no. 1, p. 12, 2004.

[2] C. Medina, M. J. Santos-Martinez, A. Radomski, O. I. Corrigan, and M. W. Radomski, "Nanoparticles: pharmacological and toxicological significance.," *Br. J. Pharmacol.*, vol. 150, no. 5, pp. 552–558, 2007.

[3] M. N. Moore, "Do nanoparticles present ecotoxicological risks for the health of the aquatic environment?," *Environ. Int.*, vol. 32, no. 8, pp. 967–976, 2006.

[4] W. G. Kreyling, M. Semmler-Behnke, and W. Möller, "Health implications of nanoparticles," *J. Nanoparticle Res.*, vol. 8, no. 5, pp. 543–562, 2006.

[5] W. Wang and N. Tao, "Detection, counting, and imaging of single nanoparticles," *Anal. Chem.*, vol. 86, no. 1, pp. 2–14, 2014.

[6] B. Liedberg, C. Nylander, and I. Lunström, "Surface plasmon resonance for gas detection and biosensing," *Sens. Actuator.*, vol. 4, no. C, pp. 299–304, 1983.

[7] R. B. M. Schasfoort and A. McWhirter, "SPR Instrumentation," *Handb. Surf. Plasmon Reson.*, pp. 35–80, 2008.

[8] J. Homola, *Surface Plasmon Resonance Based Sensors*. Springer, 2006.

[9] B. Rothenhausler and W. Knoll, "Surface plasmon microscopy," *Nature*, vol. 332, pp. 615–617, apr 1988.

[10] J. H. Grassi and R. M. Georgiadis, "Temperature-dependent refractive index determination from critical angle measurements: Implications for quantitative SPR sensing," *Anal. Chem.*, vol. 71, no. 19, pp. 4392–4396, 1999.

[11] M. Piliarik and J. Homola, "Surface plasmon resonance (SPR) sensors: approaching their limits?," *Opt. Express*, vol. 17, pp. 16505–16517, 2009.

[12] S. Nizamov and V. M. Mirsky, "Self-referencing SPR-biosensors based on penetration difference of evanescent waves.," *Biosens. Bioelectron.*, vol. 28, pp. 263–269, oct 2011.

[13] T. Zacher and E. Wischerhoff, "Real-time two-wavelength surface plasmon resonance as a tool for the vertical resolution of binding processes in biosensing hydrogels," *Langmuir*, vol. 18, no. 5, pp. 1748–1759, 2002.

[14] D. Boecker, A. Zybin, K. Niemax, C. Grunwald, and V. M. Mirsky, "Noise reduction by multiple referencing in surface plasmon resonance imaging," *Rev. Sci. Instrum.*, vol. 79, no. 2, pp. 2–8, 2008.

[15] S. Nizamov, V. Scherbahn, and V. M. Mirsky, "Self-referencing SPR-sensor based on integral measurements of light intensity reflected by arbitrarily distributed sensing and referencing spots," *Sensors Actuators B Chem.*, vol. 207, pp. 740–747, 2015.

[16] M. G. Somekh, S. Liu, T. S. Velinov, and C. W. See, "High-resolution scanning surface-plasmon microscopy," *Appl. Opt.*, vol. 39, no. 34, pp. 6279–6287, 2000.

[17] B. Huang, F. Yu, and R. N. Zare, "Surface Plasmon Resonance Imaging Using a High Numerical Aperture Microscope Objective," *Anal. Chem.*, vol. 79, no. 7, pp. 2979–2983, 2007.

[18] A. Zybin, Y. A. Kuritsyn, E. L. Gurevich, V. Temchura, K. Überla, and K. Niemax, "Real-time detection of single immobilized nanoparticles by surface plasmon resonance imaging," *Plasmonics*, vol. 5, no. 1, pp. 31–35, 2010.

[19] E. L. Gurevich, V. Temchura, K. Überla, and A. Zybin, "Analytical features of particle counting sensor based on plasmon assisted microscopy of nano objects," *Sensors Actuators, B Chem.*, vol. 160, no. 1, pp. 1210–1215, 2011.

[20] F. Weichert, M. Gaspar, C. Timm, a. Zybin, E. L. Gurevich, M. Engel, H. Müller, and P. Marwedel, "Signal analysis and classification for surface plasmon assisted microscopy of nanoobjects," *Sensors Actuators, B Chem.*, vol. 151, no. 1, pp. 281–290, 2010.

[21] A. R. Halpern, J. B. Wood, Y. Wang, and R. M. Corn, "Single-nanoparticle near infrared surface plasmon resonance microscopy for real-time measurements of DNA hybridization adsorption," *ACS Nano*, vol. 8, no. 1, pp. 1022–1030, 2014.

[22] H. Yu, X. Shan, S. Wang, H. Chen, and N. Tao, "Plasmonic imaging and detection of single DNA molecules," *ACS Nano*, vol. 8, no. 4, pp. 3427–3433, 2014.

[23] I. Sidorenko, S. Nizamov, R. Hergenröder, A. Zybin, A. Kuzmichev, B. Kiwull, R. Niessner, and V. M. Mirsky, "Computer assisted detection and quantification of single adsorbing nanoparticles by differential surface plasmon microscopy," *Microchim. Acta*, vol. 183, no. 1, pp. 101–109, 2016.

[24] L. Wang, W. Ma, L. Xu, W. Chen, Y. Zhu, C. Xu, and N. A. Kotov, "Nanoparticle-based environmental sensors," *Mater. Sci. Eng. R Reports*, vol. 70, no. 3-6, pp. 265–274, 2010.

[25] Y. Yang, H. Yu, X. Shan, W. Wang, X. Liu, S. Wang, and N. Tao, "Label-Free Tracking of Single Organelle Transportation in Cells with Nanometer Precision Using a Plasmonic Imaging Technique," *Small*, vol. 11, no. 24, pp. 2878–2884, 2015.

[26] S. Nizamov, O. Kasian, and V. M. Mirsky, "Individual detection and electrochemically assisted identification of adsorbed nanoparticles by using surface plasmon microscopy," *Angew. Chemie - Int. Ed.*, vol. 55, pp. 1–6, 2016.

[27] S. Nizamov, V. Scherbahn, and V. M. Mirsky, "Detection and quantification of single engineered nanoparticles in complex samples using template matching in wide-field surface plasmon microscopy," *Anal. Chem.*, vol. 88, no. 20, pp. 10206–10214, 2016.

[28] H. Kang, Y. Kim, I. Choi, R. Chang, and W.-S. Yeo, "Determination of self-exchange rate of alkanethiolates in self-assembled monolayers on gold using matrix-assisted laser desorption/ionization time-of-flight mass spectrometry.," *Anal. Chim. Acta*, vol. 843, pp. 38–45, sep 2014.

[29] J. B. Schlenoff, M. Li, and H. Ly, "Stability and self-exchange in alkanethiol monolayers," *J. Am. Chem. Soc.*, vol. 117, no. 50, pp. 12528–12536, 1995.

[30] J. M. Brockman, B. P. Nelson, and R. M. Corn, "Surface plasmon resonance imaging measurements of ultrathin organic films," *Annu. Rev. Phys. Chem.*, vol. 51, pp. 41–63, 2000.

[31] A. Zybin, D. Boecker, V. M. Mirsky, and K. Niemax, "Enhancement of the detection power of surface plasmon resonance measurements by optimization of the reflection angle," *Anal. Chem.*, vol. 79, no. 11, pp. 4233–4236, 2007.

[32] J. Koo and C. Kleinstreuer, "A new thermal conductivity model for nanofluids," *J. Nanoparticle Res.*, vol. 6, no. 6, pp. 577–588, 2004.

[33] A. Demetriadou and A. Kornyshev, "Principles of nanoparticle imaging using surface plasmons," *New J. Phys.*, vol. 17, no. 1, p. 13041, 2015.

[34] T. Son and D. Kim, "Theoretical approach to surface plasmon scattering microscopy for single nanoparticle detection in near infrared region," in *Plasmon. Biol. Med. XII*, vol. 9340, pp. 93400W–93400W–6, 2015.

[35] R. Schweiss, P. B. Welzel, C. Werner, and W. Knoll, "Interfacial charge of organic thin films characterized by streaming potential and streaming current measurements," in *Colloids Surfaces A Physicochem. Eng. Asp.*, vol. 195, pp. 97–102, 2001.

Supporting information

Electronic supplementary material includes video sequences obtained by visualization of adsorption of 40 nm cit-Au NP (Video1.mp4) or 60 nm bPEI-Ag NP (Video2.mp4) to the patterned surface containing the spots coated by C11-$N^+(CH_3)_3$ Cl^--terminated alkylthiol while the rest of the surface was coated by C10-COOH-terminated alkylthiol. Each newly adsorbed NP is indicated by red circle, then its color is changed to the blue one. The red plot below shows the number of NPs adsorbed during the current frame, the blue plot shows the total number of adsorbed nanoparticles.

The video files are available free of charge on the Springer Publications website:

https://link.springer.com/article/10.1007/s00604-016-1956-7#SupplementaryMaterial

as well as on the CD attached to this dissertation.

2.4 Detection and quantification of single engineered nanoparticles in complex samples using template matching in wide-field surface plasmon microscopy

NIZAMOV, S., SCHERBAHN, V., & MIRSKY, V. M.

Published in: Analytical Chemistry, 88(20), 10206–10214. (2017)
DOI:10.1021/acs.analchem.6b02878

Direct link: `https://pubs.acs.org/doi/abs/10.1021/acs.analchem.6b02878`

2.4.1 Abstract

An ultrasensitive analytical method for direct detection of single nanoparticles in complex environment is described. The method relies on the wide-field surface plasmon microscopy (SPM[3]). The suppression of matrix effects is achieved by image analysis based on the template matching. First, characteristic SPM images of nanoparticles are collected in aqueous suspensions. Then the detection of nanoparticles in complex environment is performed using template matching. Quantification and characterization of nanoparticles size was demonstrated at sub-ppb level (~100 pg/mL) in such complex media as wines, fruit juices or cosmetic formulation. Visualization of the nanoparticles is performed in real time. The method does not require any sample pretreatment. If the minimal acceptable adsorption rate is defined as one nanoparticle to the whole sensor surface per few seconds, the working range of the method is ~10^6–10^{10} nanoparticles per mL.

2.4.2 Introduction

Recent growth of nanomaterials application in science, industry, and medicine increased an importance of analytical techniques for detection and characterization of nanomaterials in various consumer products and in real environment. Many approaches have been suggested for this task, but the analysis of nanoparticles in media of diverse and complex constitution is still a major challenge [1–4]. One of the emerging analytical methods for such purpose is based on the surface plasmon microscopy.

The surface plasmon microscopy [5] can be used as an ultra sensitive method for real time label free individual detection of adsorption of nanoparticles to plasmonic sensor surfaces. It can be typically used in two arrangements: using a high numerical aperture (NA) microscope objective [6, 7] and using a classical Kretschmann setup [8–10]. The field of view of high-NA objective approach is limited by the field-of-view of the used objective (typically, below 0.01 mm^2), but the obtained image has a high

[3] also denoted as (wide-field) surface plasmon resonance microscopy, (WF)-SPRM

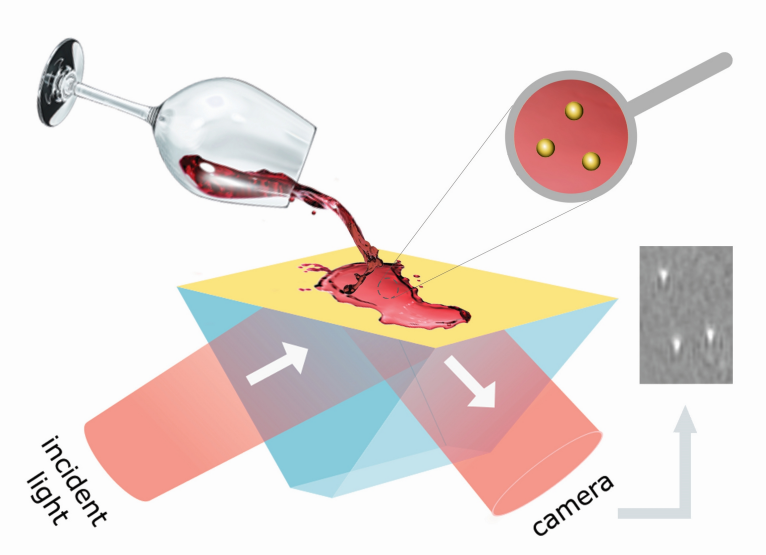

FIGURE 2.20: Graphical abstract

optical resolution and low distortions. The classical Kretschmann setup has a much wider field of view (over 1 mm^2) [9, 10]; however, the mutual tilt of the object, lens, and image planes degrades the performance and resolution of the optical system. At low resolutions it is also widely referred to as an SPR imaging [11, 12]. According to the Fick's law for one-dimensional case (the coordinate x is normal to the surface), the diffusion flux of nanoparticles J is proportional to the sensor surface area A, diffusion coefficient D, and gradient of nanoparticles concentration $C(x)$:

$$J = -AD\frac{dC}{dx} \tag{2.7}$$

Assuming that NPs adsorb irreversibly to the sensor surface [6], $C(0) = 0$, and at a distance beyond unstirred layer with thickness δ the bulk concentration is kept constant $C(x > \delta) = C_0$, we get $\frac{\delta C}{\delta x} \approx \frac{C_0}{\delta}$ and

$$J \sim ADC_0 \tag{2.8}$$

The minimal measurable adsorption rate corresponds to the detection of one NP per reasonable measurement time (e.g. per ~10 s), this gives $J_{min} = 0.1$ NPs/s. Obviously, a larger sensor area allows one to measure a lower NPs concentration C_0. Therefore the classical wide-field SPM is advantageous for analytical applications where the concentration of NPs in sample may be very low.

The principle of the wide-field SPM detection of NPs is shown in Fig. 2.21. In SPR conditions the incident light is coupled to the surface plasmons wave with evanescent field decaying from the sensor surface inwards solution. A nanoparticle, adsorbing to the sensor surface and thus getting into the evanescent field, disturbs the propagation of the surface plasmon wave. This can be observed in the image formed by the

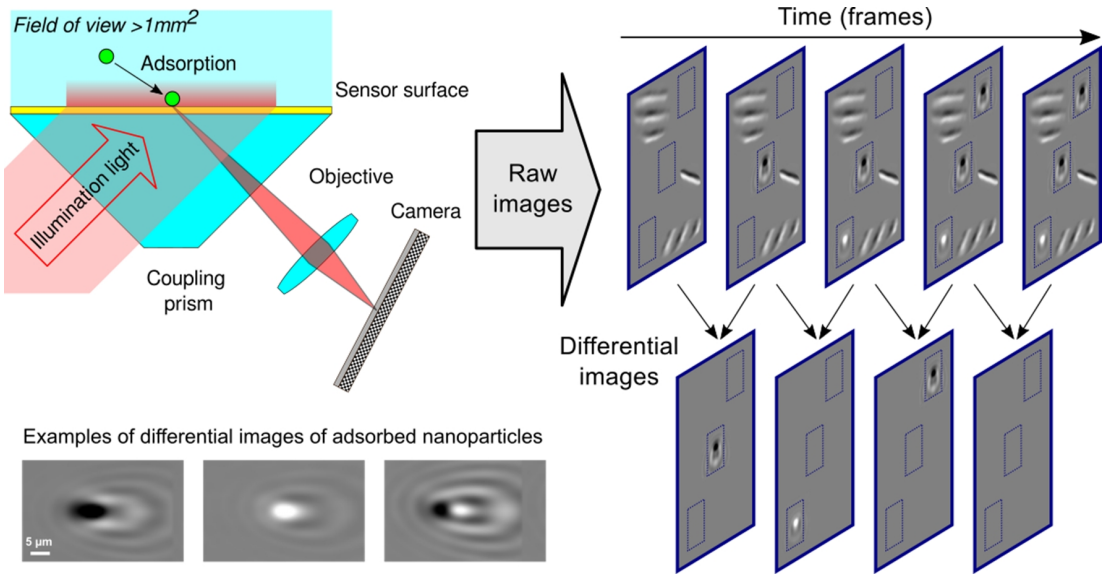

FIGURE 2.21: SPM detection of single adsorbing nanoparticles.

reflected light.

While the manual image processing can be applied for the data analysis of images obtained by SPM during nanoparticles adsorption, it is laborious, error-prone and strongly influenced by personal perception of images. For the wide-field SPM arrangement, where the amount of the detected nanoparticles is counted from single NPs up to the tens or hundreds of thousands, the manual counting approach is not suitable at all. The case becomes even more difficult for analysis of samples with complex content, where the matrix components affect the image peculiarities and may be falsely identified. Namely, this unavoidable matrix effect is the main challenge in the development of analytical techniques for detection of nanoparticle in real media. We present here a new wide-field SPM based approach which is suitable for detection, quantification and characterization of nanoparticles in very complex matrix. Suppression of matrix effects in this approach was achieved by image analysis based on the template matching. The approach was verified by its application for detection of nanoparticles in such complex probes as wines, juices or cosmetic formulations.

2.4.3 Experimental section

The principle of the detection of nanoparticles using the surface plasmon microscopy is described in [8]. The setup for SPM was developed within the EC-FP7 project "Nanodetector" and described in [9, 10]. 642 nm SM-fiber coupled laser diode with current and temperature controllers (LP642-SF20, LDC205C and TED200C correspondingly, www.thorlabs.com) was used as a light source. The light was collimated to a parallel beam by the 16 mm focus length objective (MVL16, Thorlabs, www.thorlabs.de). Polarization of light beam was set to *p*-polarisation (with regard to the gold coated

prism surface) using 14 mm free aperture Glan polarizer (EksmaOptics, www.eksma-optics.com). Gold coated sensors consist of SF–10 ($n = 1.72$) glass prisms with 43–45 nm gold layer on 3–5 nm titanium adhesive layer (www.phasis.ch). The light reflected from the plasmonic sensor surface was focused on the MT9P031 monochrome CMOS image sensor (ON Semiconductor) by optical system with input aperture 18 mm and focal distance 23 mm (NA=0.39). The image sensor has 2592 $\times$ 1944 square pixels with 2.2 μm size. The total magnification of the optical system is ~4.5, thus each pixel corresponds to ~0.5 μm of SPR-sensor surface. Optical resolution of the setup being limited by diffraction is ~2 μm.

Prior to functionalization, the gold coated sensor prisms were cleaned by freshly prepared "piranha solution" (1:3 v : v mixture of 32 % H_2O_2/H_2SO_4), rinsed thoroughly with water, ethanol and dried at room temperature. *Caution: piranha solution reacts violently with most organic materials and must be handled with extreme care.* In the next step, the cleaned prisms were introduced in 1 mM 11-(mercaptoundecyl)-trimethylammonium chloride (MUTMA) in ethanol and incubated at least overnight at room temperature. Before usage, the prisms were rinsed thoroughly by ethanol and dried by air stream.

MUTMA was purchased from ProChimia Surfaces (www.prochimia.com). Sodium chloride (NaCl) was from Roth (www.carlroth.com). All solutions and suspensions were prepared using deionized water, additionally purified by ELGA-Classic device (elgalabwater.com) and filtered using 200 nm cellulose acetate syringe filters from VWR International (www.wvr.com). 100 nm latex beads (polystyrene nanoparticles, PS-NP), citrate stabilized gold nanoparticles (AuNP, 20 nm, 30 nm, 40 nm, 60 nm, 80 nm, and 100 nm in diameter), 40 nm citrate stabilized silver nanoparticles (Ag NP), and TiO_2-NP (< 150 nm in diameter) were from Sigma Aldrich (www.sigmaaldrich.com). Aqueous suspensions of PS-NPs and AuNPs were prepared at final concentrations of about 10^8 NP/mL. TiO_2-NP were prepared at concentrations between 0.9–900 ng/mL. The size of nanoparticles was proved by dynamic light scattering (DLS) using Nano-ZS ZEN3600 (www.malvern.com). The stock concentrations of nanoparticles were proved using nanoparticle tracking analyzer NTA5330 with 532 nm laser module (Nanosight, www.malvern.com). Except long time repeatability measurements, each probe before injection was treated for few seconds with vortex shaker Lab Dancer S40 (VWR International).

All solutions and suspensions were pumped by a solenoid operated micro-pump (Biochem Valve, 130SP1220-1TP, 12V-DC) at a flow rate of 1 mL/min. First, a calibration of SPM system by injection of aqueous solution containing additional 20 mM NaCl followed by washing with the same solution without salt was performed. Then, 1.5–2 mL suspensions of nanoparticles were injected, the same volume was also used for washing steps in between.

The main part of the work was performed with three types of complex media: white wine, suncream, and apple juice. Other successfully tested probes include tap

water, mineral water, red wine. The samples in wine were prepared as suspensions containing various concentrations of 40 nm Ag NP (10^6–10^{10} NP/mL) in 80 % white wine (Chardonnay 12% vol., pH 3.4). To prepare the sample with cosmetics, suncream containing 5 % w/w polydisperse TiO_2-NP (Ahava, Israel) was diluted by water 1 : 10^4–1 : 10^6. The samples of Au-NP in 90 % v/v apple juice (pH ~ 4) were prepared as the suspensions containing 3×10^8 NP/ml of the nominally single size (30 nm, 40 nm, 60 nm, 80 nm, 100 nm) or of the mixtures (30/60 nm, 30/80 nm, 30/100 nm, 40/60 nm, 40/80 nm, and 40/100 nm) of NPs.

2.4.4 Results and discussion

In most cases the image changes caused by adsorption of NPs are very weak. To detect such changes and to suppress the static and slowly changing background in SPM raw frames the differential frames showing the changes between two frames were calculated. To combine a calculation of the differential image with normalization to the incident light intensity, it is convenient to calculate the differential frame as the pixel-to-pixel ratio of two subsequent frames [13] (frame_{N+1} / frame_N). The time required for the NP to cross the vicinity of the sensor surface within the penetration depth of the evanescent field (~ 150–300 nm [14]) is smaller than the frame time (~ 1.1 s). Therefore, the NPs adsorbed within the frame N contribute to the measured light for only a part of the frame time, and the full contribution of these NPs into the image intensity is spread over two differential frames: frame_{N+1} / frame_N and frame_N / frame_{N-1}. To capture the full contribution of NPs adsorbed within the frame N the differential frames were calculated as the ratio frame_{N+1} / frame_{N-1}. The stepwise change of light intensity due to adsorption of a NP was used for additional filtration.

The pixel values in differential frames close to unity (~ 1, grey background on Fig. 2.21) denote no changes in the SPM raw frames, whereas a sharp intensity changes result in values higher (> 1, white) or lower than the unity (< 1, black). Adsorption of NPs is manifested in differential frames as a change within a group of neighboring pixels, giving the characteristic black-and-white image pattern (see Fig. 2.21). The size, shape, and intensity of the images of NPs are mainly determined by size, refractive index of NP and its distance to the plasmonic substrate (theoretical analysis was reported in [15–18]) and by optical system used for imaging.

The straightforward approach for automated data analysis of wide-field SPM records relying on the image filtration and detection of local temporal and spatial intensity changes in differential SPM frames, was reported [9, 19]. This approach considers an image of adsorbed nanoparticle as a spot of some defined size range and does not pay much attention to its particular shape and intensity distribution over the image (Fig. 2.22, left). Correspondingly, any perturbations of this size in the differential SPM images may be falsely identified as adsorbed NPs. If some NP images have a shape very much different from the Gaussian shape, they might be either not recognized or

recognized as many spurious Gaussian blobs of various sizes. Such problems are especially pronounced in noisy SPM records obtained in the presence of some matrix. This interference hindered an application of SPM for detection of NPs in food, cosmetics or other complex media so far.

The presence of very large and/or very small particles and compounds can be probably avoided by development of an effective extraction of NPs. However, such pretreatment is not just an expensive and laborious procedure which should be developed for each particular type of probes; it may also change substantially the concentration and properties of NPs and thus lead to incorrect results. Therefore, an application of SPM for detection, quantification and characterization of NPs in very complex probes (such as industrial wastes, environmental waters, food and drinks, biological liquids and tissues) requires approaches for the suppression of the matrix effects. With this goal, a robust method for detection and identification of NPs in media of complex composition was developed.

The principle and comparison of the described double-pass and earlier reported single-pass methods are shown in Fig. 2.22. In the single pass approach, the detection of NPs is based on detection of blobs in the sequence of differential images. To suppress an interference from matrix and to provide reliable analysis of SPM records with a low signal-to-noise ratio we suggest to exploit the distinctive shape of NP images (Fig. 2.21). For the recognition of NP images in SPM records, the method of template matching using normalized correlation coefficient (NCC) 20 was applied.

The required image templates can be extracted in different ways. An obvious approach is to use simple (e.g. aqueous) suspensions of the NPs of the same type. However, one can not exclude an influence of the media on the NP images. Therefore, an extraction of NP images from the SPM record obtained directly in the complex analytical probes spiked with additionally introduced NPs may be a more appropriate approach (it can be considered as an analogue of the technique of standard additions). The goal of the first pass over the SPM record is an extraction of the image templates. For this purpose the single pass blob detection method [5] can be applied. Since the intention of this procedure is only to suggest some candidate of NP images and not to detect NP images or to distinguish them from the interfering image features, a high amount of false positives or negatives can be tolerated if the gathered candidate images contain sufficient amount of true positives. After some amount of images (containing both NP images and any junk images) is collected, the mostly common image templates in this collection are determined. This is performed by clusterization of images by their similarity. This idea was realized using a graph, where the images represent the nodes, and their NCC-expressed similarity serves as the weighted edge. The applied NCC implementation [20] is not just numerically fast, but also reports the mutual image displacement for the highest possible NCC. After calculation of the pairwise similarities (edges), the best two matching images were selected and summed. The summation was performed using a mutual displacement that gives the highest

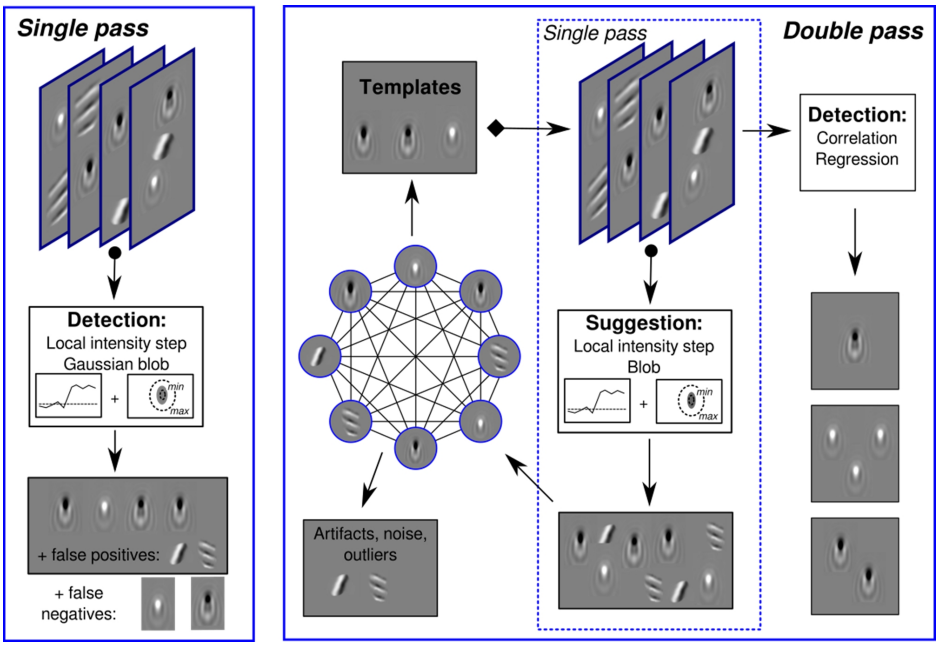

FIGURE 2.22: Single pass (blob detection) and herein described double pass (template determination and matching) approaches.

NCC. Then the selected pair of nodes was deleted from the graph and the calculated image was inserted instead. Thus, the shortest edge in the graph was removed, and two corresponding nodes were merged (edge contraction). It is to note that the result of the summation of the two merging images has an increased signal-to-noise ratio (SNR). If the noise in images is independent (e.g. pixel shot noise), one can expect an increase in SNR proportional to the square root of the images number. Iteratively repeating the best edge contraction, one can aggregate the mostly similar and frequent images into one or several templates. The clusterization procedure is stopped as soon as the best edge falls beyond some threshold (typically 0.6–0.9). Thus, the described algorithm extracts the most frequent candidates of NP images and sorts them according to their recurrence. The typical templates of NP images obtained by this algorithm are shown in Fig. 2.21.

After determination of the image templates of NPs in the first pass, they were applied for detection of NPs in the second pass. It was based on the calculation of normalized correlation coefficient (NCC) and regression coefficient (RC) of the image patch and the template. As soon as they overcome the thresholds, the NP is considered as detected. The data on the adsorption time and adsorption position of each NP were visualized (Supplementary: video). The developed approach was tested using a wide range of consumer products as a matrix. We started from such simple media as tap water or mineral water, and then studied such complex media as wines, fruit juices or suncream. Except suncream, explicitly containing nanoparticles according to its formulation, other probes were spiked with known amount of engineered nanoparticles shortly before the measurement. These known concentrations were considered

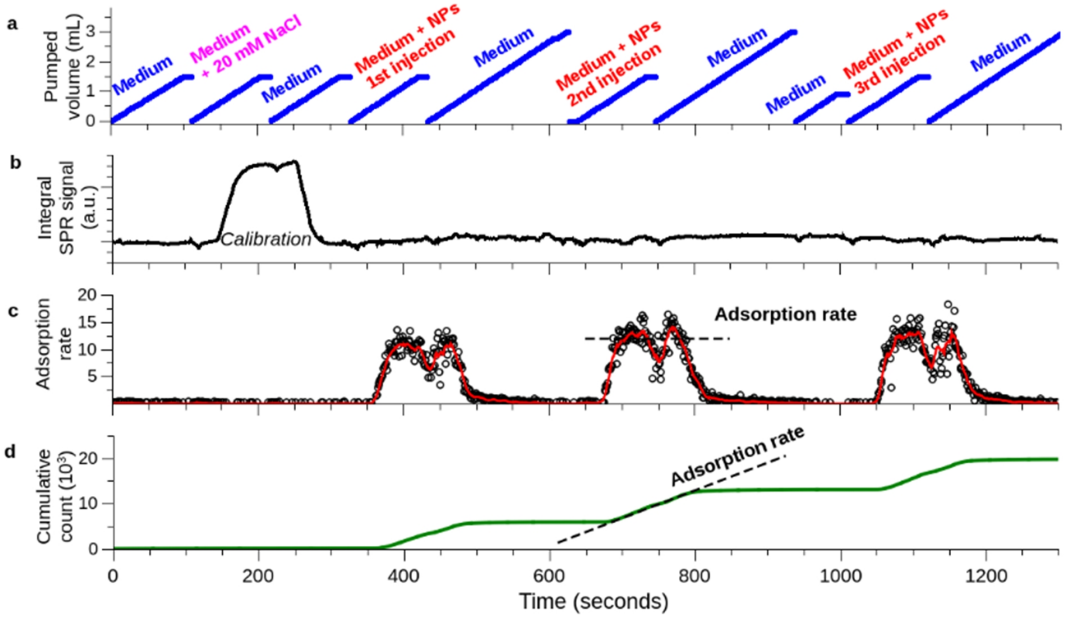

FIGURE 2.23: Detection of 60 nm Ag NPs in 10 mM PBS, pH7 (three repetitions): (a) liquids pumped through flow cell and their volume; (b) integral SPR signal; (c) detected adsorption rate of nanoparticles; (d) cumulative number of detected nanoparticles.

as the reference values for validation of our technique. For image template extraction and for independent DLS/NTA (Nanosight) control of NPs size/concentration, the suspensions of the same NPs in aqueous buffer solutions were used.

A typical sequence of experimental steps is outlined in Fig. 2.23. In the row (a) the liquids pumped through a flow are indicated. The first optional steps include a calibration of the SPR system using injections of medium without NP: an integral SPR signal shift due to increase of the total ion concentration by addition of 20 mM NaCl was measured. This calibration is only required for the comparison of NP image intensities in different experiments and may be omitted if such comparison is not intended. Then the probes were injected. For a better negative control, the injections of the probes can be alternated with injections of medium (Fig. 2.23a). Such optional negative control may be useful to exclude suspected false positives in analysis of particularly complex media; however, we did not observe such a problem with the studied probes. The number of adsorbing NPs within each differential frame was determined using the above described approach and normalized to the sensor surface area and the frame frequency. At constant diffusion conditions, the obtained adsorption rates are proportional to the concentration of NPs in the concentration range from $\sim 10^6$ till $\sim 10^9$ NPs/mL [10]. Integration of adsorption rate gives the cumulative count of adsorbed NPs. The video (Supplementary) visualizes binding of 40 nm Ag NPs from aqueous suspensions. The following sequence of injections was performed: water–10^6 NPs/mL–water–10^7 NPs/mL–water–10^8 NPs/mL. The upper insets show the current number of NPs per frame (left) and the cumulative number of adsorbed NPs so far.

NPs are indicated by red color in the first frames after adsorption; then the color is changed to blue.

It is to note, that the adsorption of NPs is not recognizable in the SPM raw frames: the only noticeable response in Fig. 2.23b is the calibration response. The intensity measurement of SPM raw frames represents the signal of conventional non-imaging and low-resolution imaging SPR sensors. Thus, the Fig. 2.23 shows clearly the advantages of our method over conventional SPR sensors. The cumulative count of adsorbed NPs within three consecutive injections amounts to ~20 000 NPs. The area occupied by 60 nm NP in densely packed hexagonal monolayer is 3.1×10^{-9} mm^2. Therefore, the occupied surface area in this particular measurement is only ~6×10^{-5} mm^2 out of ~1.2 mm^2, this corresponds to the sensor surface coverage of just 0.005 %. The measurement system provides reliable detection at at least two order of magnitude higher surface coverage. At such low surface coverage one can neglect an effect of adsorbed NPs on further NPs adsorption or a random binding of new NPs to the top of the formerly adsorbed NPs.

Repetitive measurements using 3–10 injections demonstrated good reproducibility of the detection. The values obtained for stable aqueous suspensions (Au-, Ag- or PS-NPs) showed the same values during 1 h with standard deviation of the adsorption rate in the range of 5–15 %, for the less stable suspension of TiO_2 NPs a gradual decrease of NPs adsorption with about the same standard deviation of the slope was observed. This decay indicates the possibility to study stability (aggregation or sedimentation) of NP suspensions.

One of the most popular consumer products containing TiO_2 nanoparticles as a part of their formulation are suncreams [21, 22]. The detection of TiO_2 NPs and determination of their concentration in such media is shown on Fig. 2.24. The results were compared with well characterized probe of the same type of NPs in water. Due to high polydispersity of both TiO_2 samples, the weight concentrations are indicated. For the reference purposes and for the image template determination, the aqueous suspensions of TiO_2 with gradually increasing known concentrations in range of ~1–1000 ng/mL (1–1000 ppb) were prepared and studied. Despite the broad size distribution of TiO_2 NPs, only one template was detected; on the other hand, the images of single NPs show large variation in intensity. Using these data, the calibration curve of the adsorption rate vs. concentration was obtained. This dependence is practically linear in the double-log scale over the whole concentration range. Then, the samples of suncream with 5 % w/w TiO_2 content was diluted by water in ratio $1 : 10^4$, $1 : 10^5$, $1 : 10^6$ and measured. Optionally, the diluted samples were filtered using 200 nm cellulose acetate filter. The time duration between vortex treatment and sample injection measurement was few minutes; therefore, a possible loss of TiO_2 NPs due to aggregation or sedimentation can be neglected. The template obtained from the reference suspension was used for detection of NPs in the suncream probe. The detected adsorption rate and the concentration of suncream fits well the calibration curve (Fig.

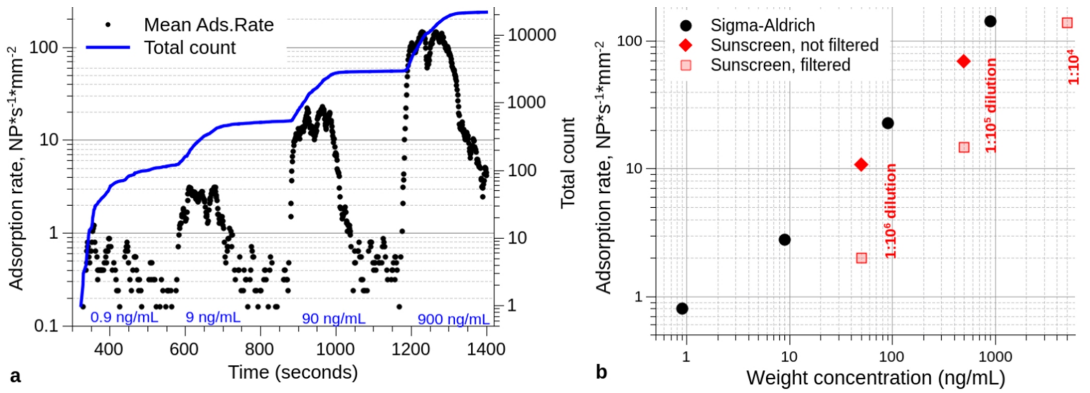

FIGURE 2.24: Analysis of content of TiO_2 NPs in the suncream. The sample was diluted by water $1:10^4$, $1:10^5$ or $1:10^6$ to match the optimal working range of the device. The weight concentrations were calculated using supplier data on the content of TiO_2 (5 % w/w). For comparison, the aqueous suspension of TiO_2 from Sigma-Aldrich was studied.

2.24). The data give the concentration value in the suncream of 4.1 % which is very close to that value indicated by the suncream supplier (5 %). The samples, filtered through a 200 nm filter, show much smaller adsorption rate thus indicating that such pretreatment, typically used to exclude very large particles from complex media, may lead to the severe underestimation of the true concentration. The detection of single TiO_2 NPs within reasonable detection time (few seconds) was performed successfully at ~1 ng/mL, this corresponds to ~1 ppb. Already at this concentration within few minutes one can detect a high enough number of NPs to get statistically representative data. Since the detection time is inversely proportional to the detection limit, also a sub-ppb detection is possible by extending the measurement time.

Other prominent nanomaterials, already being used in different consumer products and thus rising the concerns about their safety, are the formulations containing silver NPs [23, 24]. Detection of such NPs is very challenging due to their inherent chemical instability in aqueous suspensions. Ag NPs may easily aggregate or completely dissolve thus making a discrimination between silver in the form of NPs and silver in other forms (ions, insoluble sediments, microparticles or bulk material) very difficult. To detect silver NPs in the consumer product (red and white wines were chosen), the suspensions of 40 nm silver NPs in wine and water were prepared and measured (Fig. 2.25). The concentration range was in range of 10^6–10^{10} NPs/mL. Calculating the mass of a single NPs as 0.34×10^{-15} g, a mass concentration range of 0.34–3400 ng/mL (or 0.34–3400 ppb, correspondingly) is obtained. The aqueous stock solution of silver NPs had the concentration of 5.7×10^{10} NPs/mL, therefore, the constant content of 80 % wine was chosen for all suspensions prepared by dilution of this stock solution.

Clusterization of NPs images obtained during adsorption of silver nanoparticles in pure aqueous suspensions leads to the single image template, the occurrence rate of other types of images is below 1 %. The concentration dependence shows a good linearity in double log scale in the concentration range from 10^6 till 10^9 NP/mL (Fig.

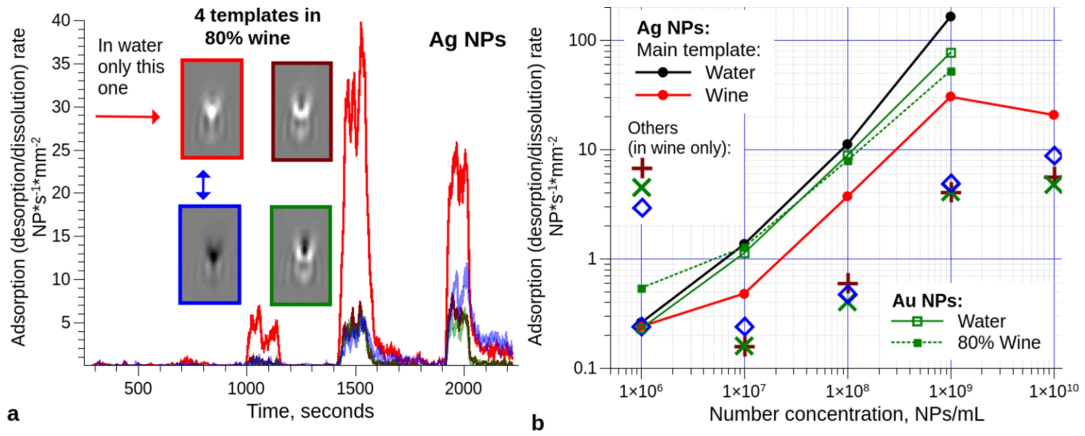

FIGURE 2.25: Detection of 40 nm Ag NPs in water and in 80 % wine. a) Image templates and adsorption rates for injection of different concentrations of Ag NPs in 80 % wine. The color of the frame corresponds to the color of the adsorption kinetics for this type of the template. Only a single image template was obtained for Ag NPs in water while also three other image templates were observed for Ag NPs in wine. b) Concentration dependence of the detected adsorption rate for different image templates. For comparison, a detection of Au NPs in these media is also shown.

2.25b). For the same NPs concentrations in 80 % wine the adsorption rate is few times lower. This discrepancy can be partially explained by 1.8–3.0 times higher viscosity of the wine matrix [25]. However, the discrepancy steadily grows with the concentration increase. After reaching the concentration of 10^{10} NPs/mL, the detected adsorption rate in wine suddenly drops. At the same time, in contrast to the pure aqueous suspensions, the occurrence rate of three other types of image templates is considerably larger in wine suspensions. The contribution of these image templates grows with NPs concentration increase. At a concentration of 10^{10} NPs/mL, these image templates constitute a substantial part of the number of detected images. This allows us to suggest a concentration decrease of silver NPs in wine and a formation of some other types of nano- or microparticles manifested by different image template. This conclusion is confirmed by measurements of Au NPs in the same media: they did not display any noticeable difference being measured in water and in 80 % wine. It is to note that two of these template images are inverses of two others. As it was reported in [10], such images relate to the dissolution (desorption) of silver nanoparticles previously adsorbed to the gold surface. An occurrence of some chemical reaction with silver nanoparticles in wine suspension was supported by DLS measurements. They give the size of Ag NPs in aqueous suspension 40 ± 7 nm well corresponding to the supplier specification. However, the suspensions of this type of Ag NPs in the wine displays an appearance of large particles with the size from 150 till 250 nm. Ag NPs of this size typically sediment irrespectively to their zeta-potential value. This conversion cannot be explained by oxidation of nanoparticles (an addition of this type of wine to aqueous electrolyte results to the shift of the redox potential to cathodic direction), but a more detailed investigation of conversions of Ag NPs in wine is beyond

the topic of this work. Nevertheless, the above described measurements demonstrate that an application of SPM is not limited by counting of nanoparticles, it may also provide an indication on physico-chemical processes with these NPs.

The excellent colloidal stability of Au NPs already lead to numerous applications of Au NPs in science, medicine and industry [26]. Au NPs were suggested to apply as anti-counterfeiting nanotaggants in some consumer products [27]. To model such an application, suspensions of 30–100 nm gold NPs in apple juice were prepared by dilution of the aqueous stock solutions. Correspondingly, the juice content in the suspensions was 90 % while the concentration of NPs was kept equal to 3×10^8 per mL (calculated from the supplier data). The results of analysis are shown in Fig. 2.26a.

The size dependence of the image intensity of Au NPs is shown in Fig. 2.26a. This dependency is approximately linear in the 30–100 nm size range. It is in a good agreement with theoretical analysis [15–17] and with a previous report for the polystyrene sub-microparticles [8].

It is to note that the differential image intensity is dimensionless and can not be quantified directly. Indeed, this is the ratio of the reflected light intensities before and after adsorption of NP. To convert this dimensionless value into representative physical value, a calibration of sensor response by refractive index (RI) step has been done. It was performed by addition of 20 mM NaCl to the medium. From the literature data [14, 28] it is known that this addition causes ~ 180 microRIU change. Thus, having calibrated the sensor response, the differential image intensity (peak-to-peak value) can be expressed in terms of RI (see plots in Fig. 2.26b for Au NPs). It is to note that the image intensity for 30 nm Au NPs is as high as $\sim 10^{-4}$ RIU. Typically, RI resolution limits for the SPR-imaging instruments is in the range of $\sim 10^{-6}$. However, because of low spatial resolution of commercial devices, this relatively large signal from single NP is blurred through a large surface area thus leading to a decrease in its magnitude.

The calibration enables a quantitative analysis and comparison of images obtained in different conditions. The histograms of image intensities in Fig. 2.26b were obtained in independent measurements. Ag NPs in water and wine were measured separately and compared with Au NPs in juice. Since the complex refractive index of bulk Ag and Au at ~ 640 nm are similar, NPs made of these metals induce similar response in SPM; correspondingly, their normalized histograms display a good coincidence as well. A broader distribution of image intensities for Ag NPs in wine in comparison with that in water can be considered as an additional indication of influence of media on Ag NPs.

The distribution of image intensities can be also used for analysis of polydisperse samples. The histograms for the 40/60, 40/80, 40/100, 30/60, 30/80, 30/100 nm mixtures of Au NPs with the nominally equal number concentration of NPs in mixture are shown in Fig. 2.26c. As expected, the histograms for the mixtures are composed from the histogram of corresponding NPs. The discrepancy in the adsorption rates between smaller 30 nm and 40 nm Au NPs and larger NPs in mixtures may be explained

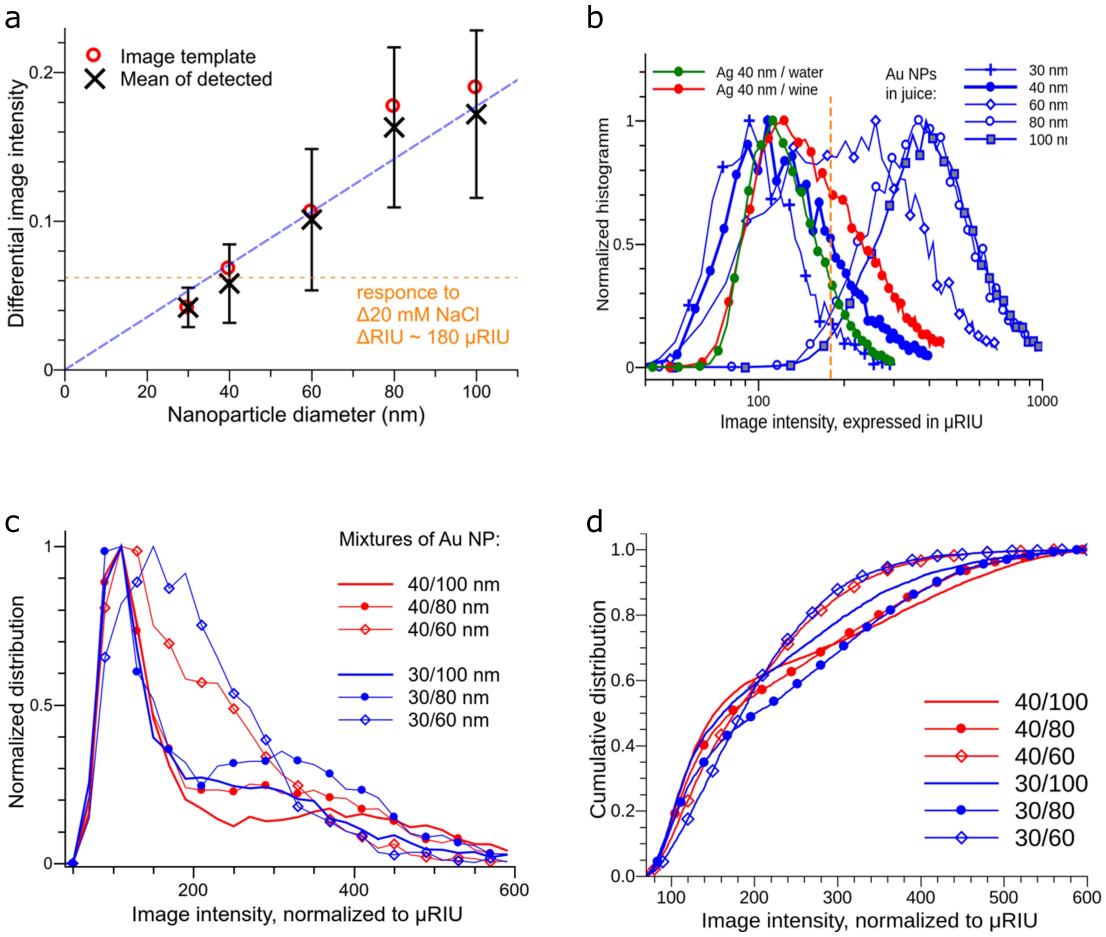

FIGURE 2.26: Characterization of size of nanoparticles in complex media. a) Image intensity of Au NPs of different size in apple juice. b) Histograms of image intensities of NPs normalized to the RI response. Ag 40 nm NP were measured separately in water and wine, Au NPs were measured in apple juice. c) Histograms of image intensities mixed suspensions of Au NPs. d) Cumulative histogram of image intensities. All the plots were normalized to RI units by calibration with 20 mM NaCl.

by two reasons. First, smaller NPs diffuse faster through the unstirred layer near the sensor surface. Thus it leads to a higher adsorption rate of smaller NPs at the same concentration in the volume. The second reason is that the narrower distribution of image intensities for smaller NPs makes the mode value of the histogram apparently higher. The number of NPs corresponding to the particular size population can be obtained by integration of the area under distribution curve. For the mixed suspensions consisting of 40/60, 40/100, 30/80 and 30/100 nm NPs, clear two-phase curves with the ratio of the components between 1:1 and 2:1 were obtained (Fig. 2.26d). The data demonstrate that the distribution of image intensities relates to the size distribution of nanoparticles. However, one cannot exclude also a contribution of other effects, such as thickness variations of the gold layer through the sensor surface, non-complete compensation of inhomogeneous light distribution during the calibration step, or an influence of impurities on the distance between adsorbed NPs and gold layer.

2.4.5 Conclusion

We have reported a new analytical technique based on combination of a wide field of view SPM with a specially developed data analysis including recognition and clusterization of optical images from NPs on the sensor surface. The wide field of view leads to a number of advantages. First, the high sensor surface increases a probability of adsorption of at least one NP on the sensor surface during measurement time thus providing a very high sensitivity of this analytical techniques. The reliable detection limit for 1 minute measurement time is better than 10^6 NPs/mL (~1.6 fM) or ~0.3 ppb and can be further improved by increasing of the measurement time or sensor surface. Secondly, it allows us to analyze hundreds thousands of NPs on the sensor surface simultaneously thus providing a high dynamic range and a possibility to get statistically representative measurements within a very short time. The wide field of view allows one to apply sensor array technology [29]; some examples of application of sensor arrays for detection of NPs will be presented elsewhere [30]. An implementation of image recognition into this analytical technique opens a way for its application in very complex media. We have demonstrated that it provides reliable analytical data in practically relevant media of different complexity, starting from relatively simple (tap water, mineral water) up to very complex ones (wines, juices, cosmetics). The proposed method can be applied to detect single NPs without sample pretreatment, making it superior to most other alternative techniques for sensitive analysis of NPs in such complex media [1, 2]. Notably, the developed technology provides not only a determination of number concentration of NPs, it gives also information on the size of NPs and on the size distribution. As the closest competitor in terms of analytical capabilities the Nanoparticle Tracking Analysis (NTA) may be considered [31]. However, the differences in underlying principles (detection of moving NP in bulk solution vs NP immobilized on the sensor due to adsorption from bulk) make these two technologies more complementary that competitive. The immobilization of NPs allows combining the surface plasmon microscopy with other in-situ analytical techniques – like electrochemical analysis [29]. The proposed method may be applied to study the interaction of NPs with their local nano-environment which changes their properties [32]. One can also expect further development of the reported technique by its combination with Raman spectroscopy, field-flow-fractionation and other analytical techniques.

Acknowledgement

The work was supported by FP7 EC Project Nanodetector (FP7-NMP-2011-SME-5, #280478). We are grateful to all project partners, especially to Dr. A. Zybin and A. Kuzmichev, for discussions and suggestions. An assistance of Dr. K. Tonder and Mr. J. Burkhardt is acknowledged. The authors are grateful to Professors Erik Bakker,

Michal Borkovec and Reinhard Niessner for constructive comments and fruitful suggestions during the discussion of this work.

References

[1] F. Babick, J. Mielke, W. Wohlleben, S. Weigel, and V. D. Hodoroaba, *How reliably can a material be classified as a nanomaterial? Available particle-sizing techniques at work*, vol. 18. Springer Netherlands, 2016.

[2] R. Peters, G. ten Dam, H. Bouwmeester, H. Helsper, G. Allmaier, F. vd Kammer, R. Ramsch, C. Solans, M. Tomaniová, J. Hajslova, and S. Weigel, "Identification and characterization of organic nanoparticles in food," *TrAC - Trends Anal. Chem.*, vol. 30, no. 1, pp. 100–112, 2011.

[3] S. A. Love, M. A. Maurer-Jones, J. W. Thompson, Y.-S. Lin, and C. L. Haynes, "Assessing Nanoparticle Toxicity," *Annu. Rev. Anal. Chem.*, vol. 5, no. 1, pp. 181–205, 2012.

[4] A. Yurt, G. G. Daaboul, J. H. Connor, B. B. Goldberg, and M. Selim Ünlü, "Single nanoparticle detectors for biological applications," *Nanoscale*, vol. 4, no. 3, p. 715, 2012.

[5] B. Rothenhausler and W. Knoll, "Surface plasmon microscopy," *Nature*, vol. 332, pp. 615–617, apr 1988.

[6] B. Huang, F. Yu, and R. N. Zare, "Surface Plasmon Resonance Imaging Using a High Numerical Aperture Microscope Objective," *Anal. Chem.*, vol. 79, no. 7, pp. 2979–2983, 2007.

[7] W. Wang and N. Tao, "Detection, counting, and imaging of single nanoparticles," *Anal. Chem.*, vol. 86, no. 1, pp. 2–14, 2014.

[8] A. Zybin, Y. A. Kuritsyn, E. L. Gurevich, V. Temchura, K. Überla, and K. Niemax, "Real-time detection of single immobilized nanoparticles by surface plasmon resonance imaging," *Plasmonics*, vol. 5, no. 1, pp. 31–35, 2010.

[9] I. Sidorenko, S. Nizamov, R. Hergenröder, A. Zybin, A. Kuzmichev, B. Kiwull, R. Niessner, and V. M. Mirsky, "Computer assisted detection and quantification of single adsorbing nanoparticles by differential surface plasmon microscopy," *Microchim. Acta*, vol. 183, no. 1, pp. 101–109, 2016.

[10] S. Nizamov, O. Kasian, and V. M. Mirsky, "Individual detection and electrochemically assisted identification of adsorbed nanoparticles by using surface plasmon microscopy," *Angew. Chemie - Int. Ed.*, vol. 55, pp. 1–6, 2016.

[11] R. B. M. Schasfoort and A. McWhirter, "SPR Instrumentation," *Handb. Surf. Plasmon Reson.*, pp. 35–80, 2008.

[12] J. Homola, "Surface plasmon resonance sensors for detection of chemical and biological species," *Chem. Rev.*, vol. 108, no. 2, pp. 462–493, 2008.

[13] R. Radke, S. Andra, O. Al-Kofahi, and B. Roysam, "Image change detection algorithms: a systematic survey," *Image Process. IEEE Trans.*, vol. 14, no. 3, pp. 294–307, 2005.

[14] S. Nizamov and V. M. Mirsky, "Self-referencing SPR-biosensors based on penetration difference of evanescent waves.," *Biosens. Bioelectron.*, vol. 28, pp. 263–269, oct 2011.

[15] V. Lozovski, "Visualization of nano-sized objects by scattering of surface plasmon polariton theoretical aspects of the problem," *J. Comput. Theor. Nanosci.*, vol. 9, no. 6, pp. 859–863, 2012.

[16] A. Demetriadou and A. Kornyshev, "Principles of nanoparticle imaging using surface plasmons," *New J. Phys.*, vol. 17, no. 1, p. 13041, 2015.

[17] A. Demetriadou, "The impact of natural modes in plasmonic imaging," *Sci. Rep.*, vol. 5, no. December, pp. 1–9, 2015.

[18] T. Son and D. Kim, "Theoretical approach to surface plasmon scattering microscopy for single nanoparticle detection in near infrared region," *Plasmon. Biol. Med. XII*, vol. 9340, pp. 93400W–93400W–6, 2015.

[19] F. Weichert, M. Gaspar, C. Timm, a. Zybin, E. L. Gurevich, M. Engel, H. Müller, and P. Marwedel, "Signal analysis and classification for surface plasmon assisted microscopy of nanoobjects," *Sensors Actuators, B Chem.*, vol. 151, no. 1, pp. 281–290, 2010.

[20] J. P. Lewis, "Fast Template Matching," *Vis. Interface 95*, vol. 10, no. 11, pp. 120–123, 1995.

[21] A. Weir, P. Westerhoff, L. Fabricius, K. Hristovski, and N. Von Goetz, "Titanium dioxide nanoparticles in food and personal care products," *Environ. Sci. Technol.*, vol. 46, no. 4, pp. 2242–2250, 2012.

[22] C. Contado and A. Pagnoni, "TiO2 in commercial sunscreen lotion: Flow field-flow fractionation and ICP-AES together for size analysis," *Anal. Chem.*, vol. 80, no. 19, pp. 7594–7608, 2008.

[23] S. R. Raz, M. Leontaridou, M. G. E. G. Bremer, R. Peters, and S. Weigel, "Development of surface plasmon resonance-based sensor for detection of silver nanoparticles in food and the environment," *Anal. Bioanal. Chem.*, vol. 403, no. 10, pp. 2843–2850, 2012.

[24] S. Chernousova and M. Epple, "Silver as antibacterial agent: Ion, nanoparticle, and metal," *Angew. Chemie - Int. Ed.*, vol. 52, no. 6, pp. 1636–1653, 2013.

[25] S. Yanniotis, G. Kotseridis, A. Orfanidou, and A. Petraki, "Effect of ethanol, dry extract and glycerol on the viscosity of wine," *J. Food Eng.*, vol. 81, no. 2, pp. 399–403, 2007.

[26] R. A. Sperling, P. G. Rivera, F. Zhang, M. Zanella, and W. J. Parak, "Biological applications of gold nanoparticles," *Chem. Soc. Rev.*, vol. 37, no. 9, pp. 1909–30, 2008.

[27] M. Wang, B. Duong, H. Fenniri, and M. Su, "Nanomaterial-based barcodes," *Nanoscale*, vol. 7, no. 26, pp. 11240–11247, 2015.

[28] "Concentrative properties of aqueous solutions: density, refractive index, freezing point depression, and viscosity," in *CRC Handb. Chem. Phys.*, pp. 8–71, CRC Press, 87 ed., 2006.

[29] S. Nizamov, V. Scherbahn, and V. M. Mirsky, "Self-referencing SPR-sensor based on integral measurements of light intensity reflected by arbitrarily distributed sensing and referencing spots," *Sensors Actuators B Chem.*, vol. 207, pp. 740–747, 2015.

[30] V. Scherbahn, S. Nizamov, and V. M. Mirsky, "Plasmonic detection and visualization of directed adsorption of charged single nanoparticles to patterned surfaces," *Microchim. Acta*, vol. 183, no. 11, pp. 2837–2845, 2016.

[31] V. Filipe, A. Hawe, and W. Jiskoot, "Critical evaluation of nanoparticle tracking analysis (NTA) by NanoSight for the measurement of nanoparticles and protein aggregates," *Pharm. Res.*, vol. 27, no. 5, pp. 796–810, 2010.

[32] X. Wo, Y. Luo, N. Tao, W. Wang, and H. Y. Chen, "Measuring the number concentration of arbitrarily-shaped gold nanoparticles with surface plasmon resonance microscopy," *Sci. China Chem.*, vol. 59, no. 7, pp. 843–847, 2016.

Supporting information

The Supporting Information (video data on adsorption of 40 nm Ag-NPs from concentrations 10^6, 10^7, and 10^8 NPs per mL, file Video1.mp4) is available free of charge on the ACS Publications website:

DOI:10.1021/acs.analchem.6b02878

as well as on the CD attached to this dissertation.

2.5 Plasmonic detection and visualization of single enzymatically synthesized nanoparticles by means of wide-field surface plasmon resonance microscopy

SCHERBAHN, V., NIZAMOV, S., & MIRSKY, V. M.

In preparation.

2.5.1 Abstract

Recently, wide-field surface plasmon resonance microscopy (WF-SPRM) was shown to detect, to visualize, to localize and to quantify single engineered nanoparticles adsorbed to the sensor surface. Besides a typical chemical synthesis, researchers have reported on application of enzymes to mediate synthesis of metallic nanoparticles for biosensing and bioelectronic applications. Several enzymes have been reported to be suitable for this purpose. In this work, we report on application of alkaline phosphatase (ALP) to mediate synthesis of gold nanoparticles (Au NPs) followed by their detection in real-time by means of WF-SPRM. The enzyme-mediated synthesis of Au NPs undergoes the following pathway: ALP converts the de-phosphorylation of the phosphorylated ascorbic (AA-P) acid to ascorbic acid (AA) and phosphate followed by reduction of gold ions (Au^{3+}) to Au NPs by AA. Applying WF-SPRM as main detecting technology it was possible to detect enzymatically formed NPs by ALP both unbound in solution and immobilized as an enzyme-antibody-conjugate to the sensor surface. This approach represents an important milestone towards development of ultra-sensitive biosensing applications as each single adsorbed, newly synthesized nanoparticle undergoes detection by WF-SPRM.

2.5.2 Introduction

As they exhibit unique physico-chemical properties, nanoparticles are nowadays considered as indispensable tools in the development of biosensing and diagnostic applications [1–4]. Unlike to be chemically synthesized [5, 6], nanoparticles were shown to be also synthesized by enzymes [7–10]. Recently, an ultra-sensitive plasmonic technology – wide-field surface plasmon resonance microscopy (WF-SPRM) – was developed enabling adsorption of single nanoparticles of different materials and sizes to differently modified surfaces to be detected, visualized and characterized within few minutes [11–18]. The visualization of nanoparticles by WF-SPRM mainly relies on the detection of scattered surface plasmon waves [19]. Mainly these encouraging aspects served as a base to apply the WF-SPRM technology to detect adsorption of single enzymatically synthesized nanoparticles. In order to implement this approach, it is necessary to understand which reaction type the nanoparticle formation obeys, and which enzymatic systems catalyze such a reaction. Concerning the latter aspect, two

pathways are possible: either direct formation of nanoparticles from a precursor by the enzyme, or the enzyme is applied to first produce a compound that in the next step induces a chemical reaction with the precursor to form nanoparticles. In regard to formation of metallic nanoparticles, which exhibit the most appropriate plasmonic properties to be detected by WF-SPRM, pure α-amylase was shown to catalyzes a direct reduction of gold ions to nanoparticles [20]. However, this reaction is governed by very slow kinetics (> 48 hours) and thus reveals to be not reliable for our purpose. Therefore, the application of redox-active compounds to reduce metal ions (precursor) to metal atoms (nanoparticles) represents another possible way. In this particular case, the role of the enzyme is attributed to act as a mediator to produce a compound with redox properties which in turn induces reduction of metal ions to nanoparticles. Hydrogen peroxide (H_2O_2) is known to act as a reducing agent to form gold nanoparticles [21, 22]. One of the most studied and applied enzymes – glucose oxidase (GOD) [23] – has been studied to mediate synthesis, mainly the growth, of metallic nanoparticles as glucose conversion is inherently accompanied by production of H_2O_2. In this case, two reactions take place: oxidation of the glucose resulting in formation of H_2O_2 as side product and reduction of gold ions by H_2O_2 to gold nanoparticles. It is to note, that the generated H_2O_2 can already serve as measurable signal [24]; however, the most important advantage of this approach relies on the possibility to detect nanoparticles by naked eye as without any further technical equipment as they exhibit different plasmonic properties (color) in dependence on their size and shape. This approach has been successfully implemented using a N-Morpholinoethansulfonic acid (MES) buffer as a mild pre-catalyst in combination with H_2O_2 as the main catalyst [21].

Besides H_2O_2 as reducing agent at alkalic pH, organic aromatic compounds such as ascorbic acid (AA) [25, 26] or phenolic derivatives [27, 28] were also shown to reduce metal ions to nanoparticles. In this particular case it is necessary first, to provide an inactivated form of the reducing agent (detaining the redox activity) and secondly, to choose an enzymatic system that catalyzes the activation of this compound to reduce metal ions. Exemplarily, redox-active ascorbic acid was shown to form gold- (Au-) [29] and silver nanoparticles (Ag NPs) [30–32]. Fortunately, ascorbic acid is also available in an inactivated state – phosphorylated ascorbic acid (AA-P). This aspect encouraged researchers to develop biosensors based on application of alkaline phosphatase (ALP) to catalyze hydrolysis (activation) of redox-inactive phosphorylated ascorbic acid to redox-active ascorbic acid followed by reduction of silver ions by ascorbic acid to form Ag NPs [30–32]. In that particular case, first a hydrolysis (activation) of the inactive phosphorylated ascorbic acid to ascorbic acid and phosphate takes place, whereas in the second reaction ascorbic acid reduces silver ions to form nanoparticles. Notably, this reaction has to be performed in the dark to prevent spontaneous formation of silver nanoparticles. Additionally, the formed silver nanoparticles can undergo a spontaneous oxidation/dissolution [18]. Besides, the presence of chloride ions in the buffer solution may lead to the formation of an insoluble silver chloride salt (AgCl).

Apart from enzymatic formation of solid nanoparticles, application of gas-producing enzymes may be applied to generate gaseous bubbles or even nano-bubbles to be detected by means of WF-SPRM. Catalase (CAT) is one of the most produced natural enzymes and catalyzes decomposition of H_2O_2 to water and oxygen (O_2) [33, 34]. Using CAT, a direct formation of gaseous O_2 on the sensor surface followed by its detection by WF-SPRM is possible.

In this work, we report a novel approach to detect and visualize enzyme-assisted generation of single gold nanoparticles (Au NPs) using wide-field surface plasmon resonance microscopy (WF-SPRM) as the main detecting technology. After evaluating GOD and CAT as potential enzyme mediators, alkaline phosphatase (ALP) was chosen as the most suitable biocatalyst to convert the redox-inactive phosphorylated ascorbic acid (AA-P) into the redox-active ascorbic acid (AA) that in turn induces a reduction of gold (Au^{3+}) ions to Au^0-agglomerates thus forming gold nanoparticles (Au NPs). ALP is used and tested both in free, unbound state (in volume) and immobilized to the sensor surface.

2.5.3 Materials and methods

2.5.3.1 Chemicals

11-Mercaptoundecanoic acid (HS-$(CH_2)_{10}$-COOH) was purchased from Sigma Aldrich. 2-(N-mor-pholino)ethanesulfonic acid (MES) was purchased from Roth. Diethanolamine (DEA), glycine, L-Ascorbic acid (AA), L-ascorbic 2-phosphate sesquimagnesium salt hydrate (AA-P), chloroauric acid ($HAuCl_4$) were purchased from Sigma as well as alkaline phosphatase (bovine intestinal mucosa), human serum albumin, polyclonal anti-human serum albumin antibody (rabbit anti-HSA IgG), 20 nm and 100 nm gold nanoparticles (Au NPs). Tris(hydroxymethyl)aminomethane (TRIS), Zink chloride ($ZnCl_2$) and magnesium chloride ($MgCl_2$) were purchased from Merck. 99.9 % ethanol and phosphate salts were purchased from Merck. Dimethyl sulfoxide (DMSO) and sodiumchloride (NaCl) were purchased from Roth. Goat anti-rabbit IgG-ALP (secondary/detecting antibody) was purchased from Invitrogen. Alkaline phosphatase (ALP), Catalase (CAT) and glucose oxidase (GOD) were purchased by Sigma Aldrich.

2.5.3.2 Colorimetric test

The feasibility of reducing Au^{3+} ions ($HAuCl_4$ as source) by ascorbic acid (AA) was performed as follows: 100 μl containing 2 mM $HAuCl_4$, 1 mM $MgCl_2$ and 1 μM $ZnCl_2$ were added to 100 μl containing 2mM AA, 1 mM $MgCl_2$, and 1 μM $ZnCl_2$ and incubated for maximal 30 minutes (1 mM final concentrations of AA and $HAuCl_4$). Negative controls without ALP or anti-rabbit IgG-ALP were performed by addition of 100 μl containing 0.025 mM, 0.2 mM or 2 mM $HAuCl_4$, 1 mM $MgCl_2$ and 1 μM $ZnCl_2$, respectively, to 100 μl containing 0.025 mM, 0.2 mM or 2mM AA-P, 1 mM $MgCl_2$, and 1 μM $ZnCl_2$, respectively, and incubated for maximal 30 minutes (0.0125 mM, 0.1 mM

or 1 mM final concentrations of AA-P and $HAuCl_4$). Positive control with ALP or anti-rabbit IgG-ALP was conducted as in previous step but with extraction of 0.5 μl from each batch followed by addition of either 0.5 μl ALP (original solution was stored at 4 $^\circ$ C, 12 mg ml^{-1} with ~ 43 kU ml^{-1}) or 0.5 μl anti-rabbit IgG-ALP (stored as aliquots with 1–5 μl at -20 $^\circ$ C , 1 mg ml^{-1}) and incubated for maximal 30 minutes. As buffers, DEA, TRIS or glycine were used at pH 9–9.5 with final concentration ranging from 10 mM to 100 mM. All solutions were filtered by a 0.22 μm cellulose acetate filter.

2.5.3.3 Characterization of ALP-generated Au NPs by optical methods

Spectrophotometric measurements were performed using the Spectrophotometers Jasco V-630 and Thermo Scientific Evolution 220 measuring 1:10 sample dilutions obtained within the colorimetric test. Measurements of size of ALP-generated NPs were performed using dynamic light scattering (DLS, Zeta Sizer, Malvern) and nanoparticle tracking analysis (NTA, NanoSight, Malvern).

2.5.3.4 Functionalization of sensor surface

Prior functionalization, gold coated prisms were cleaned by freshly prepared piranha solution (1:3 v: v mixture of 32 % H_2O_2/H_2SO_4) for ~ 20 s followed by thorough, subsequent rinsing with water and ethanol, and dried at room temperature. *Caution: piranha solution reacts violently with most organic materials and must be handled with extreme care.* In the next step, cleaned prisms were put in 1 mM ethanolic solution of 11-Mercaptoundecanoic acid (HS-$(CH_2)_{10}$-COOH) and incubated overnight at room temperature. Before usage, the prisms were rinsed thoroughly by ethanol and dried at room temperature.

2.5.3.5 Immobilization of ALP-conjugated antibody

Sensor prisms, previously modified by HS-$(CH_2)_{10}$-COOH, were coated with anti-HSA-IgG by addition of 50 μl of 0.3 mg ml^{-1} anti-HSA-IgG containing 400 mM EDC in 0.1 M MES buffer pH 5.5 to the sensor surface for 10 minutes as one-pot-reaction. After a thorough washing step by phosphate saline buffer (PBS) pH 7.35, 50 μl with 0.1 mg ml^{-1} ALP-conjugated secondary(detecting) antibody (anti-rabbit IgG-ALP) directed against rabbit anti-HSA IgG were added. After 1 hour; the sensor was washed by PBS and stored until usage (in all cases the further usage occurred 10–15 min later).

2.5.3.6 Measurements by wide-field surface plasmon resonance microscopy (WF-SPRM)

The setup for WF-SPRM is described elsewhere [11, 14, 16]. In brief, a *p*-polarized 642 nm laser beam illuminates a ~ 50 nm gold layer through a glass prism ($n = 1.7$) at the angle of the total internal reflection near resonance conditions forming a so-called

evanescent wave. Smallest changes in refractive index within the penetration depth of evanescent wave strongly affect the resonance conditions and can be detected by a camera.

It is to emphasize that all experiments using WF-SPRM were performed in batch-mode with a horizontal sensor position (applying a 100 μl droplet to the sensor surface). Concerning experiments with ALP unbound in solution, following additions onto the sensor surface were given while gathering SPRM-images online: (1) 50 μl containing 2 mM $HAuCl_4$, 1 mM $MgCl_2$, 1 μM $ZnCl_2$; (2) after ~300 frames (~5 minutes) 50 μl containing 2 mM AA-P, 1 mM $MgCl_2$, 1 μM $ZnCl_2$; (3) ~300 more frames later 0.5 μl 1 mg ml^{-1} ALP were added. For experiments with immobilized anti-rabbit IgG-ALP, only steps (1) and (2) were performed.

2.5.4 Results and discussion

2.5.4.1 Potential enzymatic systems to generate nanoparticles

To reduce metal ions, only few enzymes were reported to perform this reaction [20]. However, due to very slow kinetics of nanoparticle formation (> 48 hours) we exclude these enzymatic systems. Therefore, instead to apply a "slow" enzyme to directly reduce metal ions, reducing organic compounds allowing a much faster reduction rate were suggested. Prior, several aspects have to be taken into account: (1) an appropriate compound to reduce metal ions to metal atoms further forming nanoparticles; (2) appropriate conditions to maintain enzyme activity (pH, buffer compositions) and to ensure reduction of metal ions; (3) availability and chemical stability of the appropriate reducing compound in an inactivated state (e.g. capped or as a precursor); (4) suitable enzymatic system to convert either the redox-inactive compound or the precursor into an active redox agent. It is important to mention that before choosing ALP as an enzyme mediator, first well-known enzymatic systems like glucose oxidase (GOD) and catalase (CAT) were evaluated.

Hydrogen peroxide (H_2O_2) is known as reducing agent to form metallic nanoparticles [7, 21]. As H_2O_2 is intrinsically produced as a by-product when glucose is oxidized by GOD, it is logical to suggest this enzyme to form Au NPs in the presence of gold (Au^{3+}) ions. Colorimetric experiments confirmed the feasibility of this reaction (Supplementary, Fig. 2.32). Since several organic buffers are known to spontaneously induce formation of Au-agglomerates in the presence of Au^{3+} ions and glucose [35], phosphate buffer was preferred. Negative controls (without GOD and H_2O_2 in the presence of Au^{3+} ($HAuCl_4$) and glucose only), showed no color formation and thus indicating glucose not to affect formation of Au NPs without GOD (Supplementary, Fig. 2.33). Similar results were obtained with an additional negative control: GOD and $HAuCl_4$ without glucose (Fig. 2.27a). Once different GOD concentrations (1 mg ml^{-1}, 0.1 mg ml^{-1}, 0.01 mg ml^{-1}) were added into samples containing glucose and $HAuCl_4$, the sample color turned blue/purple and pink (0.1 mg ml^{-1} and 0.01 mg ml^{-1} GOD,

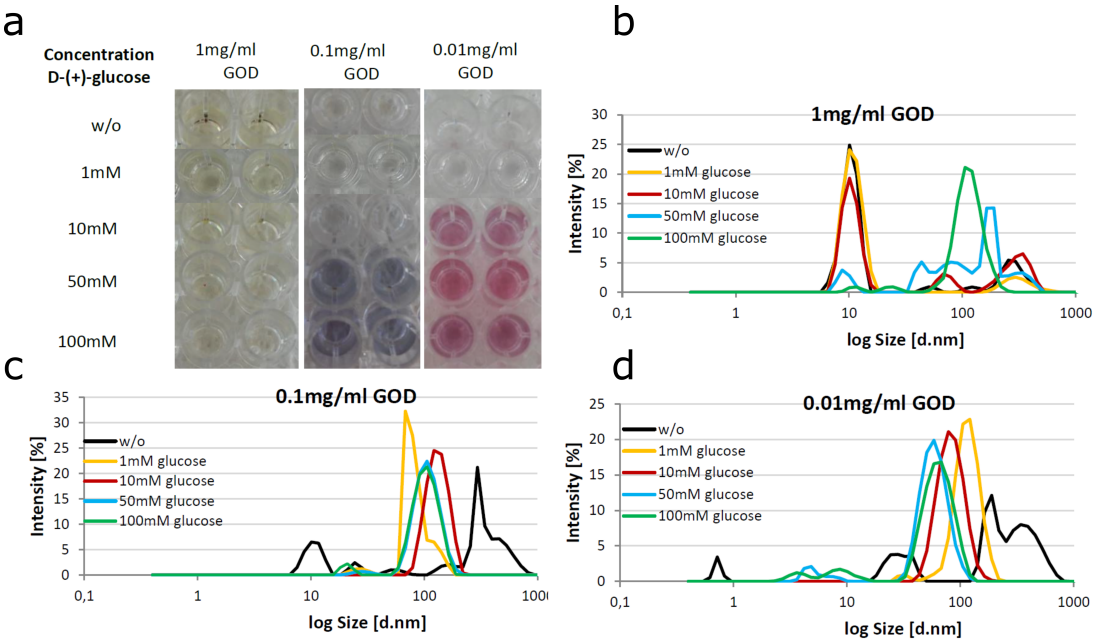

FIGURE 2.27: (a) Colorimetric test applying different concentrations of GOD and glucose. DLS measurements of samples containing (b) 1 mg ml^{-1} GOD, (c) 0.1 mg ml^{-1} GOD and (d) 0.01 mg ml^{-1} GOD

respectively) after ~15 min, whereas no color change was observed when using 1 mg ml^{-1} GOD (Fig. 2.27a). Assuming that lower GOD concentration inherently leads to generation of lower amount of H_2O_2 per time, it can be considered that under such conditions smaller Au NPs (Fig. 2.27d) are formed exhibiting pink color (Fig. 2.27a) compared to larger Au NPs ((Fig. 2.27c)) exhibiting blue/purple color (Fig. 2.27a) when using a higher GOD concentration (0.1 mg ml^{-1}). However, an opposite effect of H_2O_2 concentration on size of generated Au NPs was shown in [21]. As for our purposes, formation of NPs within first minute(s) is required and the GOD system was shown to form Au NPs only after 10–15 min, this system is considered to be too "slow" and was discarded.

An alternative to synthesizing solid nanoparticles, enzymatic formation of gases may be a promising issue to apply gaseous bubbles or even nano-bubbles to be detected by WF-SPRM. Thus, the choice of a fast enzymatic system to generate a gas was made in favor of catalase, which, along with acetylcholine esterase [36], represents one of the fastest natural enzymes in nature with a turnover rate in the range of several millions molecules per second [37]. Catalase is a ubiquitous enzyme which is produced in almost all living organisms exposed to oxygen catalyzing the decomposition of hydrogen peroxide (H_2O_2) to oxygen (O_2) and water (H_2O). The refractive index of gaseous O_2 is ~1; compared to the refractive index of water (n ~1.334). Due to such an essential difference in refractive index, a possible formation of O_2 bubbles, or even nano-bubbles, on the sensor surface could be visualized by WF-SPRM. Therefore, visualization of surface nano- or micro-bubbles may be potentially applied to

develop novel biosensing approaches. First experiments showed a successful immobilization of catalase measured by means of classical surface plasmon resonance (SPR) (Fig. 2.28a). The formation of bubbles in the presence of H_2O_2 was visualized using the WF-SPRM technology. As can be seen in Fig. 2.28b, signals, most likely attributed to O_2-formation on sensor surface, were successfully detected (denoted by yellow circles). Unlike the large spot in the bottom left corner, white and black spots are visible throughout the horizontally placed sensor indicating formation of O_2-bubbles accompanied by their detachment from the surface into the bulk (black spots, opposite signal to white). Despite successful detection of O_2 bubbles formed, almost all experiments with immobilized catalase and H_2O_2 solutions were accompanied by accidental accumulation of macroscopic O_2 bubbles on the sensor surface and in the flow-cell, thus disturbing measurement earlier or later. Additionally, formation of O_2-bubbles occurred at relatively high H_2O_2 concentrations (> 0.1 M); sometimes spurious decomposition of H_2O_2 could be observed as well. Therefore, this enzymatic system was not considered to be further investigated. Nevertheless, the results showed for the first time by means of WF-SPRM the visualization of gaseous O_2 bubbles to be formed by immobilized catalase in the presence of H_2O_2 in solution. Perhaps, this approach may potentially work with other enzyme systems producing gaseous products [37].

After discarding GOD- and CAT -based enzymatic systems, taking into account considerations and prerequisites for enzyme mediated synthesis of NPs, a feasible, robust and fast enzyme-mediated generation of Au NPs was realized using ALP and phosphorylated ascorbic acid (AA-P) as redox-inactive compound. Recent works report on ALP to catalyze the de-phosphorylation of phosphorylated ascorbic acid (AA-P) to the redox-active ascorbic acid (AA) to reduce silver ions (Ag^+) to silver nanoparticles (Ag NPs) followed by electrochemical readout [31, 38, 39].

However, this reaction must be strictly conducted in the absence of light to prevent spontaneous formation of silver agglomerates leading to false-positive signals. We also confirm ALP to be able to mediate synthesis of Ag NPs; however, as WF-SPRM implies illumination of sensor surface by red laser light (642 nm), spontaneous formation of Ag NPs (false-positives) in the presence of Ag^+ was observed. Therefore, we excluded the system using Ag^+ as metal-ion-precursor. Besides reduction of Ag^+ to Ag NPs, AA is also known to reduce Au^{3+} ions to generate gold nanoparticles (Au NPs) and gold microparticles (Au MPs) [25, 26]. Assuming these prerequisites, ALP was chosen as biocatalyst to perform the de-phosphorylation of AA-P to AA to reduce Au^{3+} ions to Au NPs. A simplified reaction path to generate Au NPs using ALP and AA-P in the presence of Au^{3+} is given in Eq. 2.9:

$$AA\text{-}P + Au_{ox}^{3+} \overset{ALP}{\rightarrow} AA_{red} + P + Au_{ox}^{3+} \rightarrow AA_{ox} + P + Au_{red}^{0}(AuNPs) \downarrow \qquad (2.9)$$

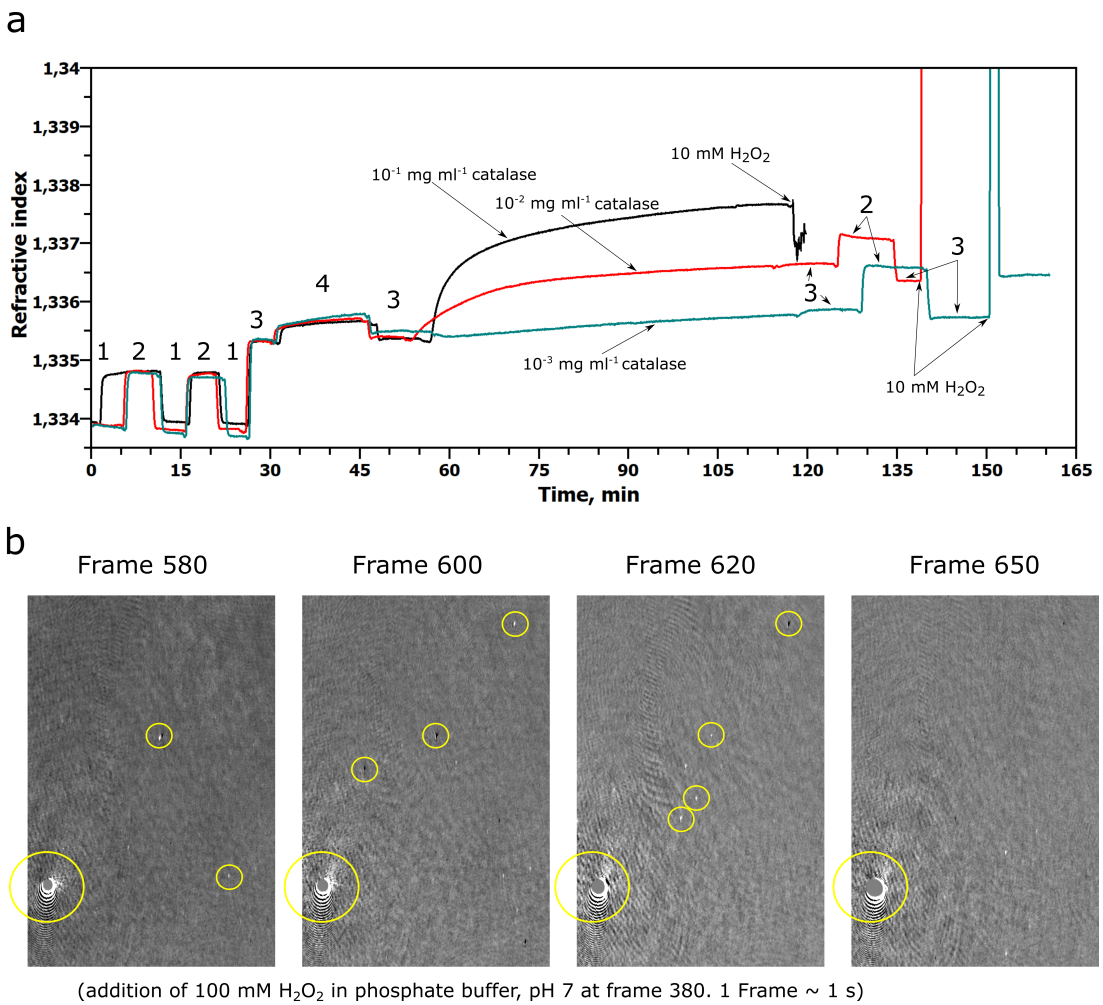

FIGURE 2.28: (a) SPR-sensograms representing immobilization of catalase using different concentrations in phosphate buffer at pH 7 followed by addition of 10 mM H_2O_2. 1 – water; 2 – 100 mM NaCl; 3 – 1 x PBS buffer pH 7.3; 4 – 100 mM 1-ethyl-3-(-3-dimethylaminopropyl) carbodiimide hydrochloride (EDC) and 25 mM N-hydroxysuccinimide (NHS) as linking agents in 1 x PBS buffer pH 7.3; 5 – 50 mM ethanolamine (blocking agent) in 1 x PBS buffer pH 7.3 (b) SPRM-images visualizing formed nano- and microbubbles by immobilized catalase. Catalase covalently coupled to the sensor surface according to procedure in (a).

2.5.4.2 Free ALP mediated synthesis of gold nanoparticles and their characterization

First, three working buffer systems for maintaining pH in the 9–11 range (being the working pH range for ALP [40]) were tested. Additionally, substrate (AA-P and $HAuCl_4$) concentrations were evaluated resulting in 1 mM for both as the most appropriate and effective concentrations which exhibit the fastest formation of Au NPs in the presence of ALP. The selected three basic buffer systems are glycine, Tris(hydroxymethyl)aminomethan (TRIS), and diethanolamine (DEA). The performance of ALP in these particular media as well as their impact on the kinetics of Au NPs formation was tested using a simple colorimetric approach (Fig. 2.29a). As a prerequisite, the

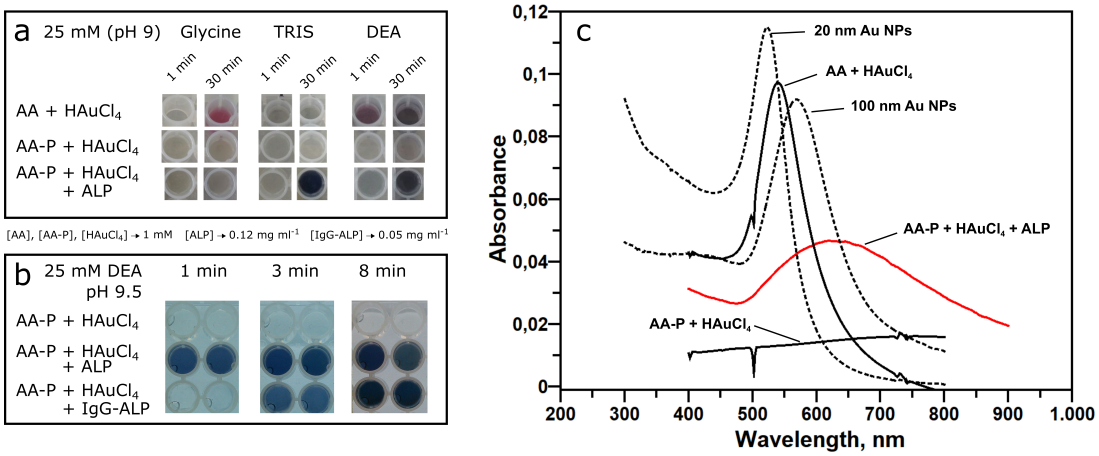

FIGURE 2.29: Colorimetric tests (a),(b) . Experimental conditions are given on the figure. All samples contain 1mM $MgCl_2$ and 0.1 mM $ZnCl_2$ as stabilizing agents for ALP. (c) Spectrophotometric measurements of solutions containing commercially available 20 and 100 nm gold nanoparticles (dashed lines); ascorbic acid (AA) + $HAuCl_4$ (Au^{3+}); phosphorylated ascorbic acid (AA-P) + $HAuCl_4$ (Au^{3+}); phosphorylated ascorbic acid (AA-P) + $HAuCl_4$ (Au^{3+}) + 0.12 mg ml^{-1} alkaline phosphatase (ALP) (red solid line). The last two solutions additionally contain 1 mM $MgCl_2$ and 0.1 mM $ZnCl_2$.

ability of AA to reduce Au^{3+} ions to Au NPs in alkalic conditions was tested. In the DEA buffer system, a colorless solution turns blue/purple immediately, this can be observed with the naked eye. In glycine buffer the solution turned pink/red within 10–15 min (from colorless to pink/red) whereas no color change in TRIS buffer was observed with the naked eye even after 30 min. Based on these results, DEA buffer seems to be the most suitable one as the formation of NPs occurs within the first minute compared to glycine and TRIS. According to preliminary experimental work (Supplementary, Fig. 2.34), the working concentration concerning the DEA buffer, AA-P and $HAuCl_4$ were defined with 25 mM, 1 mM and 1 mM, respectively. Negative controls were performed with mixtures containing AA-P and $HAuCl_4$ (Au^{3+}) to ensure that AA-P itself (i.e. without being decomposed to AA and P) cannot reduce Au^{3+} to Au NPs. As expected, no color change in either buffer system was observed indicating that AA-P persists in a redox-inactive form (Fig. 2.29a) and no NPs can be formed by it directly. Finally, the positive control was performed by addition of ALP into the buffer solutions containing AA-P and Au^{3+} ions (Fig. 2.29a). Either buffer system showed color formation at different time after enzyme addition. Similar to the case with pure AA, the most efficient reaction was observed in the DEA buffer where a color change from colorless to blue/purple was observed within the first minute by naked eye. The intensity of the sample color increased with time indicating an increase in the concentration of formed NPs. Similar behavior was observed using TRIS buffer in which the color change occurred 10–15 min after ALP addition indicating much slower kinetics compared to DEA. No color change in the glycine buffer was observed 30 min after

ALP addition, thus indicating very slow reaction kinetics. Based on these results, DEA buffer demonstrated the highest suitability in regard to the kinetic of ALP-assisted generation of Au NPs. Thus, it was considered to be applied for further experimental work. Besides in free state, ALP was applied as a conjugate to an antibody (anti-rabbit IgG-ALP) and showed similar ability to perform successful synthesis of Au NPs in the presence of Au^{3+} and AA-P in solution (Fig. 2.29b). Additionally, spectrophotometric measurements of the suspensions presented in Fig. 2.29a were performed (Fig. 2.29c). For the comparison, UV-visible spectra of commercially available 20 nm and 100 nm Au NPs were included. As can be seen, the sample with Au NPs generated by AA and Au^{3+} showed an absorption maximum of 540 nm indicating a size of ~ 40–50 nm. The control measurement in the presence of AA-P and Au^{3+} without ALP showed no absorption peak thus confirming formation of Au NPs being strongly dependent on ALP. Only after addition of ALP, an absorption peak with a maximum at ~ 625 nm was measured indicating formation of Au NPs.

However, this absorption maximum does not correspond to spherical particles with a size of 70–100 nm, as measured by nanoparticle tracking analysis (NTA) (Supplementary, Fig. 2.35): typical absorption maximum corresponding to such a size range is measured between 550 and 565 nm according to the model based on Mie theory [41]. Besides AA acting as a stabilizer, such a discrepancy can be explained by the absence of the any kind of additional stabilization resulting in a continuing growth of NPs, thus leading to the aggregation of NPs or their growth into the submicron scale.

After demonstrating ALP to mediate formation and growth of Au NPs, this enzymatic pathway was studied using WF-SPRM. It is to mention that the shape of the NPs with a relatively small aspect ratio (i.e. excluding nanowires, long nanorods, platelets) does not affect the measurement, identification and quantification of NPs using the WF-SPRM technology. The first attempt including negative and positive controls was performed in the volume in batch (Fig. 2.30). To ensure Au NPs do not form without ALP, a solution containing AA-P and Au^{3+} was incubated for 15 minutes in batch on the sensor surface while gathering differential SPRM-images. As can be seen, a very low, negligible amount of NPs was detected/counted ((Fig. 2.30b)) while no signal due to adsorption of Au NPs were recognizable (Fig. 2.30b inset). Such background signal accompanies the measurements throughout the entire study and is at least partially attributed to the false positives registered by the detection software: spurious noise may be falsely identified as very small particles. Once the ALP was added (after ~ 15 min) into the droplet, single, distinct white spots appeared ~ 2 min later on the gathered differential SPRM-images, thus clearly indicating formation and adsorption of Au NPs (Fig. 2.30b-c). This result strongly confirms WF-SPRM to be a suitable technology to detect single NPs formed by an enzyme-mediated reaction. To our knowledge, this is demonstrated for the first time.

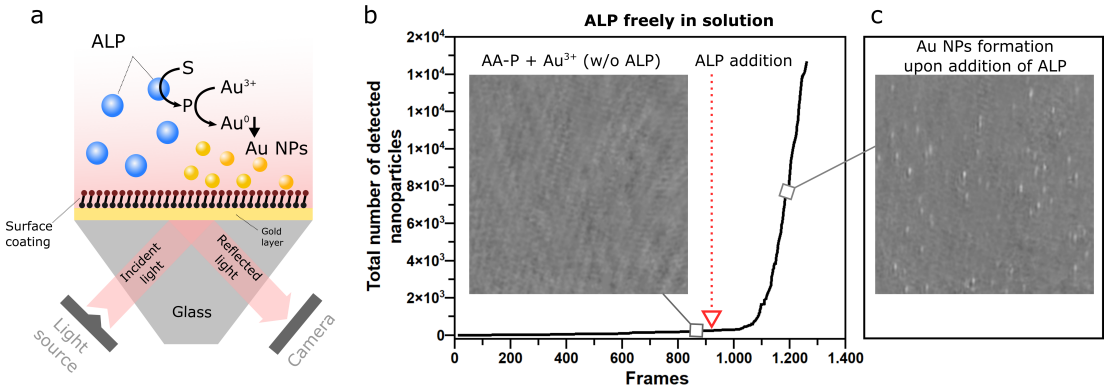

FIGURE 2.30: (a) Schematically presented synthesis of gold nanoparticles (Au NPs) by alkaline phosphatase (ALP) in solution applying WF-SPRM as detecting technique. "S" – substrate (phosphorylated ascorbic acid (AA-P)); "P" – product (ascorbic acid (AA)). (b) Detection of ALP-generated Au NPs by means of WF-SPRM and afterwards quantified by custom-made image post-processing approach [14]; (inset) typical WF-SPRM image showing no nanoparticle formation in the absence of ALP; frame rate ~1 frame s^{-1}. (c) WF-SPRM image visualizing single Au NPs formed by ALP.

2.5.4.3 Formation and detection of gold nanoparticles by immobilized ALP

In order to immobilize ALP to the sensor surface, a classical affinity binding was implemented. For that purpose, ALP was applied as a conjugate to a secondary antibody (anti-rabbit IgG-ALP). To confirm the anti-rabbit IgG-ALP is able to convert AA-P, first a colorimetric test was performed with anti-rabbit IgG-ALP in solution (Fig. 2.29b). As can be seen, in the presence of the anti-rabbit IgG-ALP a specific color change was observed by naked eye thus clearly indicating Au NPs were formed. This result is similar to that applying free ALP and confirms the ability of conjugated ALP to mediate nanoparticle formation.

The immobilization of ALP onto the sensor surface was performed using a commercially available anti-rabbit IgG-ALP. First rabbit-anti-human serum albumin IgG (rabbit anti-HSA IgG) was covalently immobilized to the sensor surface followed by addition of anti-rabbit IgG-ALP. The immobilization procedure was performed separately – outside the measurement setup. Formation of Au NPs was measured by WF-SPRM upon simultaneous addition of AA-P and Au^{3+} (substrates). As can be seen in Fig. 2.31b during the first 4 min after substrate addition, the conversion of AA-P was presumably catalyzed but no NPs were formed/detected (Fig. 2.31b inset). After that time delay, Au NPs were formed and their adsorption to the sensor surface was detected as white spots in differential SPRM images (Fig. 2.31c). It is to note that in spite of immobilized enzyme, NPs do not grow on the surface: they are first formed in the volume and afterwards adsorb to the sensor surface. In case Au NPs were formed directly on the surface, the signal generated in the SPRM images (white distinct spots) would persist during the growth phase of each distinct nanoparticle. However, in our case, NPs only appear for few seconds indicating their adsorption after diffusion from

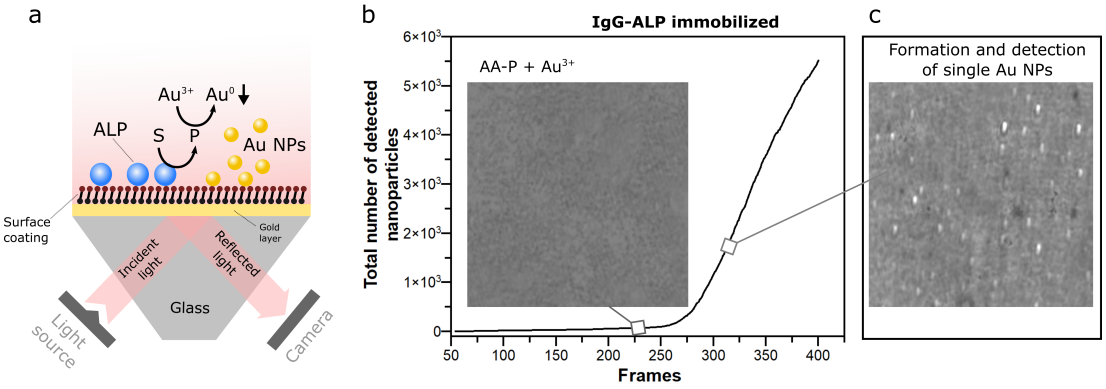

FIGURE 2.31: (a) Schematically presented synthesis of gold nanoparticles (Au NPs) by alkaline phosphatase (ALP) immobilized to the sensor surface. Detection of nanoparticles was performed by WF-SPRM. (b) Detection of ALP-generated Au NPs by means of WF-SPRM and afterwards quantified by custom-made image post-processing approach [14]; (inset) typical WF-SPRM image showing no nanoparticle formation; frame rate ~1 frame s^{-1}. (c) WF-SPRM image visualizing single Au NPs formed by immobilized ALP.

the volume phase to the sensor surface.

2.5.5 Conclusion

This work presents a comparative study of several enzymes to mediate synthesis of nanoparticles followed by their detection by means of WF-SPRM for future applications in bioanalytics. First, glucose oxidase- and catalase-based formation of nanoparticles has been evaluated. The idea behind the application of catalase is based on oxygen formation and a possible visualization of oxygen (nano)bubbles by WF-SPRM. The synthesis of gold nanoparticles has been investigated by glucose oxidase and alkaline phosphatase by naked-eye colorimetric and spectrophotometric detection as well as by dynamic light scattering and nanoparticle tracking analysis. Alkaline phosphatase revealed to be the most suitable enzyme to mediate synthesis of gold nanoparticles. The formed nanoparticles were successfully detected, visualized and quantified by means of WF-SPRM. Alkaline phosphatase was applied in different states: unbound in solution and bound to the sensor surface. The WF-SPRM technology was shown for the first time to detect single nanoparticles formed by enzymatic assistance. This approach opens versatile possibilities to develop novel biosensing platforms.

References

[1] O. V. Salata, "Application of nanoparticles in biology and medicine," *J Nanobiotechnology*, vol. 2, 2004.

[2] P. D. Howes, R. Chandrawati, and M. M. Stevens, "Colloidal nanoparticles as advanced biological sensors," 2014.

[3] M. Segev-Bar and H. Haick, "Flexible sensors based on nanoparticles," 2013.

[4] Y.-C. Yeh, B. Creran, and V. M. Rotello, "Gold nanoparticles: preparation, properties, and applications in bionanotechnology," *Nanoscale*, vol. 4, no. 6, pp. 1871–1880, 2012.

[5] J. Turkevich, P. C. Stevenson, and J. Hillier, "A study of the nucleation and growth processes in the synthesis of Colloidal Gold," *Discuss. Faraday Soc.*, vol. 11, no. c, pp. 55–75, 1951.

[6] J. Kimling, M. Maier, B. Okenve, V. Kotaidis, H. Ballot, and a. Plech, "Turkevich Method for Gold Nanoparticle Synthesis Revisited.pdf," *J. Phys. Chem. B*, vol. 110, no. 95 mL, pp. 15700–15707, 2006.

[7] I. Willner, R. Baron, and B. Willner, "Growing metal nanoparticles by enzymes," *Adv. Mater.*, vol. 18, no. 9, pp. 1109–1120, 2006.

[8] M. Gholami-Shabani, M. Shams-Ghahfarokhi, Z. Gholami-Shabani, A. Akbarzadeh, G. Riazi, S. Ajdari, A. Amani, and M. Razzaghi-Abyaneh, "Enzymatic synthesis of gold nanoparticles using sulfite reductase purified from Escherichia coli: A green eco-friendly approach," *Process Biochem.*, vol. 50, no. 7, pp. 1076–1085, 2015.

[9] T. Schüler, A. Steinbrück, G. Festag, R. Möller, and W. Fritzsche, "Enzyme-induced growth of silver nanoparticles studied on single particle level," *J. Nanoparticle Res.*, vol. 11, pp. 939–946, 2009.

[10] R. Möller, R. D. Powell, J. F. Hainfeld, and W. Fritzsche, "Enzymatic control of metal deposition as key step for a low-background electrical detection for DNA chips," *Nano Lett.*, vol. 5, pp. 1475–1482, 2005.

[11] V. Scherbahn, S. Nizamov, and V. M. Mirsky, "Plasmonic detection and visualization of directed adsorption of charged single nanoparticles to patterned surfaces," *Microchim. Acta*, vol. 183, no. 11, pp. 2837–2845, 2016.

[12] S. Nizamov, V. Scherbahn, and V. M. Mirsky, "Advanced wide-field surface plasmon microscopy of single adsorbing nanoparticles," *Procedings SPIE*, vol. 10231, p. 102312F, 2017.

[13] S. Nizamov, V. Scherbahn, and V. M. Mirsky, "Wide-field surface plasmon microscopy of nano- and microparticles: features, benchmarking, limitations, and bioanalytical applications," vol. 10231, pp. 1023108–1023109, 2017.

[14] S. Nizamov, V. Scherbahn, and V. M. Mirsky, "Detection and quantification of single engineered nanoparticles in complex samples using template matching in wide-field surface plasmon microscopy," *Anal. Chem.*, vol. 88, no. 20, pp. 10206–10214, 2016.

[15] S. Nizamov, V. Scherbahn, and V. M. Mirsky, "Wide-field surface plasmon microscopy of nano- and microparticles: features, benchmarking, limitations, and bioanalytical applications," in *Procedings SPIE*, vol. 10231, p. 1023108, 2017.

[16] S. Nizamov and V. M. Mirsky, "Wide-Field Surface Plasmon Resonance Microscopy for In-Situ Characterization of Nanoparticle Suspensions," in *In-situ Charact. Tech. Nanomater.* (C. S. S. R. Kumar, ed.), pp. 61–105, Berlin, Heidelberg: Springer Berlin Heidelberg, 2018.

[17] V. Scherbahn, S. Nizamov, and V. M. Mirsky, "Toward Ultrasensitive Surface Plasmon Resonance Sensors," in *Label-Free Biosensing Adv. Mater. Devices Appl. Springer Ser. Chem. Sensors Biosens.* (M. J. Schöning and A. Poghossian, eds.), pp. 1–40, Berlin, Heidelberg: Springer Berlin Heidelberg, 2018.

[18] S. Nizamov, O. Kasian, and V. M. Mirsky, "Individual detection and electrochemically assisted identification of adsorbed nanoparticles by using surface plasmon microscopy," *Angew. Chemie - Int. Ed.*, vol. 55, pp. 1–6, 2016.

[19] A. Demetriadou and A. Kornyshev, "Principles of nanoparticle imaging using surface plasmons," *New J. Phys.*, vol. 17, no. 1, p. 13041, 2015.

[20] A. Rangnekar, T. K. Sarma, A. K. Singh, and J. Deka, "Retention of Enzymatic Activity of a-Amylase in the Reductive Synthesis of Gold Nanoparticles," *Society*, no. 11, pp. 5700–5706, 2007.

[21] R. de la Rica and M. M. Stevens, "Plasmonic ELISA for the ultrasensitive detection of disease biomarkers with the naked eye," *Nat. Nanotechnol.*, vol. 8, no. 9, pp. 1759–1764, 2012.

[22] C. Peng, X. Duan, Z. Xie, and C. Liu, "Shape-controlled generation of gold nanoparticles assisted by dual-molecules: The development of hydrogen peroxide and oxidase-based biosensors," *J. Nanomater.*, vol. 2014, 2014.

[23] B. E. P. Swoboda and V. Massey, "Purification and Properties of the Glucose Oxidase from Aspergillus niger," *J. Biol. Chem.*, vol. 240, no. 5, pp. 2209–2215, 1965.

[24] T. Xuecai, Z. Jinlei, T. Shengwei, Z. Dandan, H. Zenwei, M. Yan, and H. Zaiyin, "Amperometric Hydrogen Peroxide Biosensor Based on Horseradish Peroxidase

Immobilized on Fe3O4/Chitosan Modified Glassy Carbon Electrode," *Electroanalysis*, vol. 21, pp. 1514–1520, jun 2009.

[25] D. V. Goia and E. Matijević, "Preparation of monodispersed metal particles," *New J. Chem.*, vol. 22, no. 11, pp. 1203–1215, 1998.

[26] M. Luty-Błocho, M. Wojnicki, and K. Fitzner, "Gold Nanoparticles Formation via Au(III) Complex Ions Reduction with l-Ascorbic Acid," *Int. J. Chem. Kinet.*, vol. 49, no. 11, pp. 789–797, 2017.

[27] J. A. Jacob, H. S. Mahal, N. Biswas, T. Mukherjee, and S. Kapoor, "Role of phenol derivatives in the formation of silver nanoparticles," *Langmuir*, vol. 24, no. 2, pp. 528–533, 2008.

[28] R. Baron, M. Zayats, and I. Willner, "Dopamine-, L-DOPA-, adrenaline-, and noradrenaline-induced growth of Au nanoparticles: Assays for the detection of neurotransmitters and of tyrosinase activity," *Anal. Chem.*, vol. 77, no. 6, pp. 1566–1571, 2005.

[29] K. Sun, J. Qiu, J. Liu, and Y. Miao, "Preparation and characterization of gold nanoparticles using ascorbic acid as reducing agent in reverse micelles," *J. Mater. Sci.*, vol. 44, no. 3, pp. 754–758, 2009.

[30] B. Abel, T. C. Clement, and K. Aslan, "Enhancement of enzymatic colorimetric response by silver island films on high throughput screening microplates," *J. Immunol. Methods*, vol. 411, pp. 43–49, 2014.

[31] P. Fanjul-Bolado, D. Hernández-Santos, M. B. González-García, and A. Costa-García, "Alkaline phosphatase-catalyzed silver deposition for electrochemical detection," *Anal. Chem.*, vol. 79, no. 14, pp. 5272–5277, 2007.

[32] B. Qu, L. Guo, X. Chu, D.-H. Wu, G.-L. Shen, and R.-Q. Yu, "An electrochemical immunosensor based on enzyme-encapsulated liposomes and biocatalytic metal deposition," *Anal. Chim. Acta*, vol. 663, no. 2, pp. 147–152, 2010.

[33] J. Switala and P. C. Loewen, "Diversity of properties among catalases," *Arch. Biochem. Biophys.*, vol. 401, pp. 145–154, 2002.

[34] A. Díaz, P. C. Loewen, I. Fita, and X. Carpena, "Thirty years of heme catalases structural biology," *Arch. Biochem. Biophys.*, vol. 525, no. 2, pp. 102–110, 2012.

[35] C. Engelbrekt, K. H. Sørensen, J. Zhang, A. C. Welinder, P. S. Jensen, and J. Ulstrup, "Green synthesis of gold nanoparticles with starch–glucose and application in bioelectrochemistry," *J. Mater. Chem.*, vol. 19, no. 42, p. 7839, 2009.

[36] M. A. Rothenberg and D. Nachmansohn, "Studies on cholinesterase," *J. Biol. Chem.*, vol. 168, pp. 223–231, 1947.

[37] P. Chelikani, I. Fita, and P. C. Loewen, "Diversity of structures and properties among catalases," *Cell. Mol. Life Sci.*, vol. 61, no. 2, pp. 192–208, 2004.

[38] T. H. Degefa, S. Hwang, D. Kwon, J. H. Park, and J. Kwak, "Aptamer-based electrochemical detection of protein using enzymatic silver deposition," *Electrochim. Acta*, vol. 54, no. 27, pp. 6788–6791, 2009.

[39] Y. Wang, R. Yuan, Y. Chai, Y. Yuan, and L. Bai, "In situ enzymatic silver enhancement based on functionalized graphene oxide and layer-by-layer assembled gold nanoparticles for ultrasensitive detection of thrombin," *Biosens. Bioelectron.*, vol. 38, no. 1, pp. 50–54, 2012.

[40] K. M. Holtz and E. R. Kantrowitz, "The mechanism of the alkaline phosphatase reaction: Insights from NMR, crystallography and site-specific mutagenesis," *FEBS Lett.*, vol. 462, no. 1-2, pp. 7–11, 1999.

[41] G. Mie, "Beiträge zur Optik trüber Medien, speziell kolloidaler Metallösungen," *Ann. Phys.*, vol. 25, no. 3, pp. 377–445, 1908.

Supplementary

This supporting material describes accompanying works on studying glucose oxidase and additional supporting material concerning alkaline phosphatase.

(S1) Glucose oxidase (GOD)
(S2) Alkaline phosphatase (ALP)

S1 GOD-mediated synthesis of gold nanoparticles

Several studies describe the ability of hydrogen peroxide (H_2O_2) to affect formation of gold nanoparticles in the presence of gold ions, mainly as $HAuCl_4$ salt, at defined conditions [1, 2]. Furthermore, different H_2O_2 concentrations lead to a formation of differently sized Au NPs that can be simply detected by naked eye. There are two ways of H_2O_2 to be involved into the reaction: either to be produced, or to be eliminated/reduced. The latter approach was successfully implemented as a biosensor based on formation of Au NPs in dependence of catalase (CAT) concentration, thus affecting the reduction of H_2O_2 [2]. Another approach is to generate H_2O_2, e.g. by converting glucose and O_2 to gluconolactone and H_2O_2 by glucose oxidase (GOD) [3, 4].

In order to prevent any unspecific, spontaneous formation of Au NPs due to organic buffers such as 2-(N-morpholino)ethanesulfonic acid (MES) [5], an inorganic buffer system – phosphate buffer – was chosen. To probe GOD as potential enzyme to mediate synthesis of Au NPs, first, the effect of H_2O_2 and buffer concentration was investigated in a colorimetric test (Fig. 2.32a). Using 10 mM phosphate buffer revealed to be the most appropriate concentration to form Au NPs starting from 1.2 mM H_2O_2. Fig. 2.32b-d represents the corresponding DLS results.

To exclude the impact of glucose on the formation of Au NPs, 50 mM and 100 mM glucose (both values are higher than the corresponding K_m value with ~33 mM [4] have been used both in a control without H_2O_2 and with differently concentrated H_2O_2 solutions. As can be seen in Fig. 2.33 no color formation in the absence of H_2O_2 in presence of $HAuCl_4$ is observed. Once H_2O_2 is added, a pink color is formed indicating synthesis of Au NPs.

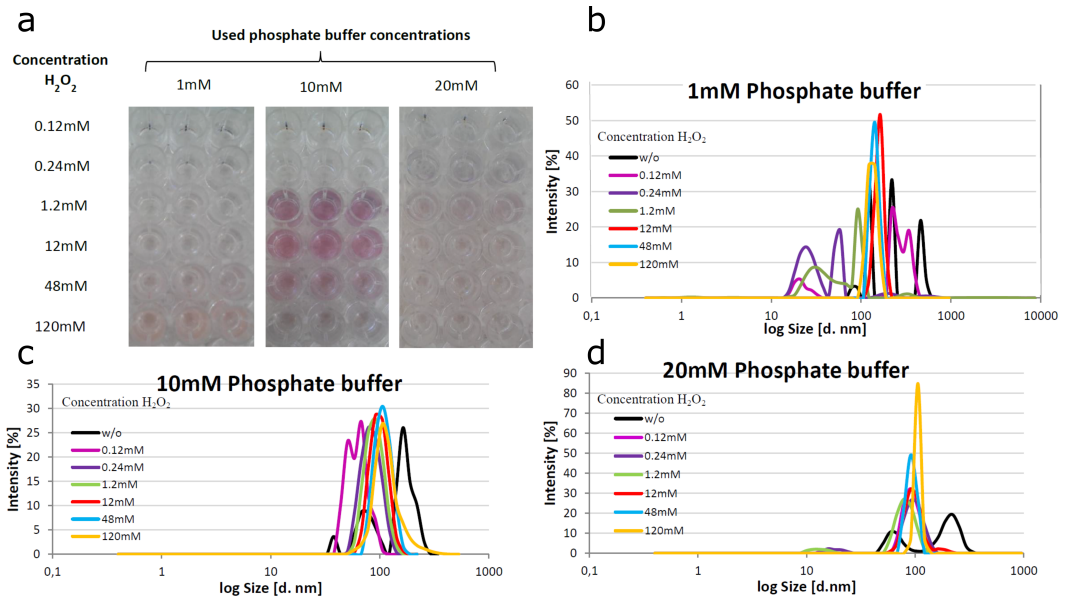

FIGURE 2.32: (a) Colorimetric test with different concentrated phosphate buffer at pH 7 and different concentrations of H_2O_2 with 0.1mM chloroauric acid ($HAuCl_4$) and incubated for 15min. (b-d) Dynamic light scattering (DLS) measurements representing averaged triplicates of the results corresponding suspensions with 1:10 sample dilution.

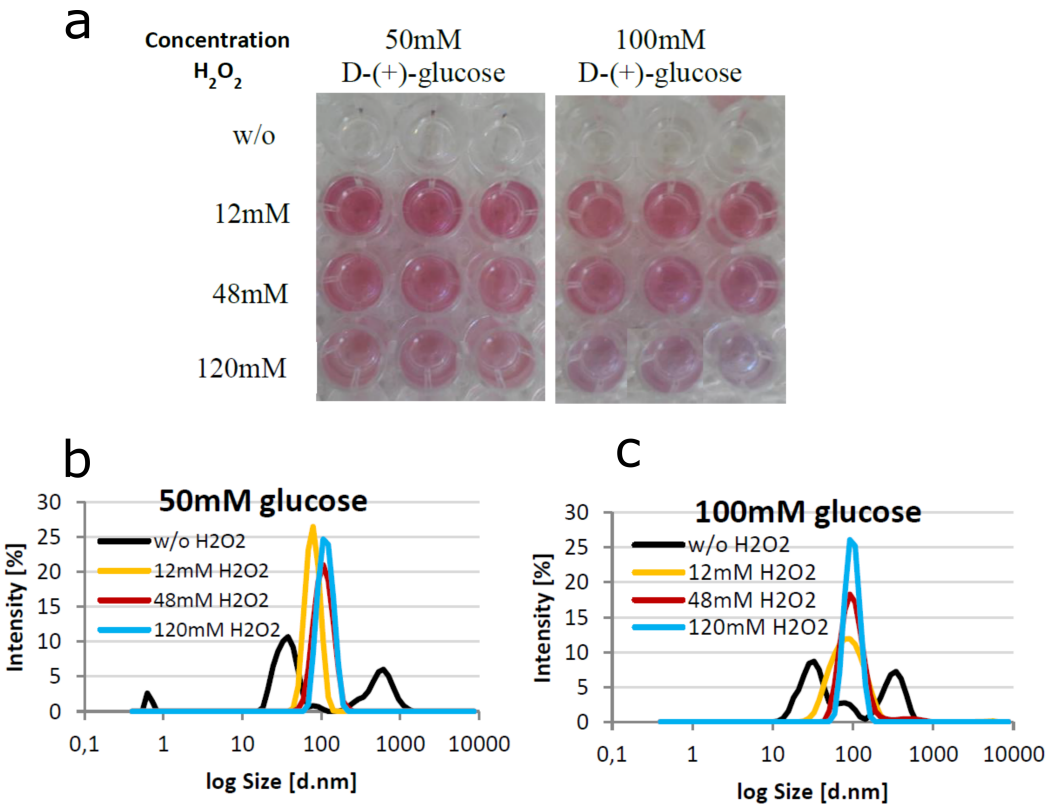

FIGURE 2.33: (a) Colorimetric tests as negative control to exclude unspecific formation of Au NPs in the presence of glucose. Glucose concentration of 50 and 100mM were used and incubated with different concentrations of H_2O_2 (0 mM, 12 mM, 48 mM, 120 mM) and 0.1 mM $HAuCl_4$ in 10 mM phosphate buffer at pH 7 for 15min. (b-c) Corresponding DLS measurements as as averaged triplicates of the 1:10 sample dilutions.

S2 ALP mediated synthesis of gold nanoparticles

The concentration of the working buffer (DEA) was set to 25 mM as using 10 mM, spontaneous formation of Au NPs was observed in the with AA-P and $HAuCl_4$ w/o ALP (Fig. 2.34a). Using higher DEA concentration (> 25 mM), NP were formed with much slower kinetics compared to 25 mM DEA. The concentrations of AA-P and $HAuCl_4$ were defined to be 1 mM as the fastest formation of Au NPs was observed (by naked eye) (Fig. 2.34b). The concentration of ALP stabilizing supplements was defined to 1 mM $MgCl_2$ and 10^{-6} M $ZnCl_2$ according to supplier information. Fig. 2.35 represents an NTA measurement of a sample containing AA-P, $HAuCl_4$ and ALP in solution.

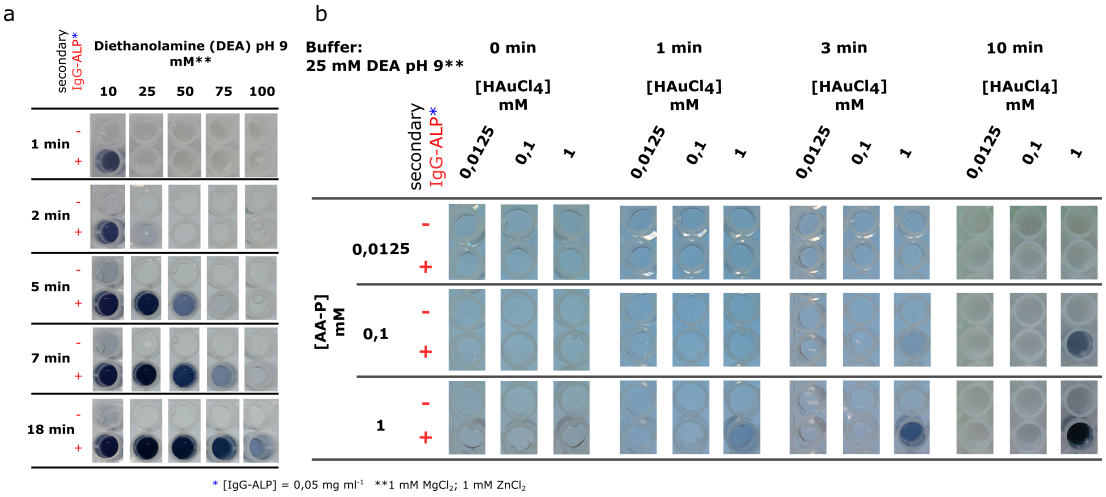

FIGURE 2.34: Colorimetric test using secondary anti-rabbit IgG-ALP investigating (a) the effect of different DEA concentrations as well as (b) different concentrations of $HAuCl_4$ and AA-P on the efficiency on nanoparticles formation.

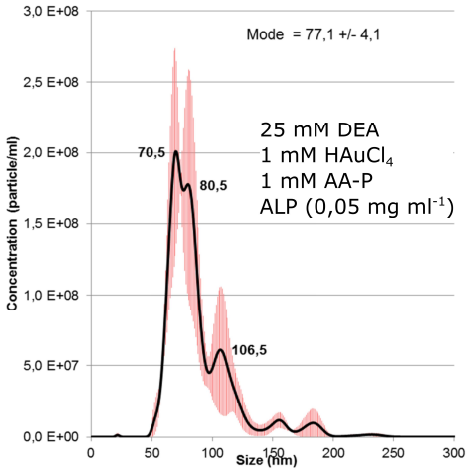

FIGURE 2.35: Measurement of ALP generated Au NPs by means of NTA

References

1. Willner I, Baron R, Willner B (2006) Growing metal nanoparticles by enzymes. Adv Mater 18:1109–1120

2. de la Rica R, Stevens MM (2012) Plasmonic ELISA for the ultrasensitive detection of disease biomarkers with the naked eye. Nat Nanotechnol 8:1759–1764

3. Wilson R, Turner A (1992) Glucose oxidase: an ideal enzyme. Biosens Bioelectron 7:165–185

4. Swoboda BEP, Massey V (1965) Purification and Properties of the Glucose Oxidase from Aspergillus niger. J Biol Chem 240:2209–2215

5. Engelbrekt C, Sørensen KH, Zhang J, Welinder AC, Jensen PS, Ulstrup J (2009) Green synthesis of gold nanoparticles with starch–glucose and application in bioelectrochemistry. J Mater Chem 19:7839

3. Summary and conclusion remarks

About 30 years ago, the introduction of SPR sensors has revolutionized the landmark of optical, label-free bio- and chemosensors. The measurement principle is based on the SPR effect being observed as a frustration of the total internal reflection of *p*-polarized light from a thin metallic layer deposited on the surface of a glass prism. At resonance conditions, the incident light induces collective electron oscillations in a highly conductive metallic layer (e.g. gold) generating an electromagnetic wave (plasmons) that exponentially decays (evanescent wave/field). Small changes of refractive index within the penetration depth of the evanescent wave shift the resonance conditions providing an extremely sensitive measurement of adsorption of any species onto the resonant surface: a few sub-angstrom change in the mean thickness of the adsorbed layer leads to a measurable signal. This promising technology was commercialized few years upon invention and has been adopted almost in all life-science-branches including scientific research, industry, medicine and pharmacology. One of the major milestones concerning the development of SPR has been achieved by its implementation as an imaging technology – SPRi or SPRM – allowing visualization of surface interactions by a camera as light detector. In spite of a comparable high sensitivity, SPR and SPRi/SPRM are still under continuous development in regard to the instrumental and methodological aspects. The major drawback, intrinsically accompanying SPR measurements, is the necessary separation between the signal obtained by surface interactions and that due to bulk effects. By overcoming this issue, a higher signal-to-noise-ratio (SNR) is expected resulting in a lower limit of detection (LOD). Following this goal, several approaches to improve the performance of SPR sensing were suggested, e.g. by optimization of receptor and resonant layers as well as of measurement setup and instrumentation.

Along with that, another direction towards optimization of the SPR performance was implemented by the introduction of a spatially separated referencing channel – in most cases it was a sensor area coated by a material bearing significantly lower affinity to analyte. Subtraction of the signal obtained by sensing channel from that obtained by referencing channel led to a certain compensation of the bulk effects. However, this approach bears several drawbacks. The spatial separation of sensing and referencing areas into distinct channels results in a loss of precious sensor surface remaining unexploited. Additionally, the determination of the sensing and referencing positions in many cases reveals to be difficult. It is to note that the overall efficacy of such an approach increases by diminishing the distance between the sensing and the referencing

areas to microscopic scale while maintaining a macroscopic total sensor area.

In that sense, the performance of SPR sensing to be improved was defined as the main objective of this dissertation. Two directions including several approaches were pursued to attain such an ambitious goal: (1) implementation of an internal referencing and (2) application of wide-field (WF)-SPRM to detect, to visualize and to characterize single nanoparticles adsorbed to modified surfaces. The realization of both directions is considered as one of the most important methodological advances in SPR sensing:

1. Implementation of an internal referencing
    - Self-referencing based on arbitrarily patterned sensing and referencing spots (section 2.1)
    - Ionic referencing in WF-SPRM towards visualization of changes in surface properties of patterned monomolecular layers (section 2.2)
    - Spatio-temporal referencing in WF-SPRM allowing a real-time detection and visualization of smallest changes in refractive index near/on the sensor surface
2. Application of WF-SPRM to detect, to visualize and to characterize single nanoparticles adsorbed to modified surfaces in real-time
    - in simple aqueous media (section 2.3) on differently coated sensor surfaces,
    - in complex media such as wine, juice or sun cream (section 2.4) and
    - upon their enzyme-assisted formation (section 2.5).

In section 2.1, a new approach for self-referencing in SPR was described. The self-referencing effect is based on integral measurement of reflected light from a heterogeneously patterned surface containing several sensing and referencing areas next to each other. The surface patterning was realized by means of a contact-less spotting (ink-jet like) technique to form self-assembled monolayer (SAM) patterns containing an anti-fouling coating – first step. Then, the rest surface was coated by SAM containing reactive groups (–COOH) enabling a coupling with biomolecules. The maximal self-referencing effect occurred near the summarized resonance conditions, only when a difference in optical thickness attributed to sensing and referencing areas was given and the surface was covered between 40% and 75% by sensing area. The proof-of-concept was realized by means of a model antigen-antibody-interaction assuming an increase in optical thickness on the sensing areas only. As a result, an over 10-fold suppression of bulk refractive index and temperature micro-fluctuations was measured indicating the feasibility of the self-referencing effect. Notably, this approach can be applied in many other commercially available SPR devices and, besides surface patterning, does not require any further modifications.

Micro-patterned SAM represent a powerful and versatile tool in biosensing applications, mainly in micro-array development. Based on micro-patterned coatings, a self-referencing effect in SPR (section 2.1) and a tool for directed adsorption of single nanoparticles (section 2.3) was implemented. However, such heterogeneous monomolecular coatings still remain difficult to be assessed or visualized using SPRi/SPRM as the influence of terminal functional groups on the refractive index revealed to be very small. A solution for this issue based on ionic self-referencing in WF-SPRM was presented in section 2.2. To implement ionic referencing, a patterned surface by charged SAM was flushed with specifically chosen electrolytes with a large disproportion of the molar refraction of cations and anions (e.g. sodium salicylate or benzyltrimethylammonium chloride) providing either some adsorption to the deposited SAM or participation in the formation of electrical double layer near areas with charged SAM (e.g. $–NH_2$ and –COOH). Thus, counter ions of the particular electrolyte solution adsorb to the oppositely charged SAM areas enabling their visualization over the whole sensor area. In addition, using this approach, a successful visualization and spatial distinction of three types of surface patterns was performed: an array containing spots with –OH and $–NH_2$ SAMs whereas the remaining part of the surface was coated by –COOH terminated SAM. As a pre-conclusion, ionic self-referencing represents an unobtrusive surface assessment being applicable to almost all SPRi/SPRM devices without damaging the sensor surface; thus, preserving the surface functionality for further experimental work. Besides, ionic referencing is very robust and enables a wide range of coating compounds to be studied.

Pursuing the aim to develop an ultra-sensitive detection of single analyte species using SPR, a major contribution in this direction was made applying WF-SPRM in combination with spatio-temporal referencing resulting in a powerful technology to detect and to visualize very weak changes in refractive index in real-time e.g. due to adsorption of a single nanoparticle. In order to detect, moreover to visualize, such weak changes in refractive index and to suppress the static and slowly changing background, differential frames were calculated showing intensity changes between two subsequent frames only – spatio-temporal referencing. The application of such referencing in WF-SPRM as detecting technology allows single metallic nanoparticles with ~15–20 nm in size and plastic/organic nanoparticles with ~50 nm in size to be registered, visualized and quantified in a broad dynamic range from a single adsorbed nanoparticle to several hundreds of thousands. Within this scope, the second direction of this thesis was dedicated by means of WF-SPRM technology in combination with spatio-temporal referencing to study interactions between nanoparticles and differently modified surfaces (section 2.3–2.5).

As engineered nanoparticles are nowadays applied in almost all industrial fields (e.g. food, cosmetic, pharmaceutical or paint industries) and according to several

studies, their exposition was shown to affect biological systems, highly sensitive techniques are required for their detection. In section 2.3, WF-SPRM was shown to detect and to visualize adsorption of single charged metallic and plastic nanoparticles in simple aqueous suspensions to SAM bearing different functional properties. Besides, the application of micro-patterning technique as a tool to design heterogeneous surface coatings enabled the detection and visualization of a directed adsorption of engineered nanoparticles to oppositely charged surface areas – an additional assessment approach of patterned surfaces besides ionic referencing. Unlike in simple aqueous media, the detection and visualization of nanoparticles in complex media may be affected by matrix components leading to detectable false positive signals. The unavoidable presence of the matrix effect is still considered as the main challenge in the development of analytical techniques to detect nanoparticles in real, complex samples. Therefore, sensitive and reliable technologies for that purpose are required.

In section 2.4, a solution to detect, to quantify and to characterize engineered nanoparticles in very complex media was presented. It is based on the WF-SPRM technology combined with a sophisticated image analysis based on template matching allowing to filter off the false-positive signals. Using this approach, a reliable limit of detection of $< 10^6$ nanoparticles mL^{-1} (~ 1.6 fM) or ~ 0.3 ppb in complex media such as wine, juice or sun cream formulation was achieved within a measurement time of 1 min without any pre-treatment of the sample. Furthermore, the WF-SPRM technology provided not only determination of number concentration of nanoparticles, but also information on their size and size distribution. As the measured signal intensity due to adsorption of single nanoparticles was found to be proportional to their size, mixtures of nanoparticles with different sizes were successfully probed. Apart from that, WF-SPRM was demonstrated to be applied for analysis of practically relevant media of different complexity, such as tap water, mineral water up to very complex ones, such as wines, juices and cosmetics. These results clearly indicate WF-SPRM to be superior over other analytical techniques for sensitive analysis of nanoparticles.

Besides classical chemical synthesis, recent research has shown a rather unusual approach to synthesize nanoparticles – by enzymes. In that sense, application of enzyme mediated synthesis of nanoparticles was suggested to be implemented as a tool for novel biosensing platforms in combination with WF-SPRM as the main detecting technology. The results were presented in section 2.5. Among several enzymes catalyzing reactions to induce synthesis of nanoparticles at ambient conditions, alkaline phosphatase was found to be the most appropriate biocatalyst for that purpose. In particular case, alkaline phosphatae catalyzed de-phosphorylation of phosphorylated ascorbic acid to ascorbic acid which in turn reduced gold ions forming gold nanoparticles. The feasibility of this reaction was first studied by colorimetric and spectrophotometric measurements as well as by nanoparticle tracking analysis applying alkaline phosphatase being freely, unbound in solution. The results confirmed a successful formation of gold nanoparticles in the presence of alkaline phosphatase, phosphorylated

ascorbic acid and gold ions. In the next step, WF-SPRM as main detecting technique was applied to detect and visualize single gold nanoparticles formed by alkaline phosphatase attached to the sensor surface as an enzyme-antibody-conjugate. As a result, a successful formation and adsorption of single gold nanoparticles formed by immobilized alkaline phosphatase was shown. The results also showed, in spite of immobilized enzyme, NPs to grow in the volume and afterwards to adsorb to the sensor surface. It is important to note that single enzymatically synthesized gold nanoparticles were shown to be detected for the first time by means of WF-SPRM technology. This approach represents an important milestone opening new possibilities to develop novel biosensing platforms e.g. to detect ultra-low analyte concentrations.

Based on past and recent progress, nowadays, the SPR technology has become one of the most powerful technologies to study affinity processes on differently modified surfaces. The application of several coating techniques, mainly those enabling the sensor surface to be structured, opens new versatile possibilities to explore novel approaches to improve the performance of SPR-based (bio)sensors. Unlike the classical SPR technology, the recently developed WF-SPRM technology enables detection and visualization of single engineered and biological (e.g. exosomes; these results were not included into the present thesis) nanoparticles to be detected at sub-femtomolar concentrations. As sensitive detection of nanoparticles is nowadays considered as a "hot" topic, the WF-SPRM technology may enormously contribute towards nanoparticle analytics. Due to the continuous development and improvement of the SPR technology in general, detection of even single proteins or DNA molecules is expected to be realized very soon. The combination of SPR with other analytical techniques (e.g. electrochemical, surface-enhanced Raman scattering, mass spectrometry, chromatography) is being suggested to further extend the potential capabilities of this technology. Therefore, SPR sensors are highly competitive and, more importantly, hold a lot of promise for further developments in ultra-sensitive analytics.

Acknowledgement

This dissertation would not have been possible without the assistance and contribution of many people whom I wholeheartedly would like to thank.

Dear Prof. Mirsky, I sincerely express my gratitude to you as you gave me the opportunity to be member of your research group "Nanobiotechnology" at the BTU Cottbus-Senftenberg. Without you my dissertation would have been impossible.
Thank you for your mentoring throughout my scientific work, for the vast amount of discussions, for giving me freedom for own ideas as well as for invaluable advices also beyond scientific matter. I very enjoyed to work with you and to continuously gain new experience in the field of (bio)sensing.

In the same way I would like to thank Dr. Shavkat Nizamov for supporting and giving me enormous motivation, for instance when things seemed to be difficult. Thank you for all your help, for instance concerning all technical work in the lab.

My special thanks belong to Dr. Karin Tonder for an immense support and help in regard to all administrative and organizational issues. Thank you for your uncomplicated and open manner whenever different questions have arisen.

Sincere thanks belong to the present and former members of the group "Nanobiotechnology" M.Sc. Ajay Sridhar, M. Sc. Arwa Laroussi, Dr. Olga Kasian, M.Sc. Yulia Efremenko, Dipl.-Chem. Franziska Klemm. Thank your for a pleasant time, for your support and fruitful discussions also apart from scientific area.

I would like to express my deepest thanks to all my colleagues from the Institute of Biotechnology for the positive atmosphere throughout my working phase. In particular, I am very grateful to Prof. Klaus-Peter Stahmann, Dr. Susann Barig and Dr. Kai-Uwe Schmidtke for their support to realize UV-VIS measurements and to Dr. Stephan Rödiger for interesting discussions and important advices. I want to thank M.Sc. Hannes Meyer, M.Sc. Susanne Steinbrecht and M.Sc. Elisabeth Nowak for nice discussions during our work-home-travels by train.

I would also like to thank Prof. Peer Schmidt and Prof. Gunther Wittstock for their willingness and time to assess my doctoral dissertation.

I deeply thank my parents and my grandparents for all their support in my life.

Finally, I address my warmest appreciation to my wife and my daughter. Thank you for your love and encouragement – the most precious gifts.

Thank you all for your help!